Synthesis of Zeolite Nanosheets and Applications in Membranes and Adsorption Separation Processes

A Dissertation
SUBMITTED TO THE FACULTY OF
UNIVERSITY OF MINNESOTA
BY

Mi Young Jeon

IN PARTIAL FULFILLMENT OF THE REQUIREMENTS
FOR THE DEGREE OF
DOCTOR OF PHILOSOPHY

Professor Michael Tsapatsis, Adviser

May 2016

Acknowledgements

I would like to thank my advisor, Professor Michael Tsapatsis, for supporting and guiding me with patience during my journey. It has been an honor to work with him closely under his guidance. My discussions with him have motivated me to become, like him, a good scientist. His brilliant ideas and outstanding insight always inspire me. I am grateful to him for showing me how to solve problems and for encouraging me to think deeply without jumping to conclusions. I also would like to extend my appreciation to Professor Alon McCormick, Professor Andre Mkhoyan, and Professor Lee Penn for agreeing to serve on my committee.

I am grateful to have had the opportunity to work with many people in Tsapatsis' group: their creativity is inspiring. Interacting with the group's talented graduate students and post-docs has broadened my horizons. I especially thank Dr. Pyung-Soo Lee, a senior student in Tsapatsis' group, for our numerous discussions about research. I am grateful to Dr. Donghun Kim for his generous help with the AFM and high resolution SEM analysis of my samples. I thank Prashant Kumar, who carried out intensive HR-TEM analysis and simulations of my samples, and Dr. Limin Ren, who prepared the SPP samples for vapor adsorption measurement. Without their help I would not have completed this dissertation.

In particular, I deeply thank my beloved mother, Im Sook Kang, who always cares about me, for her unconditional love, devotion and sacrifices. She is always there for me. Thanks to her sincere and wise advice in my personal life, I have learned how to handle tough issues. Without her, I would not have dared to start this long journey. There are no words to express my gratitude to her.

Dedication

To my mother.

Abstract

In separation processes, desirable products with high purity are acquired at the expense of high energy cost procedures such as distillation. Alternative separation processes, such as zeolite membrane separation and adsorption processes, are promising to reduce the energy cost of production since zeolites can discriminate molecules on the basis of size/shape and functionality. Indeed, the high cost of zeolite membranes can be reduced by fabricating thin membranes with high throughput. High aspect ratio zeolite nanosheets can be used to fabricate zeolite membranes with high throughput on porous supports. To date, however, there is no published evidence that scientists have successfully achieved nanosheet synthesis under the direct hydrothermal treatment route. This dissertation documents a successful direct hydrothermal synthesis of zeolite nanosheets via seeded-growth—a process that leads to zeolite membranes that exhibit high performance on xylene isomer and butane isomer permeation. To the best knowledge, this is the first achievement to prepare zeolite nanosheets without complicated post treatment such as exfoliation and purification process (density gradient centrifugation). Extensive parametric studies are conducted in order to establish the optimal synthesis condition for high quality zeolite nanosheets. Additionally, in an effort to understand the mechanism of nanosheet formation, the sequential evolution of seed crystals into zeolite nanosheets is observed by time-resolved TEM imaging analysis. Keeping in mind that in the future polymers could be used to reduce the costs of membrane manufacture, the de-templation of MFI nanosheets without formation of aggregates is discussed in this dissertation.
In addition to membrane applications, this dissertation probes the roles of hydrophobicity in ethanol adsorption when hydrophobic siliceous zeolites, and defective siliceous zeolite nanosheets with house-of-card architecture are provided as adsorbents. Vapor phase ethanol adsorption and aqueous phase ethanol adsorption are compared to investigate how water molecules affect ethanol adsorption onto siliceous zeolites in the aqueous phase.

Table of Contents

List of Tables

List of Figures

Chapter 1: Introduction

Zeolites are crystalline aluminosilicate materials composed of regular connections of Si or Al atoms (T atoms) in oxide forms. These are backbone structures of molecular-sized pores that range in size from 0.3 to 2 nm, and they have applications in catalysis, separation, and ion exchange[1]. The neutrality of the zeolite frameworks, which is associated with applications, can be tuned via the Si/Al ratio in the frameworks. For example, the charged aluminosilicate zeolites have been employed as catalysts and ion-exchangers.[2-5] In contrast, hydrophobicity and adsorption affinity play important roles in applications of neutrally charged siliceous zeolite. For instance, siliceous zeolites can separate ethanol from water in the aqueous phase due to higher adsorption affinity to relative hydrophobic molecules—ethanol.[6-11]

During the late 1940s, Richard Barrer and Robert Milton[12] of Imperial College, London, were the first to artificially synthesize a zeolite (the KFI type zeolite). Since then, many scientists have tried to synthesize other types of zeolite[12-17] and elucidate the mechanism of zeolite formation.[12,18-33] These studies reveal that zeolite crystal structure can be manipulated by changing such variables as temperature, composition, and structure-directing agent (SDA). To date, the International Zeolite Association (IZA) has recognized 231 zeolite topologies,[34] and in each case the framework type is designated by three letters—for example, LTA, FAU, BEA, and MFI.

The MFI type zeolite has been the focus of many investigations of the separation of organic molecules since its pore dimensions are similar to those of many organic molecules.[35] The siliceous MFI zeolite framework (**Figure 1-1A**)[36] consists of ten

interconnected SiO_4 tetrahedral (10MR) with straight pore channels (5.2 Å × 5.8 Å) along the crystallographic *b*-axis. Additionally, the siliceous MFI zeolite framework forms sinusoidal pore channels with 10MR along *a*-axis (5.5 Å × 5.1 Å) (**Figure 1-1B**).[37] In this dissertation, the MFI zeolite framework is employed in separation applications.

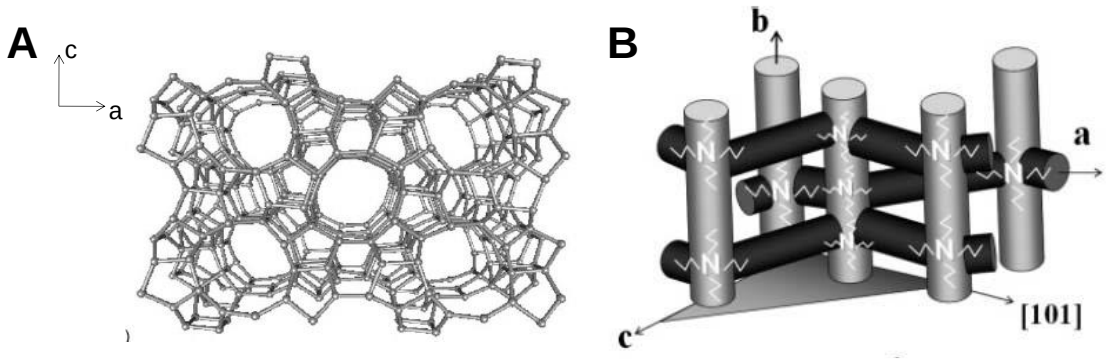

Figure 1-1. Schematic representation of the MFI framework along the [010] direction (A). Each node represents a SiO_4 tetrahedral and each stick denotes the oxygen bridge. This image is reproduced from reference 36. The cartoon of MFI pore channels exhibits straight pores along *b*-axis and sinusoidal pores along *a*-axis (B). The image is adapted from reference 37.

Applications of zeolites in membranes and adsorption processes have been of interest as alternatives to energy-intensive industrial separation processes such as distillation and crystallization since zeolites discriminate chemical species on the basis of size/shape.[38-45] Compared to membrane technologies such as polymeric membranes, zeolite membranes have a far superior separation performance (permeance and separation factor) due to their precisely defined micropore structure. Moreover, zeolite membranes are stable when exposed to high temperature, organic molecules, and oxidizing agents.[38]

In spite of intensive attempts to fabricate free-standing zeolite films, they have not been employed as membranes due to the low mechanical strength (i.e., the high brittleness) of

the films.[38] To overcome the fragility, researchers have fabricated supported zeolite films. There are two methods for fabricating zeolite membranes on porous supports: the in-situ method and the secondary growth method. In the case of the-situ method, bare supports are dipped into an appropriate zeolite precursor sol and then heated for nucleation and crystal growth of zeolites.[42,46-49] Although the process is simple, the in-situ zeolite membrane preparation does not control the orientation of the zeolite crystals in the membranes.[49] Also in-situ membrane preparation leads to thick membranes that have high resistance to molecular transport.[49]

In the alternative method, the secondary growth strategy, zeolite seed layers are prepared on porous supports that then are dipped into a zeolite precursor sol. The orientation, size, and shape of the zeolite crystals are manipulated by deposition methods such as dip coating,[44] manual rubbing,[7,50,51] sonication,[52] and vacuum assisted coating.[53-55] The secondary growth approach produces zeolite membranes that are thin and oriented.[50-52,56-58]

The zeolite membrane cost is typically $5,000 ~ $10,000 per unit area of membranes.[59] If the cost does not decreases, a ten fold increase in flux (high throughput) is the way forward. The high throughput can be achieved via thin membranes, which can be attained by reducing the size of zeolite crystals.[4,57,60] By disassembling large crystals[57,61] through sonication researchers can reduce the size of zeolite crystals, but in this method it is difficult to control the orientation of zeolite nano-crystals due to their isotropic morphology. Moreover, the method produces low yields and so it is not useful for large-scale applications.

Another means of obtaining thin zeolite membranes is to prepare anisotropic zeolite crystals, which are thin (a couple of unit cell dimensions) along a certain crystallographic axis leading to a high aspect ratio. The resulting morphology appeared to be a sheet with a few nanometer thickness, and so it is called as "zeolite nanosheets." Zeolite nanosheets can be used to control the orientation of the zeolite membranes due to anisotropic morphology. For a couple of decades researchers have tried to prepare zeolite nanosheets through direct hydrothermal treatment, but no successful results have been reported. In a more successful approach nanosheets have been produced by exfoliating layered precursor zeolites (hereafter called "the top-down approach").[3,53-55,62-66] However, this strategy has drawbacks as well. For example, certain exfoliation methods, including the high base treatment, destroy nanosheet crystallinity.[3,62]. Further complicating matters, a purification step is required to collect the exfoliated zeolite nanosheets, and this purification step leads to low yields. Thus, this method, too, is not appropriate for large scale processes.

A possible solution to these problems might be to produce zeolite nanosheets through direct hydrothermal synthesis, hereafter called "the bottom-up synthesis." This dissertation describes the first successful bottom-up synthesis of MFI zeolite nanosheets. There are two mechanism of separating zeolite membranes; size/shape discrimination and sorption-diffusion. Under the first model, which is the simpler of the two, molecules smaller than the pore size of the zeolite framework can diffuse through micropores while bigger ones cannot. For example, a molecule, *p*-xylene (5.8 Å), that is smaller than *o*-xylene (6.8 Å) can pass through the micropore channels of the MFI zeolite framework.

Similarly, *n*-butane (4.3 Å, a linear molecule) can be separated from *i*-butane (4.9 Å, a branched molecule) since the linear molecule, *n*-butane, preferentially diffuses into the micropores of the MFI zeolite while the branched molecule, *i*-butane, does not.

The second mechanism, sorption/diffusion, is facilitated by adsorption affinity of zeolite framework to chemical species. For instance, through the sorption-diffusion mechanism ethanol (4.3 Å) is separated from water (2.7 Å). Water molecules can predominantly diffuse into the micropore channels of the MFI zeolite framework due to their small molecular size. In contrast, in the case of siliceous MFI zeolites, hydrophobicity leads to the preferential adsorption of ethanol rather than water molecules owing to relatively high hydrophobicity of ethanol. Thus, ethanol can be separated through siliceous MFI zeolites.

Usually organic SDA molecules occluded in zeolite pore channels should be removed through thermal treatment (hereafter called "calcination"). Upon calcination, the zeolite nanosheets form aggregates, and this renders them not appropriate for thin membrane applications. SDA elimination should not cause aggregates to form for thin membrane applications. Inexpensive polymeric supports can replace expensive inorganic supports if SDA-free zeolite nanosheets are prepared prior to depositing the zeolite nanosheets onto the polymeric supports. To prepare SDA-free zeolite nanosheets without formation of aggregates, the SDA molecules should be eliminated using a method other than thermal treatment. A potentially viable approach, the oxidation of SDA molecules via *Fenton chemistry*, has been developed for aluminosilicate BEA nano-crystals.[67,68] This dissertation evaluates the usefulness of applying *Fenton chemistry* to MFI zeolite nanosheets.

Adsorption, too, is a relatively low energy-intensive separation technology that purifies chemicals and fuels.[69] Its efficiency depends on how chemicals are adsorbed onto the zeolite framework. To understand zeolite membrane systems under the sorption-diffusion model (e.g., ethanol separation from aqueous phase by the siliceous MFI zeolites), the adsorption affinity between adsorbates and the zeolite framework must be demonstrated. In this dissertation ethanol adsorption onto pure silica MFI zeolites is demonstrated.

This dissertation, which consists of 4 chapters plus an appendix, examines three topics: 1) the synthesis of zeolite nanosheets; 2) applications in membranes; and 3) adsorption separation processes. The first three chapters examine the synthesis of zeolite nanosheets and the membrane preparation method. The fourth chapter discusses adsorption processes.

This dissertation is organized as follows.

Chapter 2 illustrates the first successful direct hydrothermal treatment, or the bottom-up synthesis, of MFI zeolite nanosheets that serve as building units of zeolite membranes. In a discussion of how to optimize the synthesis condition zeolite nanosheets produced from parametric studies are characterized by SEM and TEM. To understand the synthesis process the time-resolved evolution of the MFI nanosheets is observed.

Chapter 3 describes the preparation of zeolite membranes from MFI nanosheets synthesized using the bottom-up strategy is described. Different types of inorganic supports, coating sol of nanosheets, and secondary growth are introduced to control the microstructure of the MFI nanosheet membranes. The resulting membranes are tested for xylene isomer permeation and butane isomer separation.

Chapter 4 describes research on SDA removal. In the attempt to remove SDA out of zeolite framework, formation of few or no aggregates of the MFI nanosheets is desirable for future applications that combine with polymeric supports. The methods are divided into thermal treatment and chemical treatment types. To examine the viability of these types the micropore openings and the morphologies of nanosheets produced under each type of treatment are characterized.

Chapter 5 examines ethanol and water adsorption behavior onto siliceous MFI crystals in nanosheet morphology and the conventional coffin shape. Influences of hydrophobicity of the siliceous MFI crystals on ethanol adsorption are probed in vapor phase. This work was undertaken in collaboration with Dr. Matthias Thommes (Quantachrome) and Dr. John Bullis (Hiden Isochema). Roles of water in ethanol adsorption onto the siliceous MFI crystals are probed by comparison of vapor phase and aqueous phase adsorption.

The appendix describes the preparation of MFI zeolite nanosheets under the top-down approach. Prior to undertaking the bottom-up synthesis the multilamellar MFI nanosheets were exfoliated and they underwent simple purification. The exfoliated nanosheets are exploited to fabricate zeolite membranes and ethanol pervaporation performance of the membranes is investigated.

Chapter 2: Preparation of bottom-up synthesis of MFI nanosheets for membranes

2.1 Introduction

Several attempts have been made to decrease the diffusion path length for high throughput membranes[59] and catalysts through the direct hydrothermal synthesis of zeolite nanosheets. However, to date none have produced a direct synthesis of zeolite nanosheets due to the difficulty of rationally designing structure-directing agents and a synthesis methodology. Instead of directly synthesizing zeolite nanosheets, researchers have employed a wide range of indirect top-down strategies that involve parent materials that are layered structure zeolites. To delaminate the layered structure of zeolites, researchers have employed the high base treatment, ultrasonication, fluoride/chloride anion promoted exfoliation, and melt extrusion with a polymer.[3,53,54,62-65] The delamination method most amenable to preserving pristine zeolite crystallinity is melt extrusion with a polymer. For the last seven years, Tsapatsis' group has exfoliated zeolite nanosheets through melt extrusion with a polymer. Hereafter, the term "top-down method" refers to melt extrusion with the polymer polystyrene.

The melt extrusion with polystyrene is attractive because it preserves the pristine crystallinity of the zeolite nanosheets, but there are drawbacks to this method. During the exfoliation process of the top-down strategy, the resulting MFI zeolite nanosheets were broken down into small pieces owing to the high shear forces produced by the high viscosity of polystyrene. As a result, the maximum lateral size of the exfoliated MFI nanosheets is 200 nm × 200 nm. The reduced lateral size is likely to create an increased

number of grain boundaries, which are potential defects. Therefore, this breakage of MFI nanosheet crystals is not desirable for membrane fabrication.

After exfoliation, unexfoliated MFI particles and polystyrene co-existed with the exfoliated MFI nanosheets. To purify the exfoliated MFI nanosheets, multiple steps of centrifugation must be carried out combined with density gradient centrifugation (DGC).[54] This time-consuming process generates plenty of organic solvent waste, which is not environmentally-friendly. The resulting yield of the exfoliation is so low, i.e., 10%, that the majority of the starting material, i.e., layered MFI zeolites, is wasted. Additionally, the strategy is not suitable for commercialization; instead, it is appropriate for a small batch process in lab-scale.

Some suggest that the direct synthesis of zeolite nanosheets (i.e., the bottom-up approach) will provide a solution to the shortcomings mentioned above. Inspired by a previous report by Tsapatsis' group,[70] which concluded that MFI zeolite crystal morphologies are controlled by different types of structure-directing agents—suggesting that a bottom-up synthesis of MFI nanosheets might be possible—in this chapter a bottom-up synthesis is developed. In the previous work conducted by Tsapatsis' group, MFI zeolite plates co-existed with peculiar MFI zeolite crystals. These crystals had a *b*-elongated cylindrical shape that resulted from seeded-growth produced by the structure-directing agent bis-1,5 (tripropyl ammonium) pentamethylene diiodide (hereafter dC5). However, in the work of the Tsapatsis' group, the major components of the resulting crystals were peculiarly *b*-elongated cylindrical MFI crystals. Moreover, the *b*-elongated MFI crystals were of interest since they were experimentally demonstrated for the first

time. Based on the previously reported results, bottom-up synthesis of MFI zeolite nanosheets is carried out in this chapter.

This chapter describes the development of bottom-up synthesis of MFI zeolite nanosheets with dC5 via seeded-growth. To identify the optimal condition for acquiring high quality MFI nanosheets parametric studies are described in this chapter. The last section of this chapter describes a time-resolved TEM study that examines how MFI seed crystals evolve into MFI nanosheets during synthesis.

2.2 Experimental

Synthesis of dC5

dC5 was synthesized through an exhaustive alkylation of 1,5-diaminopentane with 1-iodopropane.[70,71] The corresponding chemical reaction was as follows:

$C_5H_{14}N_2 + 6C_3H_7I + 2K_2CO_3 \rightarrow C_{23}H_{52}N_{22}I + 4KI + 2H_2O + 2CO_2$

18.90 g of 1,5-diaminopentatne (> 97 %, Sigma-Aldrich) was added to a dry three neck 1 L round bottom flask that contained 450 mL of 2-butanone (99.5 %, Sigma-Aldrich). An excessive amount (82.35 g) of anhydrous potassium carbonate (Sigma-Aldrich) was mixed as a water scavenger. The mixture was purged by an argon flow and then loaded in an oil bath heated to 80 °C. When the oil bath temperature reached 80 °C, the argon flow was stopped and 108 mL of 1-iodopropane (99 %, Sigma-Aldrich) was slowly added with a glass syringe through a rubber septum. When the addition of the 1-iodoproane was finished, the reactor was wrapped with aluminum foil to prevent light decomposition and it was connected to a condenser. The argon flow was turned on again. The reaction was

allowed to proceed for 10 h under an argon environment followed by a cooling down to 60 °C. The resulting product was filtered and solids (solid 1) and filtrate were collected for further purification. The solid 1 was composed of dC5 and impurities.

2-butanone in the filtrate (yellow solution) was removed by rotary evaporation at 60 °C, which led to an off-white solid. 250 mL of 2-butanone was added into the solid and then stirred for 30 min. After dissolving the solid, ethyl acetate (99.9 %, Fisher Scientific) was added in order to precipitate out an off-white solid (solid 2). After stirring for 6 h, the solid was recovered by filtration.

The solids, solid 1 and solid 2, were not pure and contained potassium carbonate and potassium iodide, which is a byproduct of reaction. Since dC5 is highly soluble in ethanol, the solids were dissolved in ethanol. The ethanol solution was filtered and the filtrate was collected. Since potassium carbonate is not soluble in ethanol and potassium iodide is slightly soluble, in the filtrate, the major component is dC5. To remove the trace amount of potassium iodide, the ethanol in the filtrate was evaporated at 60 °C by rotary evaporation, and then the purification steps (dissolving in ethanol, filtration and evaporation in sequence) were repeated 3~4 times. The resulting solid was dissolved into 250 mL of 2-butanone and stirred for 30 min. Then 250 mL of ethyl acetate was added to precipitate out the solids. After 6 h of stirring, the solids were recovered by filtration. To acquire high purity dC5, the solids were extracted with ethanol once again and that was followed by recrystallization by using 2-butanone and ethyl acetate.

The final product was analyzed by ^{13}C NMR and ^{2}H NMR to confirm that the structure of the product corresponds to dC5.

Synthesis of TPA primary seeds

The nano-crystals of silicalite-1, primary seeds were prepared from a molar composition of $10SiO_2$: 2.12TPAOH: 0.76NaOH: $97.27H_2O$. Every chemical was used without further purification. 8.93 g of tetrapropyl ammonium hydroxide solution (TPAOH, 1.0 M, Sigma-Aldrich) was mixed with 0.16 g of deionized (DI) water, and then 0.127 g of sodium hydroxide (NaOH, 97 %, Sigma-Aldrich) was added. After completely dissolving the sodium hydroxide, 2.5 g of silicic acid (99.9 %, 20 μm, Sigma-Aldrich) was added as a silica source. The mixture was stirred overnight at room temperature and then heated at 50 ºC for 6 days. The solution was filtered with a 12 mL syringe that was connected to a 0.45 μm GHP (polypropylene) syringe filter, and then the filtrate was heated at 100 ºC for 3 days. The primary seed particles were recovered by centrifugation at 14,500 RCF (Relative Centrifugal Force) three times for 1 h.

Synthesis of dC5 secondary seeds

Following centrifugation the recovered primary seeds were re-dispersed in DI water and then an aliquot was taken for evaluating the silica molar concentration of the suspension. The rest of the primary seed suspension was mixed with a dC5 precursor sol composed of dC5, hydrolyzed TEOS, water and potassium hydroxide (KOH) that had the following molar composition: $120SiO_2$: 7.5dC5: 25KOH: $9500H_2O$: 480EtOH. When the primary seed suspension was mixed with the dC5 precursor sol, the silica molar concentration of the dC5 precursor sol was four times higher than that of the primary seed suspension. The mixture was transferred into a Teflon-lined stainless-steel autoclave and heated at 150 °C

for 3 days under rotation. The secondary seed particles were recovered by centrifuging three times at 14,500 RCF for 5 min.

Synthesis of nanosheets: Two-step

The recovered secondary seeds were re-dispersed in DI water and then the silica molar concentration was determined for synthesis of nanosheets. The secondary seed suspension was mixed with a dC5 precursor sol comprised of dC5, hydrolyzed TEOS, water and KOH that had a molar composition of $80SiO_2$: 3.75dC5: 25KOH: $9500H_2O$: 320EtOH. When the secondary seeds were mixed with the dC5 precursor sol, the silica molar ratio of the secondary seed suspension to the dC5 precursor sol was 1:60. The hydrothermal treatment conditions varied under static conditions: at 140 °C for 3 days, at 150 °C for 2 days, and at 160 °C for 2 days.

Synthesis of nanosheets: One-step

To shorten the length of time needed for nanosheet preparation, the recovered primary seed crystals were used rather than the secondary seeds during the seeded-growth. The recovered primary seed suspension was mixed with the dC5 precursor sol where molar composition was $80SiO_2$: 3.75dC5: 25KOH: $9500H_2O$: 320EtOH. When the primary seed suspension was mixed with the dC5 sol, the silica molar ratio of the primary seed suspension to the dC5 precursor sol was 1:200. The mixture was hydrothermally treated under static conditions at 150 °C for 3 days.

Parametric studies of one-step synthesis

To optimize the quality of the nanosheets, parametric studies were conducted using variables such as pH, silica molar ratio, cation size of base, temperature, and

crystallization time. As described in **Table 2-1**, the influence of pH adjusted by concentration of KOH on synthesis was explored, and the optimized pH condition was identified.

Table 2-1. Experimental details of molar composition of dC5 sol with various concentrations of potassium hydroxide. The silica molar ratio of the primary seeds to the dC5 sol was 1 to 200. *a) the dC5 sol of sample 1 was prepared by ion exchange with an ion exchange resin of –OH form (Amberlite IRN-78 ion-exchange resin, Acros).

Sample name	SiO_2	dC5	H_2O	KOH	pH	Temperature (°C)	Time (days)
1	80	3.75	9500	0[a)]	10.36	150	3
2				5	10.77		
3				10	11.36		
4				15	11.54		
5				20	11.63		
6				25	11.72		

A wide range of silica molar ratios of primary seeds to dC5 sol that had sol composition of $80SiO_2$: 3.75dC5: 15KOH: $9500H_2O$: 320EtOH was examined: 1:30/1:60/1:200/1:400/1:600/1:800. Not only potassium hydroxide but also other bases are chosen as mineralizing agents: sodium hydroxide, cesium hydroxide (50 wt%, 99.9 %, Sigma-Aldrich) and rubidium hydroxide (50 wt%, 99 %, Sigma-Aldrich). The objective was to investigate the influence of the size of cations of base on nanosheet

synthesis. The molar composition of dC5 sol was $80SiO_2$: 3.75dC5: 15MOH (M: Na, K, Cs, and Rb): $9500H_2O$: 320EtOH, and the silica molar ratio of primary seeds to the dC5 sol was fixed to 1:200. The hydrothermal treatment was carried out at 150 °C for 3 days under static conditions.

The effect of hydrothermal treatment temperature on resulting nanosheet quality was explored by varying temperatures such as 150, 160, 165, and 170 °C. The silica molar ratio of primary seeds to the dC5 sol that had composition of $80SiO_2$: 3.75dC5: 15KOH: $9500H_2O$: 320EtOH, was 1:200. The crystallization time was also varied: shorter crystallization time (52 h) and prolonged crystallization time (20 days and 31 days).

Effects of seeds

To investigate an impact of primary seeds, crystal growth with no seeds was carried out from the only dC5 sol where composition was $80SiO_2$: 3.75dC5: 15KOH: $9500H_2O$: 320EtOH. Seeds of different sizes and morphologies were used to investigate effects of size and morphology of seeds. Seeds smaller (*ca.* 20 nm) than regular primary seeds were provided through disassembly of the 3-DOm-i (3 Dimensionally Ordered Mesoporous Imprinted) MFI.[57] These were provided by Dr. Pyung-Soo Lee at the Korea Research Institute of Chemical Technology (KRICT) and Prof. Wei Fan at the University of Massachusetts Amherst. Employing the same chemicals used to prepare primary seeds, bigger seeds (*ca.* 120 nm) were prepared from a precursor sol where composition was $10SiO_2$: 2.12TPAOH: 0.76 NaOH: 97.27 H_2O. The precursor sol was transferred into a Teflon-lined stainless-steel autoclave and heated at 120 °C for 3 days under static conditions. Intergrown nanosheet seeds were also prepared: SPP (Self Pillared Pentasil)[72]

seeds that consisted of a unit cell thickness (2 nm) of nanosheets arranged along the *b*-axis with a house-of-card arrangement.

Aluminum and tin insertion

Pure silica zeolites do not have an activity for reaction, and without this activity they cannot serve as catalysts. Thus, heteroatoms such as aluminum and tin should be incorporated into the zeolite framework for an activity. To ensure that the pure silica zeolites could be used as catalysts, aluminum and tin was inserted into the MFI framework.

To this end, aluminum-tri-(sec-butoxide) ($Al(sec\text{-}BuO)_3$, 97 %, Sigma Aldrich) was used as an aluminum source. 0.55 g of dC5 was dissolved in 41.1 g of DI water and then 0.204 g of KOH was added. After a clear solution was acquired, 0.0047g of $Al(sec\text{-}BuO)_3$ was added to the solution and then 4 g of TEOS was added to the solution. The mixture was stirred at room temperature overnight to obtain a sol composition of $80SiO_2$: 3.75dC5: 15KOH: $0.04Al_2O_3$: $9500H_2O$: 320EtOH (Si/Al=1000). When the primary seeds were mixed with the dC5 sol, the targeted silica molar ratio of the primary seeds to the dC5 sol was 1:200. The mixture was hydrothermally treated at 150 °C for 4 days under static conditions.

A tin source was tin (IV) chloride pentahydrate (98 %, Sigma Aldrich). To acquire the precursor sol composition of $80SiO_2$: 3.75dC5: 15KOH: $0.8SnO_2$: $9500H_2O$: 320EtOH (Si/Sn=100), 0.55 g of dC5 was dissolved in 41.1 g of DI water and then 0.204 g of KOH was dissolved. When the dissolution was completed, 0.067 g of tin (IV) chloride pentahydrate was added to the solution and then 4 g of TEOS was added to the solution.

To hydrolyze the TEOS the mixture was stirred at room temperature overnight. When the primary seeds were mixed with the sol, the silica molar ratio of the primary seeds to the dC5 sol was 1:200. The mixture was hydrothermally treated at 150 °C for 6 days under static conditions.

Time-resolved evolution

To understand how the evolution of the primary seeds leads to the formation of nanosheets, one composition of the dC5 sol ($80SiO_2$:3.75dC5: 15KOH: $9500H_2O$: 320EtOH was prepared and the silica molar ratio of the primary seeds to the dC5 precursor sol was 1:200. The evolution was observed every 4 h. The evolution was undertaken at 150 °C for up to 3 days under static conditions. An aliquot was taken out of every sample, diluted with DI water, and mounted on holey carbon film-coated TEM grids (01824, Ted Pella, 400 mesh) for TEM analysis.

Characterization

The morphology of the primary seeds, the secondary seeds, and nanosheets was checked by SEM (Hitachi, S-4700) or TEM (Tecnai, T12).

2.3 Results and discussion

Preparation of primary and secondary seeds

The resulting primary seed particles were *ca.* 50 nm and had irregular shapes, as seen in **Figure 2-1**. In contrast, the secondary seeds had the *b*-elongated cylindrical shape with a base of *ac*-plane and well-defined facets, as shown in **Figure 2-2**. As illustrated in **Figure 2-2D**, the crystallographic axes were indexed by confirming the corresponding FFT (Fast

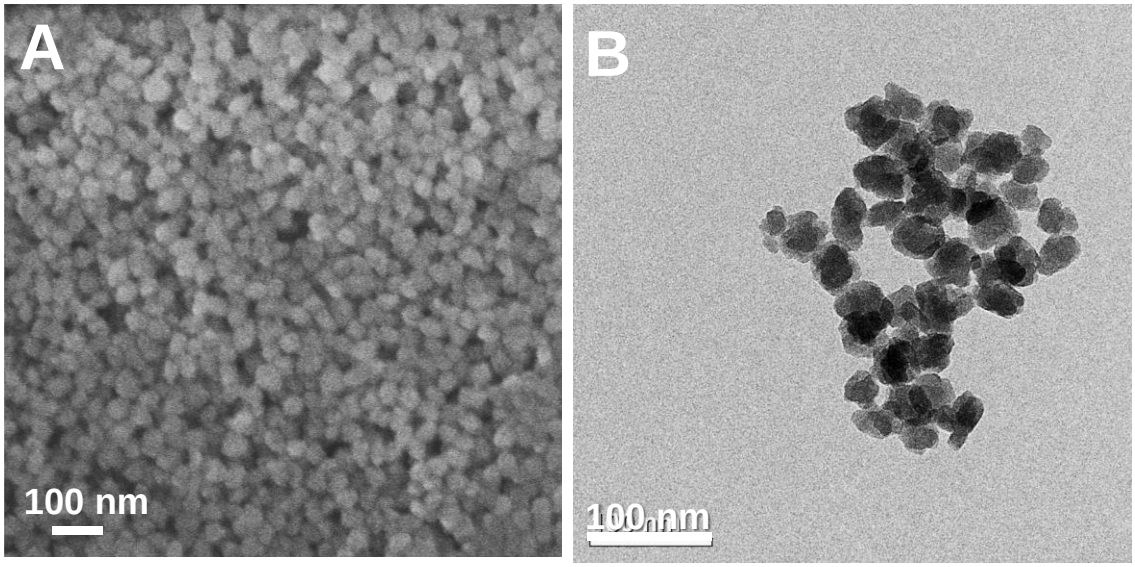

Figure 2-1. A SEM image of the primary seeds (A) and a TEM image of the primary seeds (B). The crystals are approximately 50 nm in size and have irregular shapes.

Fourier Transform). This morphology is consistent with previous studies[70] and it is possibly attributed to the dC5. In general, a TPA molecule, which is a conventional structure-directing agent of MFI, is able to fit into straight *b*-channels and sinusoidal *a*-channels by filling the intersection of the *a*- and *b*- pore channels with the nitrogen atom of the TPA molecule. In contrast, from the perspective of thermodynamics, the dC5 is preferentially fitted into straight *b*-pore channels rather than into sinusoidal a-pore channels.[73] The dC5 has only five carbon atoms between the two quaternary ammonium ions, which produces shorter carbon chains than the dimer of TPA. (It is called dC6 since it has six carbon atoms between the two quaternary ammonium ions). Consequently, fitting in the straight *b*-channel of dC5 is more energetically favorable than the sinusoidal *a*-channel leading to preferential growth along the *b*-direction.[73]

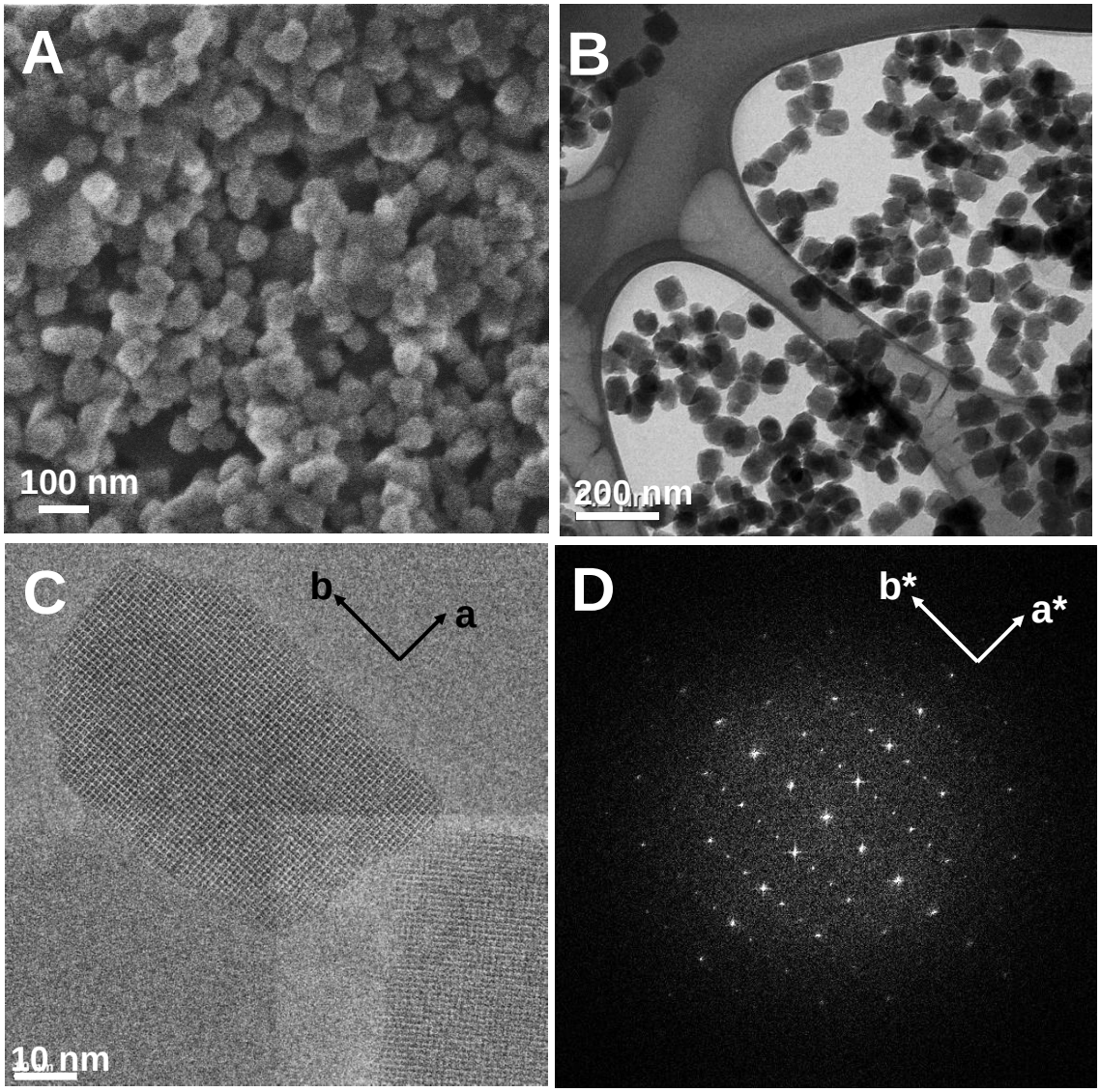

Figure 2-2. A SEM image of the secondary seeds (A) and a TEM image of the secondary seeds (B). A HRTEM (High Resolution TEM) image of the secondary seeds (C) and a corresponding FFT (Fast Fourier Transform) image (D). The HRTEM image, C, and FFT image, D, were obtained by Prashant Kumar.

Nanosheet synthesis from two-step growth

The secondary seeds were mixed with hydrolyzed dC5 sol and then hydrothermally treated. This produced nanosheets that had a thickness of *ca.* 5 nm (measured by AFM) (**Figure 2-3C middle**) and a lateral size of *ca.* 2 μm (**Figure 2-3A**). Scanning through the

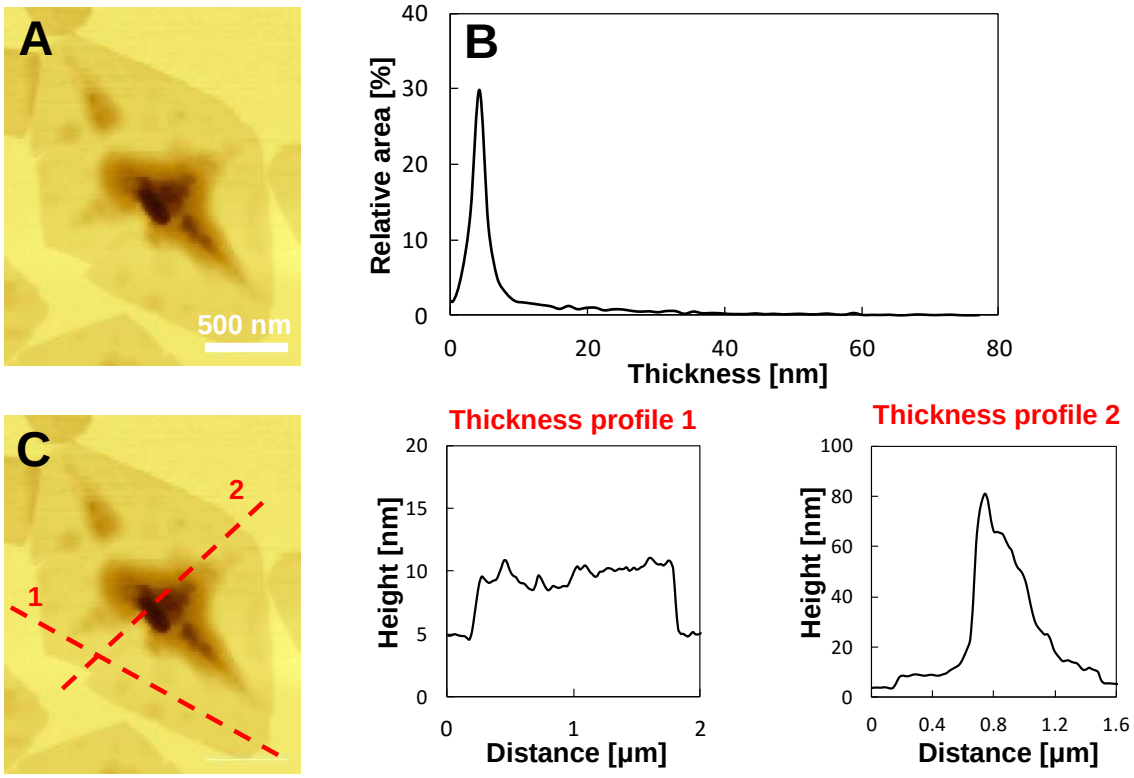

Figure 2-3. An AFM image of MFI nanosheet (A), height distribution (B), line scanning for thickness profiles (C left), thickness of the nanosheet corresponding to the line scan 1 (C middle), and thickness of the center of the nanosheet corresponding to the line scan 2 (C right). Based on the height distribution (B), the nanosheet area is approximately 75 % within the entire sheet area. On the basis of the AFM thickness profile, the nanosheet is approximately 5 nm thick (C middle), and the thick center produced by the seed is approximately 75 nm thick (C right). All images were acquired by Dr. Donghun Kim.

center of the particle (see **Figure 2-3C right)** determined that its thickness differs from that of the nanosheet portion. That is, at its center the secondary seed particle is embedded and it is thicker (*ca.* 75 nm) than the nanosheet area. This thick part at the center cannot be avoided since the synthesis is developed from seed crystals. To determine the thickness distribution the number of pixels that correspond to the thickness of a nanosheet particle was counted. Most of the nanosheet is 5nm thick. As noted in

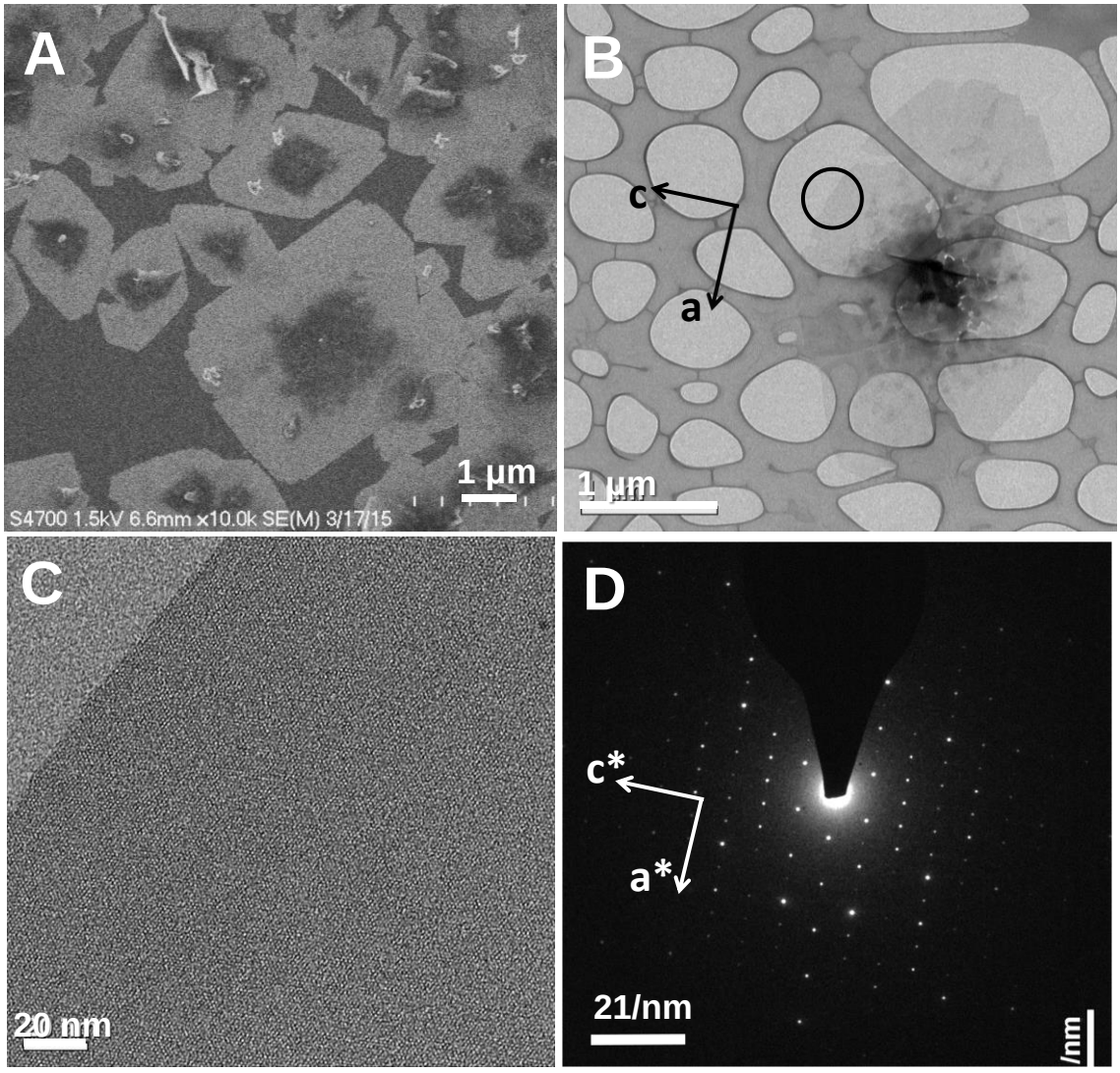

Figure 2-4. A SEM image of MFI nanosheets deposited on a silicon wafer (A), a TEM image of a MFI nanosheet (B), a high magnification TEM image of area indicated by a circle in B (C), and a corresponding electron diffraction pattern (D). The high magnification TEM image (C) indicates crystallinity. The electron diffraction pattern D is *b*-oriented pattern, which reveals that the thin dimension of the nanosheet is along *b*-axis.

Figure 2-3B, approximately 75% of the nanosheet lies within the particle, and this is much larger than the maximum nanosheet area produced under the top-down approach.

From the electron diffraction pattern of the thin nanosheet area (**Figure 2-4D**), one can determine that the thin dimension is along *b*-axis. From the indexing of the corresponding electron diffraction pattern (**Figure 2-4D**) it can determine that the long dimension of the nanosheets corresponds to the *a*-axis (**Figure 2-4B**). In contrast, in conventional MFI synthesized from TPA, the fastest crystal growth rate occurs along *c*-axis, which leads to an elongated crystal morphology along the *c*-axis.[74] **Figure 2-4A** shows the *b*-oriented nanosheet deposition on a silicon wafer.

Hereafter the nanosheet synthesis from secondary seeds is denoted as "two-step growth." This reflects the fact that from the primary seeds two steps—preparing secondary seeds and preparing nanosheets—are employed to acquire the final product, nanosheets. Completion of the two-step growth takes 7 days, which does not include preparing the primary seeds. To shorten the synthesis time, the secondary seeds were replaced with primary seeds, which shortens by three days the hydrothermal treatment of secondary seeds. This is called as "one-step growth."

Nanosheet synthesis from one-step growth

In one-step growth, the primary seeds were mixed with the dC5 precursor sol to synthesize nanosheets. In the one-step method, the amount of silica source from the dC5 precursor sol that is exploited to convert most of the primary seeds to nanosheets is higher than that used in the two-stop growth. When the same or a lesser amount of this silica source was mixed with the primary seeds and subsequently hydrothermally treated, most of the seed particles did not grow to nanosheets. As indicated in **Figure 2-5A** and **B**, they remained ungrown (A; the silica molar ratio of the primary seeds to the dC5

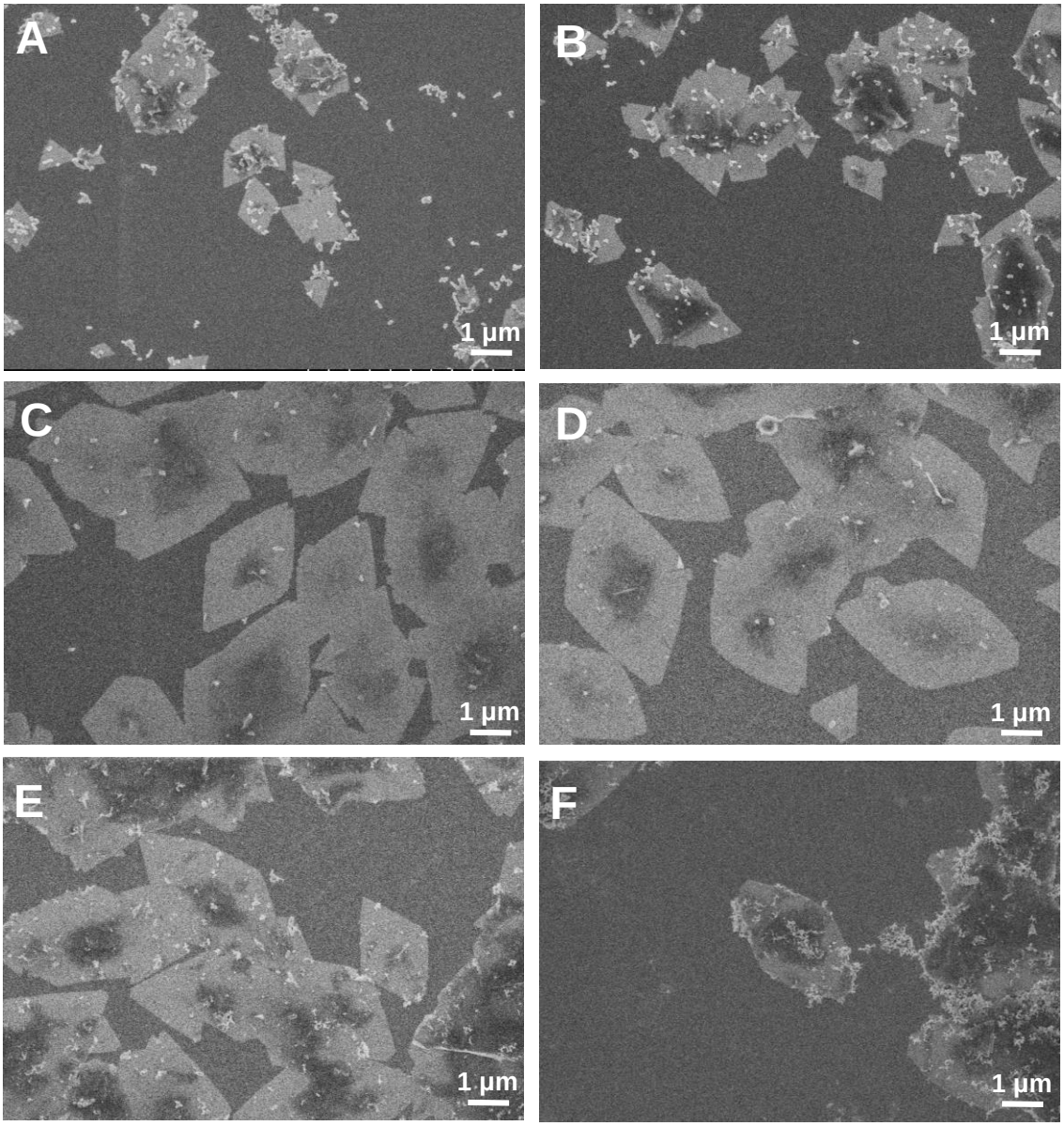

Figure 2-5. SEM images of MFI nanosheets grown from the silica molar ratio of the primary seeds to the dC5 precursor sol=1:30 (A), 1:60 (B), 1:200 (C), 1:400 (D), 1:600 (E), and 1:800 (F). Ungrown seed particles appear in the case of the low silica molar ratio of the primary seeds to dC5 sol (A and B). Amorphous silica precursor particles are observed in the case of the high silica molar ratio of the primary seeds to dC5 precursor sol (E and F).

precursor sol=1:30 and B; 1:60). Where nanosheets did grow from the low silica source of the dC5 precursor sol, as presented in **Figure 2-5A** and **B**, their lateral size was smaller

than those grown from the higher silica source of the dC5 precursor sol. Perhaps this occurred attributed to the low nutrients for crystal growth provided by the dC5 precursor sol, which has a low silica concentration. As silica concentration from the dC5 precursor sol increased, most of the seeds were converted to nanosheets, but after critical point (the silica molar ratio of the primary seeds to the dC5 precursor sol=1:600), plenty of amorphous silica particles were formed (**Figure 2-5E** and **F)**. Since the induction period of MFI crystals from dC5 is longer than that of TPA[71], excessive nutrients from the silica source might not have time to nucleate during hydrothermal treatment. Consequently, the amorphous silica precursor particles can remain without formation of MFI crystals. In one-step synthesis, two-step synthesis is not needed for nanosheet synthesis to occur. In other words, one-step synthesis is an effective and alternative to two-step synthesis.

The thickness profiles of the one-step grown nanosheet were determined by AFM analysis, as shown in **Figure 2-6**. **Figure 2-6B** shows that the thickness of the nanosheet is approximately 5 nm. This is identical to the two-step grown nanosheet. **Figure 2-6C** describes thickness profiles with a line scan passing through the central part of the nanosheet. The thickness of the central part, including the seed from one-step growth, is thicker than that acquired from two-step growth, but the differences are insignificant since both are approximately 100 nm. **Figure 2-6C** shows the bimodal thickness profile since a seed crystal was deposited onto the nanosheet. The thickness profiles from AFM analysis indicate that during one-step growth, the nanosheet synthesis time can be shortened with no compromise in quality. The nanosheets described in this dissertation

were grown from primary seeds using the one-step growth method unless it is referred to as two-step growth method.

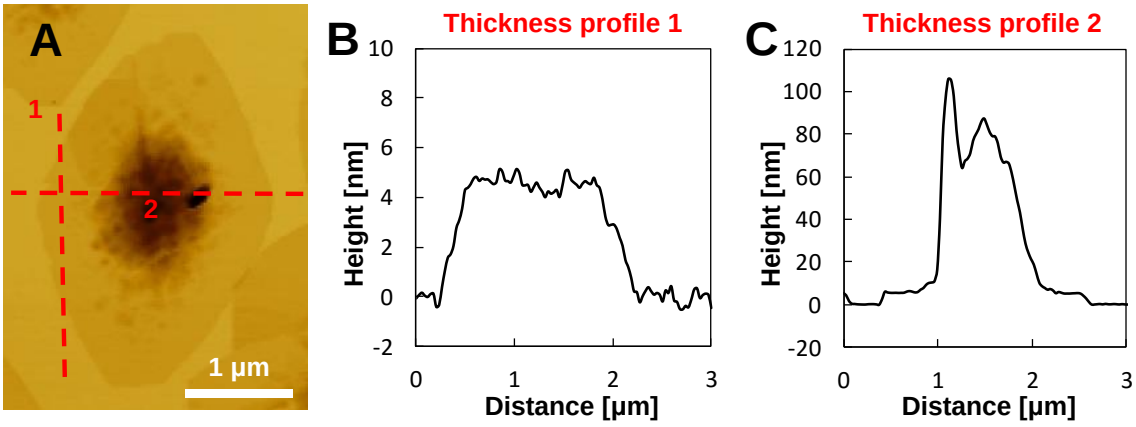

Figure 2-6. An AFM image of the MFI nanosheet (A), the thickness profile of the nanosheet that corresponds to the line scan 1 (B), and the thickness profile of the center of the nanosheet that corresponds to the line scan 2 (C). All images were acquired by Dr. Donghun Kim.

An effect of pH on nanosheet synthesis

Parametric studies were conducted in order to optimize three parameters of nanosheet quality: 1) no or few ungrown seeds remaining; 2) no or few intergrown particles; and 3) a high area of thin nanosheet within an entire particle. To achieve this, impacts of pH of the dC5 precursor sol were investigated. At low pH (sample 1 in **Table 2-1**), only amorphous silica precursor particles were obtained since the pH value was not high enough to facilitate zeolite crystallization (**Figure 2-7A)**. As pH gradually increased, zeolite particles crystallized, which led to the co-existence of nanosheets and amorphous silica precursor particles (**Figure 2-7B** and **C**). At a pH higher than 11.54, nanosheets were the major products and no or few amorphous silica precursor particles co-existed

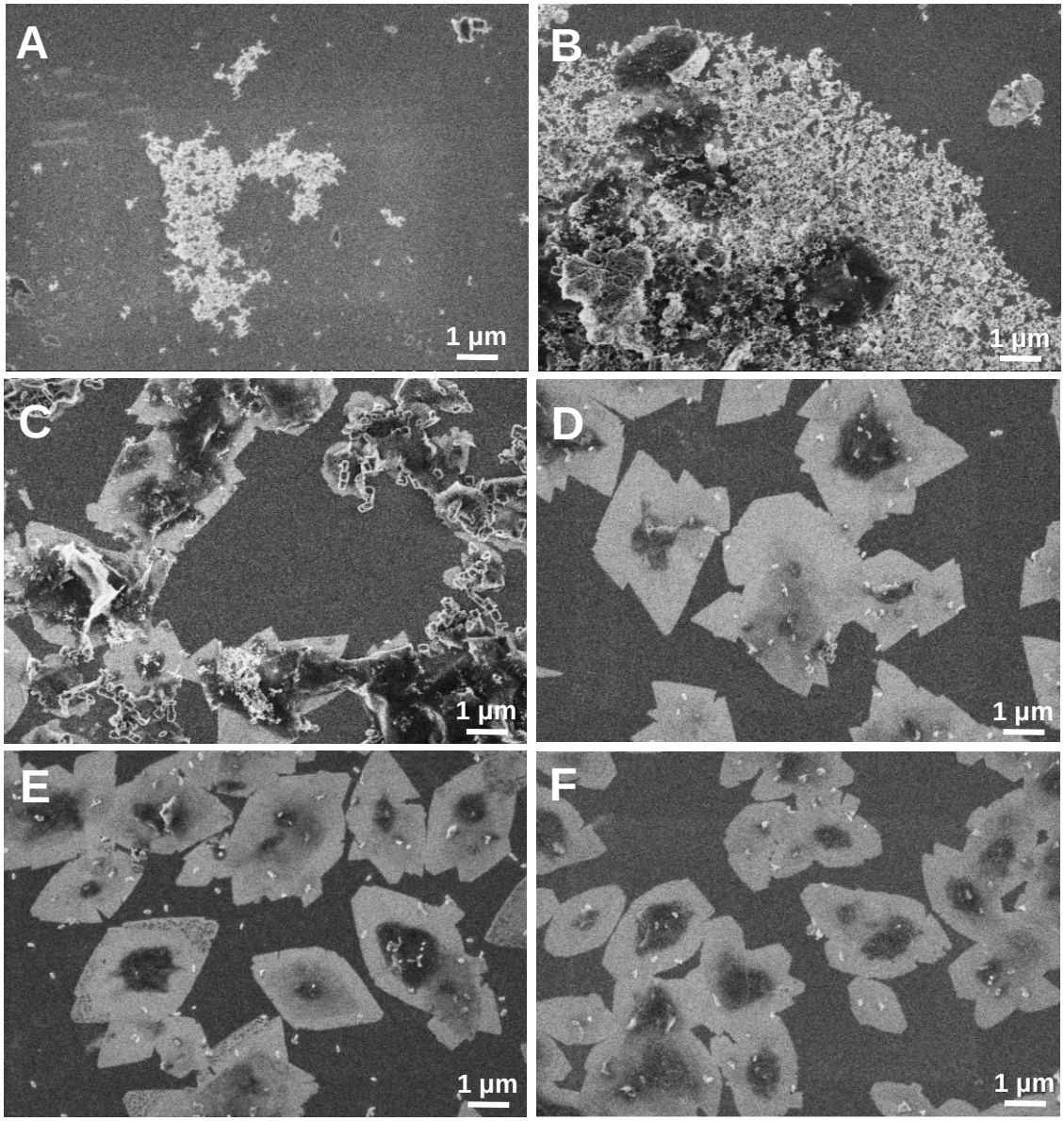

Figure 2-7. SEM images of sample 1 (A), sample 2 (B), sample 3 (C), sample 4 (D), sample 5 (E) and sample 6 (F) of Table 2-1. At low pH (A and B), major product is amorphous silica precursor particles.

(**Figure 2-7D**, **E** and **F**). From the study of pH effects, the optimal dC5 precursor sol composition was identified as $80SiO_2$: 3.75dC5: 15KOH: $9500H_2O$: 320EtOH.

The influence of cations of base on nanosheet synthesis

In zeolite synthesis, a base is employed as a mineralizing agent and sodium hydroxide and potassium hydroxide are the conventional mineralizing agents. The cations of bases influence zeolite synthesis since they interact with zeolite frameworks in different ways.[75] To probe the effects of the size of cations on nanosheet synthesis, as mineralizing agents four different cations of base that have +1 charge were employed: sodium (Na^+), potassium (K^+), cesium (Cs^+) and rubidium (Rb^+) ions.

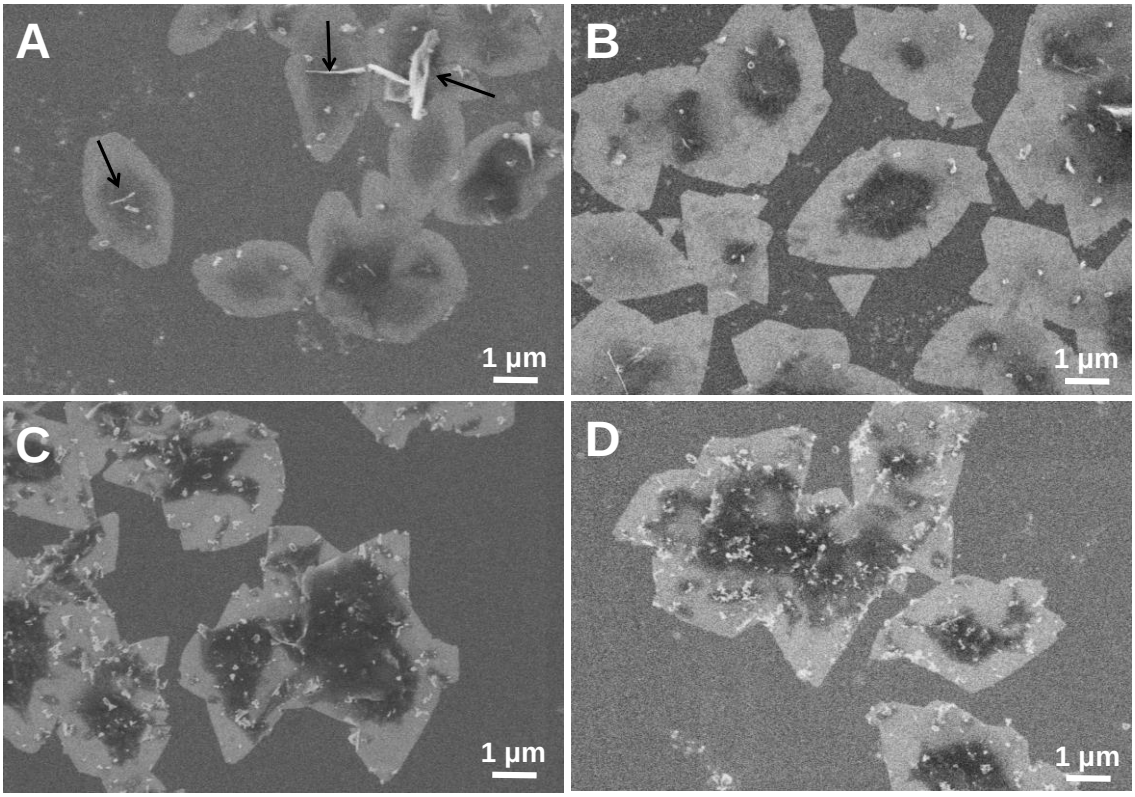

Figure 2-8. SEM images of MFI nanosheets that have been synthesized with sodium hydroxide (A), potassium hydroxide (B), cesium hydroxide (C) and rubidium hydroxide (D). Arrows in A indicate twinning.

As is well known, in the presence of sodium ions smaller zeolite crystals are produced with twinning.[75] In contrast, bigger ions such as potassium, cesium and rubidium ions favor the formation of large single crystals.[75] Consistent with what has been reported in the literature,[75] **Figure 2-8A** shows that nanosheets produced in the presence of the sodium ions are relatively small. Moreover, the nanosheets appeared to be twinned (see the arrows in **Figure 2-8A**), which is not desirable for membrane applications. **Figure 2-8C** and **D** show that, compared to potassium hydroxide (**Figure 2-8B**), increasing cation size through the use of mineralizing agents such as cesium and rubidium does not reduce seed thickening at the center. Furthermore, the lateral size of the nanosheets in the presence of cesium and rubidium ions is as large as nanosheets produced when potassium hydroxide is the mineralizing agent. As cation size increases, it is likely to form amorphous silica precursor particles (**Figure 2-8**). The formation of amorphous silica precursor particles is pronounced when the biggest cation, rubidium, is present (**Figure 2-8D**). Perhaps this occurs since there is less interaction between $dC5^{+}$ and silicate anions when large cations that form competitive interactions with silicate anions are present.[75] The results suggest that when potassium hydroxide is present as a mineralizing agent synthesized nanosheets qualify as high quality nanosheets.

How crystallization temperature affects nanosheet synthesis

A wide range of synthesis temperatures from 150 °C to 170 °C were probed for optimization of nanosheet quality. As synthesis temperature increased, nanosheet particle size increased along with pronounced seed thickening at the center as exhibited in **Figure 2-9**. With temperature, the crystallization rate increased leading to bigger crystal sizes.

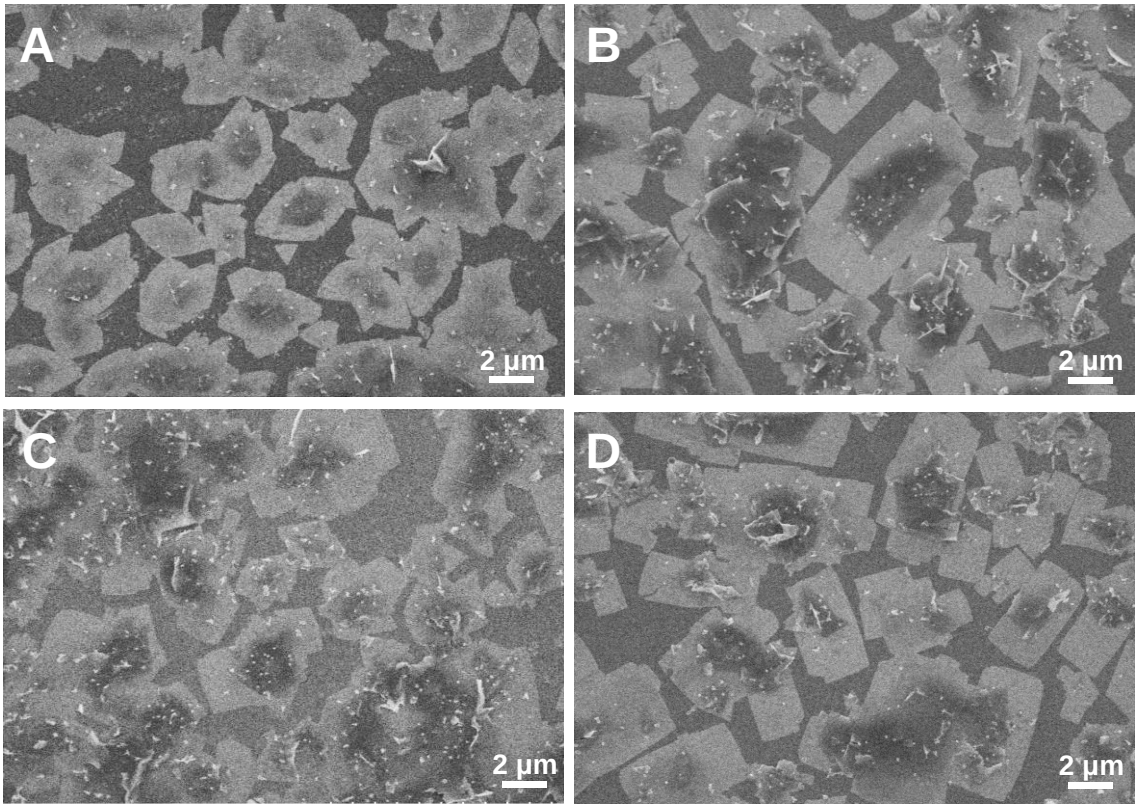

Figure 2-9. SEM images of deposited MFI nanosheets on silicon wafers synthesized at 150 °C (A), 160 °C (B), 165 °C (C), and 170 °C (D).

Besides the crystal size, the rising temperature promoted mass transfer in the system and possibly resulting in significant seed thickening at the center as well. Therefore, nanosheets synthesized at 150 °C show the least seed thickening.

How crystallization time affects nanosheet synthesis

Crystallization time was manipulated to reduce the seed thickening at the center of the nanosheets. The crystallization time was reduced long enough to obtain nanosheet crystals, and it was prolonged to verify the impact of crystallization time on seed thickening.

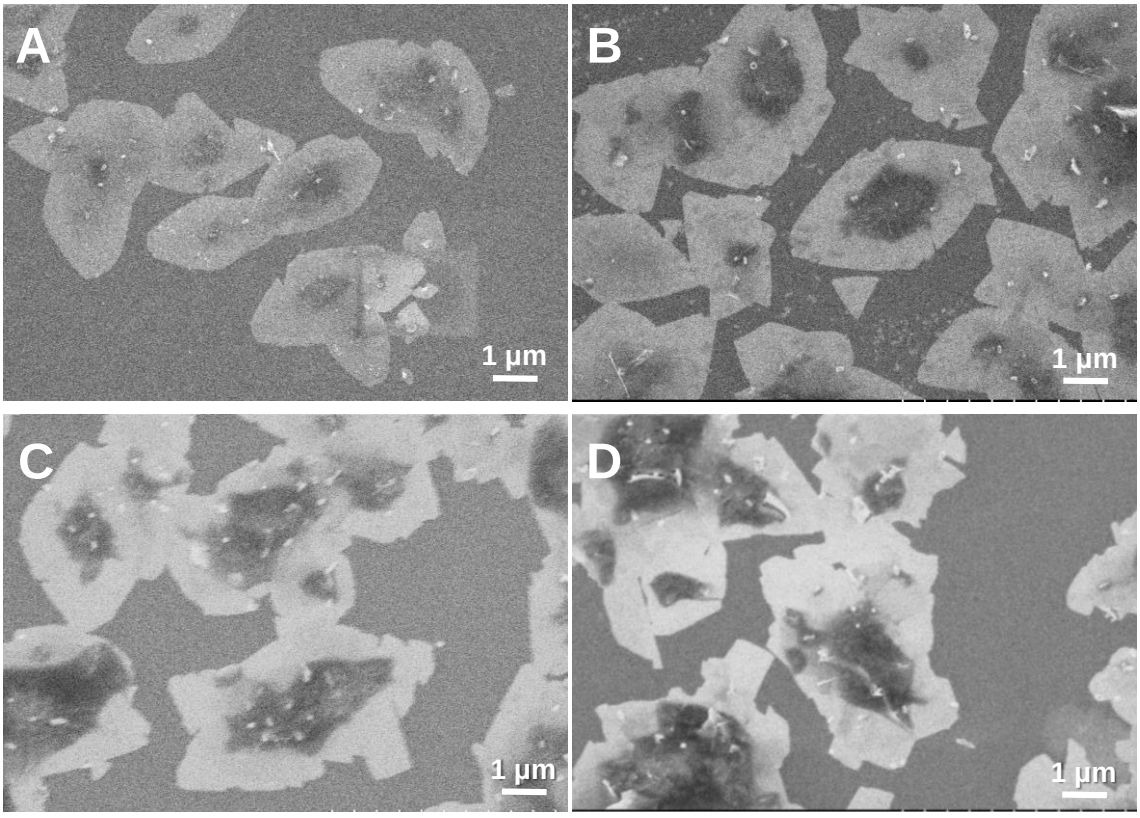

Figure 2-10. SEM images of deposited MFI nanosheets on a silicon wafer. Nanosheets synthesized for 52 h (A), 3 days (B), 20 days (C), and 31 days (D).

The size of resulting nanosheets produced during the short crystallization time (52 h, **Figure 2-10A**) was smaller than obtained during the longer crystallization time, but it was micron dimension. Moreover, the seed thickening at the center of nanosheets was less pronounced compared to nanosheets produced during the longer crystallization time. Interestingly, when the crystallization time was prolonged to 20 days (**Figure 2-10C**) and 31 days (**Figure 2-10D**), the lateral size of the nanosheets produced did not increase beyond the size of nanosheets crystallized for 3 days. This suggests that for 3 days crystallization is saturated. However, seed thickening appeared to be significant when crystallization was prolonged. This result suggests that seed thickening occurs during a

late stage of nanosheet synthesis and that when synthesis is shortened seed thickening is circumvented.

Synthesis in the absence of seed crystals

In the bottom-up synthesis of MFI nanosheets, the SDA, dC5 plays a crucial factor but seed crystals can play a critical role, too. Okubo's group describes a MFI synthesis with dC5 wherein a different composition of dC5 precursor sol in the absence of seed crystals produced intergrown cystals.[71]

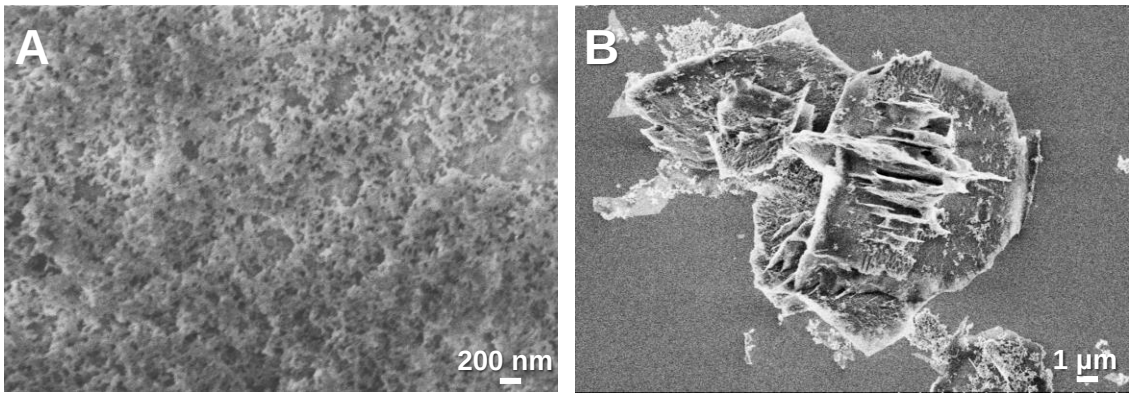

Figure 2-11. SEM images of products from the dC5 precursor sol in the absence of seed crystals. For 3 day hydrothermal treatment, only amorphous silica precursor particles were observed (A). Intergrown nanosheets were acquired for 12 day crystallization (B).

To verify the role of seed crystals, a synthesis from dC5 sol in the absence of seed crystals was carried out; the composition was $80SiO_2$: 3.75 dC5: 25KOH: $9500H_2O$: 320EtOH. Since the induction period of dC5 precursor sol is longer than that of the TPA precursor sol,[71] in the absence of nuclei (seeds), only amorphous silica precursor particles were formed for the 3 day seeded-growth crystallization (**Figure 2-11A)**. Due to the longer induction period, I chose the prolonged crystallization time (12 days) was chose in

order to obtain MFI crystals rather than amorphous silica precursor particles. Consequently, intergrown nanosheet crystals rather than single nanosheets were formed (**Figure 2-11B),** which is consistent with trends reported in the previous work.[71] This may stem from uncontrolled nucleation in the absence of seeds.

How the size of seed crystals affects nanosheet synthesis

Smaller MFI seed crystals, *ca.* 20 nm, were prepared from fragmented 3DOm-i MFI crystals (**Figure 2-12A** and **B**) with the expectation that smaller seeds would help reduce seed thickening of the central part of nanosheets. Unexpectedly, however, nanosheets synthesized from the smaller seeds, i.e., the fragmented 3DOm-i MFI, did not show improved seed thickening at the center (**Figure 2-12C** and **D)**. The size of seeds at the center of nanosheets grown from 3DOm-i MFI seeds, as shown in **Figure 2-12D**, was comparable to that of nanosheets grown from regular primary seeds. It is concluded that starting with even smaller seeds would not eliminate seed thickening at the center of nanosheets since prior to nanosheet growth seeds grow to a critical size (~100 nm). This process apparently is not affected by the primitive size of seed crystals. The growth of seed crystals up to critical size always occurs before nanosheet growth, no matter how small the seed crystals. Thus, there is always thick seed and seed thickening at the center. In the last section of this chapter the sequence of nanosheet growth is discussed in detail. To explore how bigger seed crystals affect nanosheet growth, approximately 120 nm seed crystals were prepared (**Figure 2-13A)**. The nanosheets synthesized from bigger seeds had pronounced seed thickening at their centers (**Figure 2-13B**) than nanosheets synthesized from regular primary seeds.

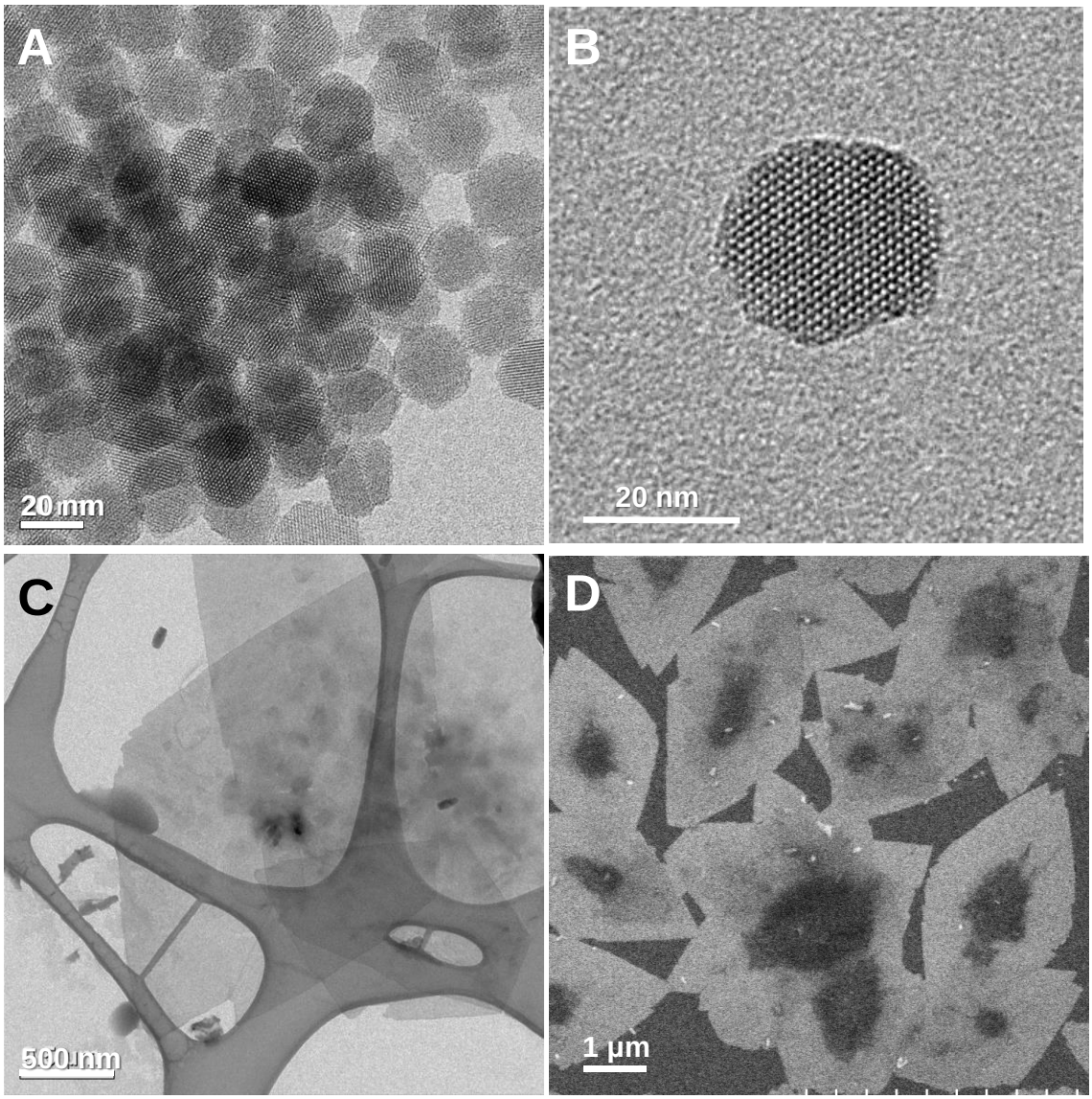

Figure 2-12. TEM images of 3DOm-i (3 Dimensionally Ordered Mesoporous imprinted) MFI seeds as synthesized (A), single crystals from disassembly of 3DOm-i MFI (B), and MFI nanosheets prepared from the fragmented single 3DOm-i MFI crystals (C). A SEM image of nanosheets synthesized from the 3DOm-i MFI seeds (D). The 3DOm-i MFI seeds were prepared by Prof. Wei Fan at University of Massachusetts Amherst. Disassembly of the 3DOm-i MFI was carried out by Dr. Pyung-Soo Lee at Korea Research Institute of Chemical Technology (KRICT).

Within an entire nanosheet particle the portion that was thin was lower than in nanosheets grown from regular primary seeds. In the case of seeds smaller than 100 nm (the primary

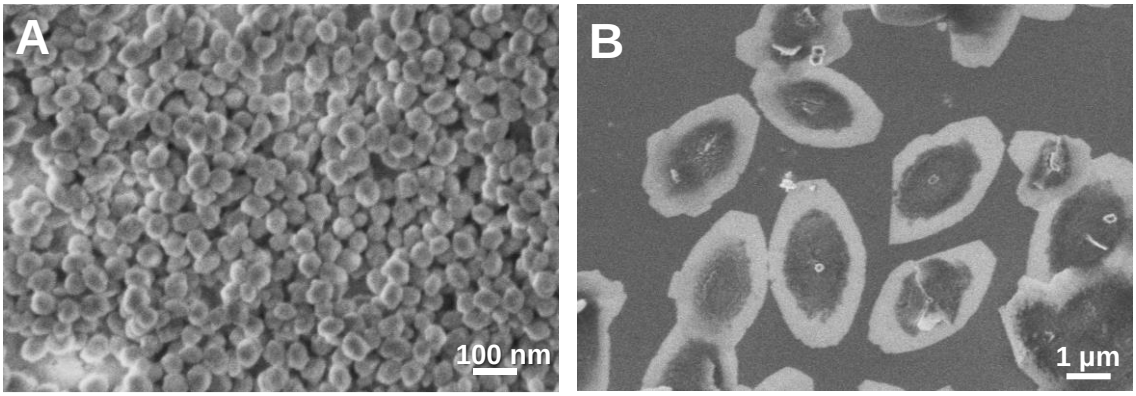

Figure 2-13. SEM images of bigger seed crystals, *ca.* 120 nm (A) and MFI nanosheets synthesized from the bigger seeds (B).

seeds and the fragmented 3DOm-i MFI seeds), the size of seeds at the center of nanosheets was not affected by initial seed size. In contrast, seeds larger than 100 nm produced larger seeds at the center of the nanosheets and seed thickening. This suggests that nanosheets grown from large seeds and nanosheets grown from regular primary seeds grow in the same manner. In other words, seeds at the center of nanosheets became larger, whatever their initial size. This finding supports the hypothesis that seed crystals grow until a critical point is reached, at which point nanosheet growth occurs.

The influence of the morphology of seed crystals on nanosheet synthesis

To examine the influence of seed crystal morphology on nanosheet synthesis, SPP consisting of 1 unit cell thick (2 nm) MFI nanosheets that have a house-of-card assembly was prepared (**Figure 2-14A** and **B**). If the morphology of the seed crystal has a significant impact on the nanosheet synthesis, the resulting product should reveal a morphology similar to that of the seed crystals. The resulting nanosheets, however, did not show intergrown structure comparable to the seeds, SPP (**Figure 2-14C**). Instead, they were similar to the nanosheets prepared from primary seeds in the respect that they

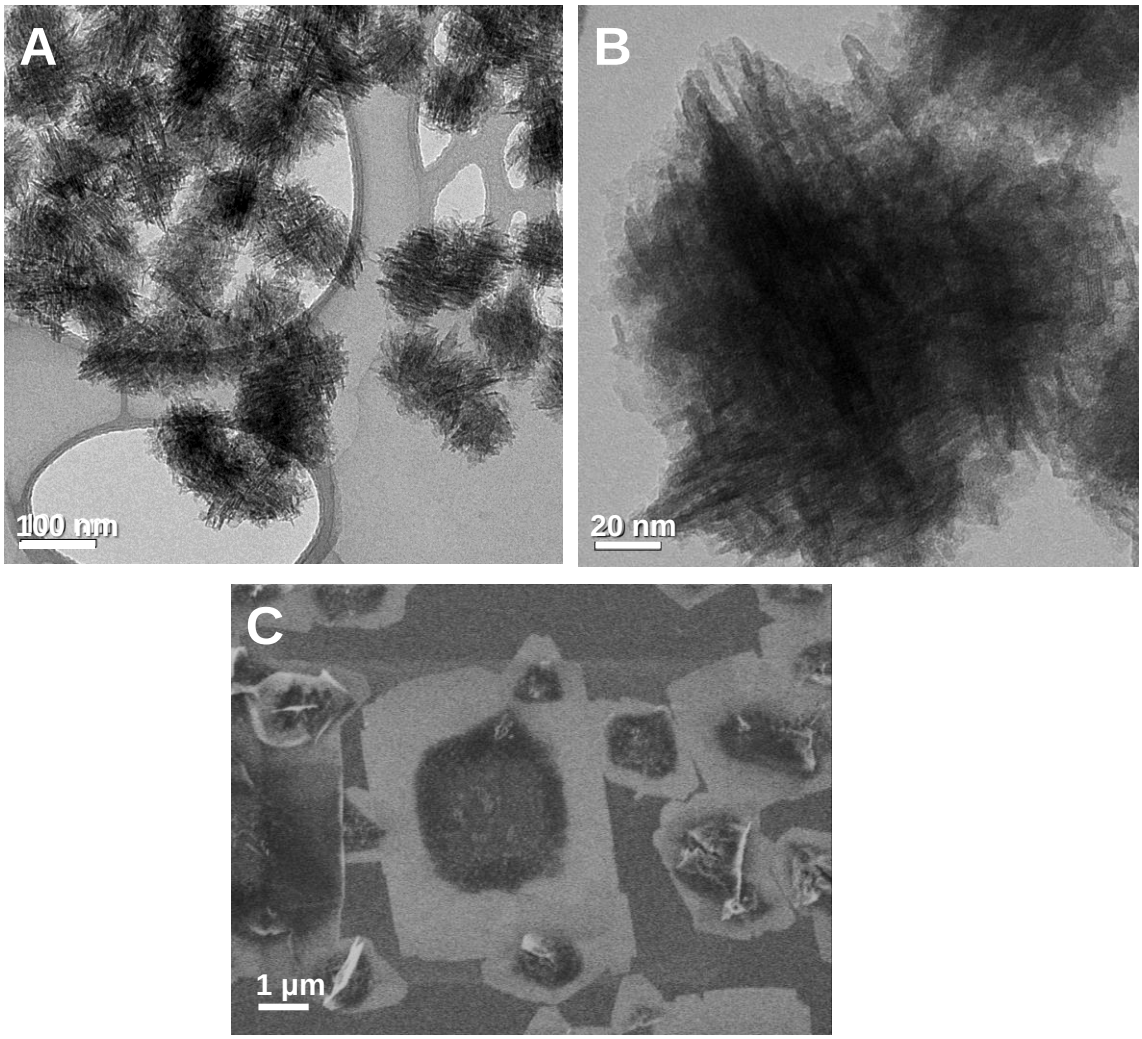

Figure 2-14. TEM images of SPP at low magnification (A), at high magnification (B), and a SEM image of MFI nanosheets synthesized from the SPP (C).

showed no significant intergrowth. The result indicates that SDA, dC5, is the key factor that determines crystal morphology, and this leads to nanosheets from seeded-growth. Although the morphology of the seed crystals did not play a critical role in nanosheet synthesis, the size of seed crystals affected synthesis in the manner discussed above. The seeds embedded at the center of nanosheets synthesized from the SPP (**Figure 2-14C**) appears to be larger than those found in nanosheets synthesized from primary seeds.

Perhaps this is attributed to that the particle size of the SPP (approximately 100 nm) is greater than that of primary seeds.

Heteroatom insertion into the MFI framework

The synthesized MFI nanosheets described above are all pure silica type crystals for membrane applications. Now the results of heteroatom insertion are described. When heteroatoms are incorporated into the zeolite framework, catalytic activity occurs.[4,72] In the case of both membranes and catalysts, nanosheets can shorten molecular diffusion length along the thin dimension, and this overcomes diffusion limitations.[4,72,76,77]

Figure 2-15A shows aluminosilicate MFI nanosheets with a ratio of Si/Al=1000. Since the aluminum atom reduces the crystallization rate, crystallization time to pure silica nanosheets (3 days) resulted in amorphous silica precursor particles. When the crystallization time was prolonged to 4 days, aluminosilicate MFI nanosheets were obtained that had a similar morphology. That is, seed crystals were embedded at the center of nanosheets and seed thickening occurred.

Figure 2-15B exhibits tin-inserted MFI nanosheets that have a ratio of Si/Sn=100 and whose nanosheet morphology resembles that of pure silica MFI nanosheets. Since the crystallization rate of the tin-inserted MFI was slower than that of pure-silica MFI, plenty of amorphous silica precursor particles were observed even after 6 day crystallization. Compared to pure-silica nanosheets, tin-inserted nanosheets had pronounced seed thickening at their centers associated with the extended crystallization time.

In the case of catalyst applications, researchers should carry out parametric studies of silicon to heteroatom ratios, and they should optimize synthesis conditions. This work is beyond the scope of this dissertation.

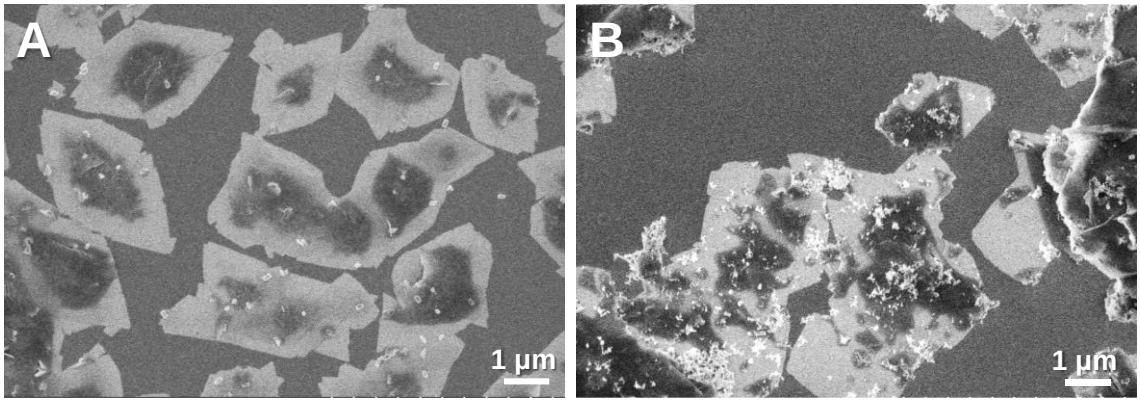

Figure 2-15. SEM images of aluminum-inserted (Si/Al=1000) MFI nanosheets (A) and tin-inserted (Si/Sn=100) MFI nanosheets (B).

The time-resolved sequence of the evolution of primary seeds

To understand the growth of the nanosheets, the time-resolved sequence of the evolution of primary seeds upon hydrothermal treatment with dC5 precursor sol was observed by TEM. At the initial stage (**Figure 2-16A**), the primary seeds and the small amorphous silica particles (from the dC5 sol), which generally form during the hydrolysis of TEOS as part of zeolite synthesis,[21,22,25,30-33] co-existed. As the primary seeds underwent hydrothermal treatment, they grew into bigger seeds that in size and morphology resemble secondary seeds (**Figure 2-16B**). In contrast to the primary seeds, the facets of the grown seed were well-defined and sharpened. After the longer hydrothermal treatment primary seeds grew to a size larger than that of secondary seeds (**Figure 2-**

16C). **Figure 2-16C** illustrates a core-shell structure of the grown seed. The size of the core is comparable to that of primary seeds. At the middle stage of evolution, further hydrothermal treatment led to the emergence of a branch on a facet of the grown seeds rather than to the further growth of the seeds (**Figure 2-16D**). The branch (**Figure 2-16D**) is approximately 5 nm thick, which is the thickness of the nanosheets. Moreover, the branch revealed pentasil chains that are building units of the MFI framework, suggesting that the branch marks the onset of nanosheet growth.

At the late phase of the evolution, and following the emergence of the branch, the nanosheet surrounded the grown seed and grew in a circular way (**Figure 2-17**). Eventually the nanosheets completely surrounded the grown seed (**Figure 2-17D**). Immediately after the nanosheets enveloped the grown seed, it remained relatively small and displayed no seed thickening at its center (**Figure 2-17D**). This suggests that the seed thickening occurs after the completion of nanosheet growth. While crystallization occurred continuously after the grown seed was enveloped, nanosheets were then continuously exposed to the dC5 precursor sol, which contains abundant nutrients for crystallization, which led to secondary nucleation and crystallization on the top surface of the nanosheets.

The arrows in **Figure 2-18** indicate that island formation on the top of the completed nanosheet due to secondary nucleation and crystallization leading to variations in the thickness of the nanosheet. Since the secondary nucleation takes place at a late stage of nanosheet formation, island formation perhaps can be suppressed by manipulating crystallization time.

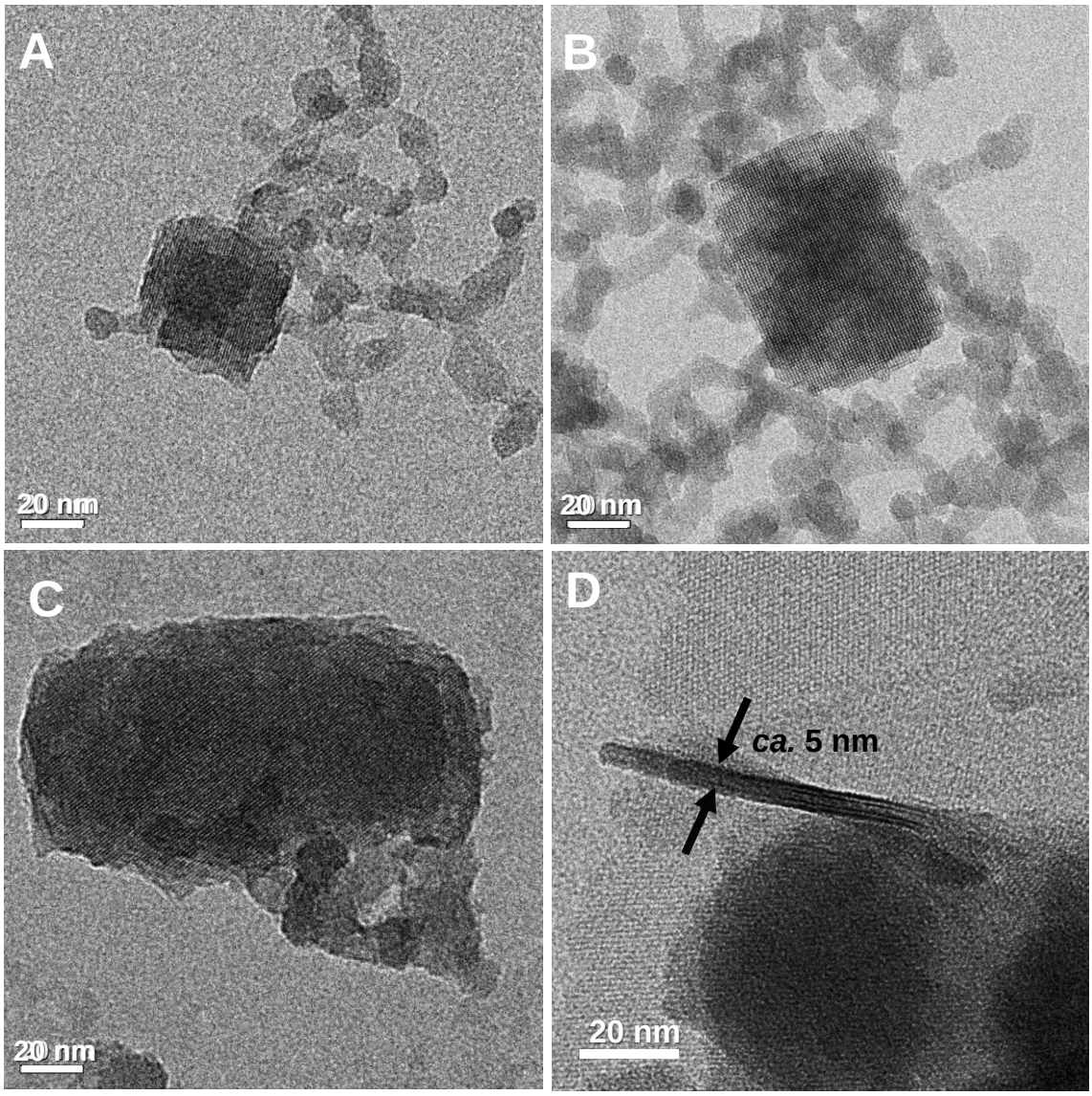

Figure 2-16. TEM images of the sequential evolution of primary seeds. At the initial stage of evolution, amorphous silica precursor particles exist with the primary seed (A). The primary seed grows to the secondary seed (B). The primary seed grows even bigger than the secondary seed and reveals its core-shell structure (C). At the middle stage of the evolution, a branch emerges out of a facet of the grown seed (D).

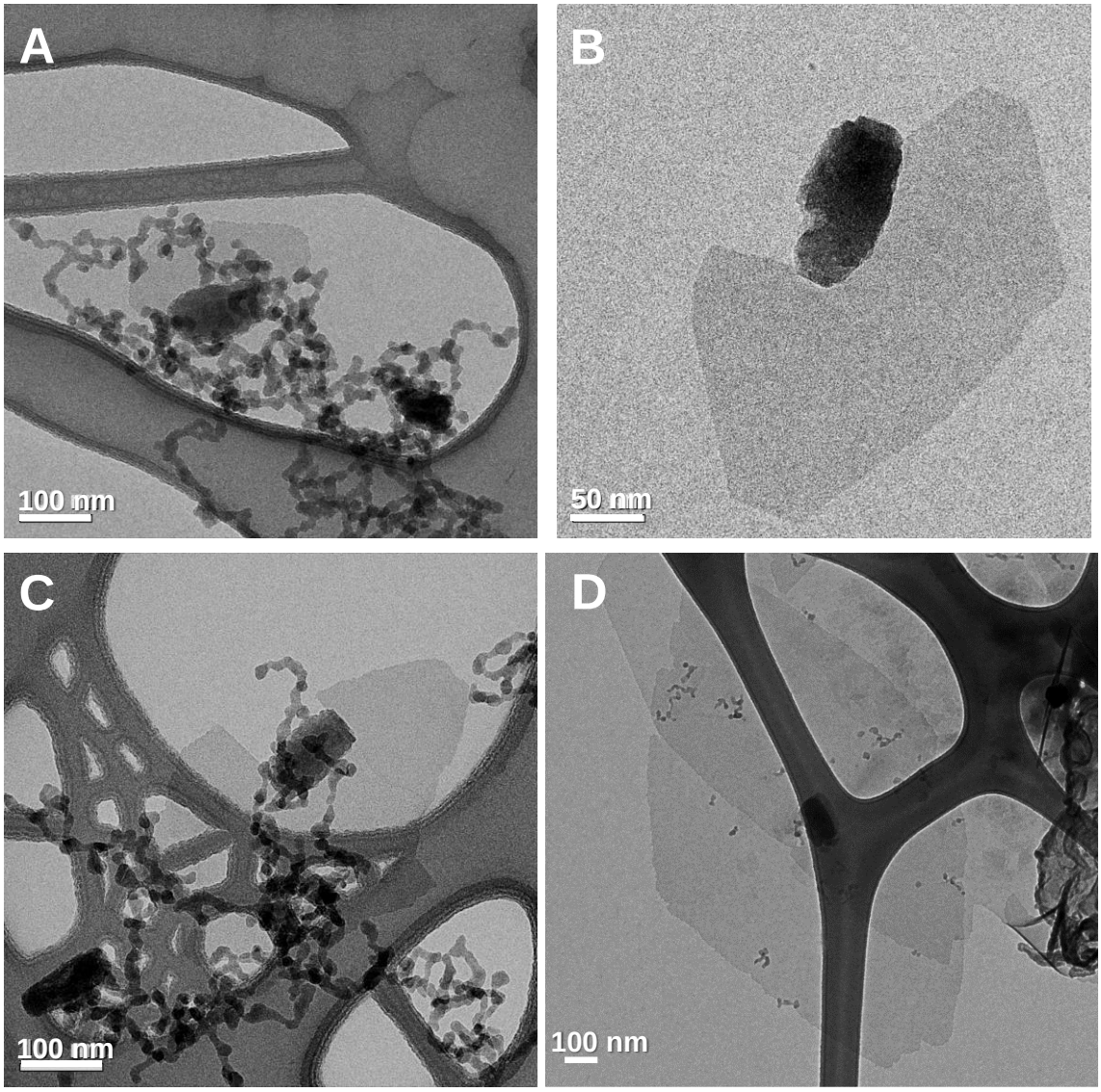

Figure 2-17. TEM images of the late stage of the evolution. At the beginning of emergence of the nanosheet out of the seed (A), gradual growth of the nanosheet around the seed in a circular way (B and C), and completion of the growth of the nanosheet around the seed (D).

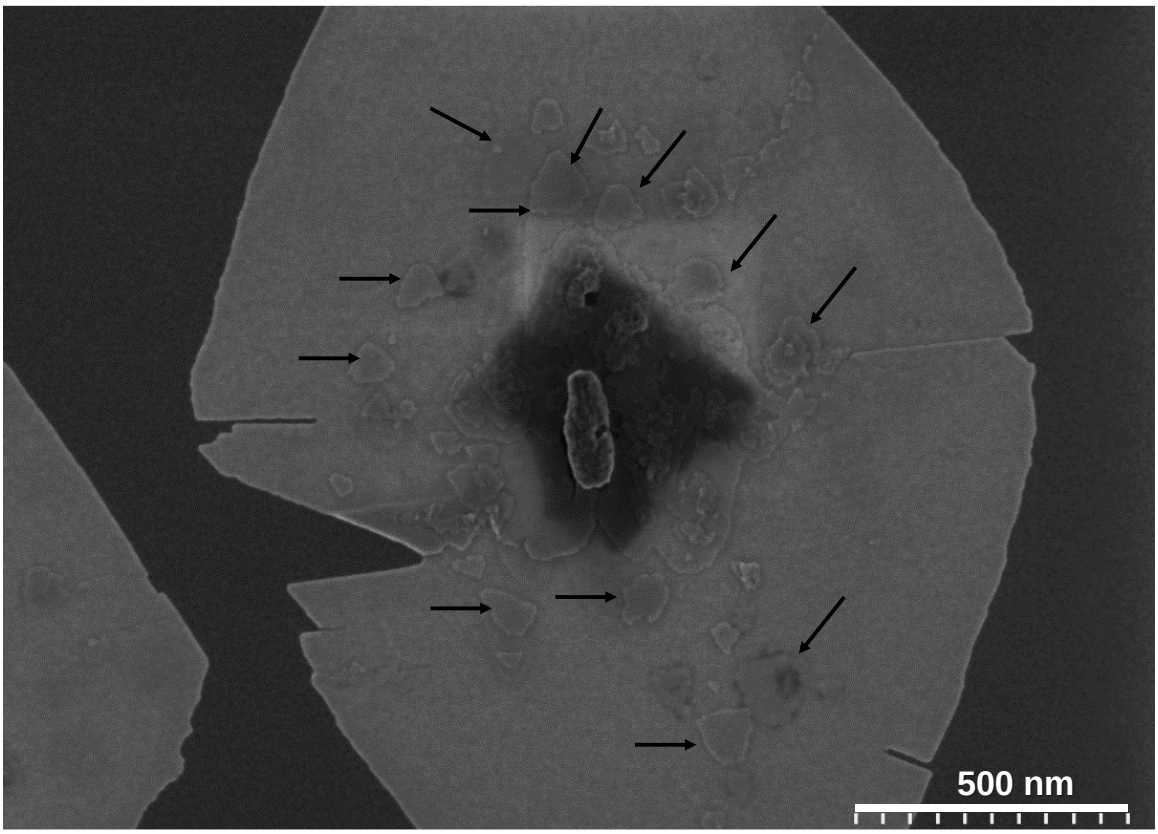

Figure 2-18. A high resolution SEM image of nanosheets. Arrows indicate island formation atop nanosheets upon the secondary nucleation. The image was obtained by Dr. Donghun Kim.

2.4 Conclusion

This chapter describes the successful bottom-up synthesis of MFI nanosheets through seeded-growth. The yield from synthesis is higher than that of nanosheets produced using the top-down approach. Nanosheet thickness along the *b*-axis is approximately 5 nm, which is thicker than the thickness of nanosheets produced using the top-down strategy (3 nm). The lateral size is larger, too. The procedure is environmentally-friendly and easy to process since nanosheets are suspended in water as synthesized forms.

The primary seeds are prepared from conventional SDA, TPA, and are treated with dC5 precursor sol in order to prepare the secondary seeds. From both primary seeds and

secondary seeds, MFI nanosheets are synthesized after the hydrothermal treatment of the mixture of seeds and the dC5 precursor sol. To shorten synthesis time, the one-step synthesis route from the primary seeds is employed.

It is inevitable that thicker seed crystals will co-exist at the center of nanosheets since synthesis requires seed crystals. However, a viable thin nanosheet portion within a nanosheet particle is larger than nanosheets produced through the top-down method.

To determine how to optimize the quality of nanosheets in terms of 1) few remaining ungrown seeds, 2) few intergrown particles, and 3) a high portion of thin nanosheet area within an entire particle, parametric studies that investigated the effects on nanosheets of several variables are conducted: variation in the silica molar ratio of seeds to dC5 precursor sol; pH; the size of the cation of the base; temperature; crystallization time; seed crystal size, and seed crystal morphology. When the silica molar ratio of seeds to the dC5 precursor sol is low, ungrown seed crystals co-exist with- nanosheets. In contrast, when the silica molar ratio of seeds to the dC5 precursor sol is too high, amorphous silica precursor particles remain. When the pH is too low, zeolite crystal is not acquired. On the other hand, pH higher than a critical value results in MFI nanosheets. To avoid highly basic condition, the minimum pH to acquire MFI nanosheets is chosen for the optimal condition. Different cations of base are also investigated, and potassium is the best means of reducing seed thickening at the center. As temperature increases, nanosheet size increases but seed thickening increases simultaneously.

Under assumption that smaller seed crystals lead to smaller seeds embedded at the center of nanosheets and to reduced seed thickening, and so smaller seed crystals are exploited

for nanosheet synthesis. When seeds smaller than 100 nm are used, there is no improvement in seed thickening or the size of embedded seeds at the center of nanosheets. To determine the effect of the size of primitive seed crystals, larger seed crystals are used for nanosheet synthesis. The use of large seed crystals led to significant seed thickening at the center of the nanosheets. To investigate how seed crystal morphology affects nanosheet synthesis SPP, which consists of 2 nm thick intergrown nanosheets with a house-of-card structure, is used as seeds. The resulting nanosheets seem to resemble nanosheets synthesized from primary seeds and do not display a SPP-like, intergrown morphology. This finding suggests that seed crystal morphology has little effect on nanosheet synthesis.

For the purposes of comparison, non-seeded growth from the dC5 precursor sol is carried out. The produced crystal has an intergrown structure like that described in the literature. This result suggests that seed crystals play a critical role in nanosheet synthesis since they control nucleation.

When heteroatoms such as aluminum and tin are inserted into the MFI framework, the crystallization rate becomes slower than that of pure silica nanosheets, although the morphology of the two is similar. Note that the results heteroatom insertion described in this chapter occurred during pilot experiments, and thus, the synthesis condition is not yet optimized. However, the parametric studies on pure silica MFI nanosheets suggest that optimal conditions for aluminum and tin incorporation into MFI framework should be achievable. Furthermore, because heteroatoms produce a catalytic activity in zeolites, the

insertion of aluminum and tin into MFI nanosheets can be investigated for catalytic applications. This topic, however, is beyond scope of this dissertation.

The sequential evolution of primary seeds observed over time suggests that primary seed growth occurs before nanosheet growth. At the initial stage of the growth, the primary seeds grow to the critical size of ~100 nm, at which point the crystals have well-defined facets and a core-shell structure. The core consists of primitive seeds and the shell is composed of crystals grown from the dC5 precursor sol. At the next evolutionary phase—the onset of nanosheet growth—a branch emerged out of a facet of the grown seed and seed growth was stopped. At the late evolutionary phase, the nanosheet gradually grew around the grown seed in a circular motion and assumed a uniform thickness. At the moment that nanosheet growth around the seed was completed, the nanosheets were continuously exposed to the dC5 precursor sol, where abundant nutrients for crystallization were still present. This led, first, to secondary nucleation on the surface of the nanosheets and, second, to crystal growth. As part of the process of secondary nucleation and crystal growth, seed thickening at the center of the nanosheets was accompanied by island formation that resulted in thickness variations in the nanosheets. Although the study revealed the time-resolved sequence of the evolution of primary seeds, it is not clear why the nanosheet emerged out of a facet of the grown seeds. This is a topic for future research.

A massive number of MFI nanosheets can be simply produced from a batch of bottom-up synthesis in a manner that does not require complicated post-synthesis purification. This approach is promising to industrial applications. Moreover, by avoiding the breakage of

crystals due to mechanical forces during exfoliation—a characteristic result of the top-down approach—the well-defined facets of the nanosheet crystals are preserved. In the future it would be useful to investigate the influence of surface structures on adsorption properties. The crystallographic axes of the nanosheets are well-defined, and thus it would be useful to the explore growth rates of crystals along these axes during secondary growth.

Chapter 3: Preparation of high performance membranes from MFI nanosheets

3.1 Introduction

Thin zeolite membranes are of interest since they can be used in separation technologies that are less energy-intensive than currently-used energy-intensive technologies such as distillation, crystallization and pressure-swing adsorption.[38-45] Over the last two decades, researchers have examined alternative methods of organic vapor separation, including xylene isomers,[50,51,53-55,57,78-80] gas separation like butane isomers,[55,78,81,82] and alcohol separation.[7,78,83,84] These methods employ zeolite membranes since they reduce the energy cost of purification.

P-xylene is a raw material used in the production of terephthalic acid, which in turn is a monomer of poly(ethylene terephthalate) (PET) used in the manufacture of water bottles and clothes. According to an analysis in "Global Paraxylene Market by Application", the global market for *p*-xylene is expected to reach 67 million dollars by 2022.[85] In most cases, *p*-xylene is produced in the presence of its isomer, *o*-xylene, which imposes the imperative separation process.[86] The current separation technology for *p*-xylene is distillation, which is an energy-intensive process due to the close boiling points of *p*-xylene (138 °C) and *o*-xylene (144 °C). As an alternative, MFI zeolite membranes can purify *p*-xylene owing to the size/shape discrimination ability of the zeolite framework. A smaller molecule, *p*-xylene (5.8 Å), can diffuse into the micropore channels of the MFI framework while a bigger molecule, *o*-xylene (6.8 Å), cannot. As a result, *p*-xylene enriched permeate can be collected on the permeate side of MFI membranes.

N-butane is a feedstock for the production of ethylene and butadiene and a fuel in the form of the liquefied petroleum gas (LPG). In contrast, *i*-butane is exploited as a blending agent in gasoline. According to a report by "Transparency Market Research", the global market for butanes is expected to reach 282 billion dollars by 2018.[87] The current purification technology for butane isomers is energy-intensive distillation. That less energy-intensive separations of butane isomers can be achieved through using zeolite membranes has been extensively demonstrated.[46,55,78,88-90] *N*-butane generally can pass through the micropores of the MFI zeolite membranes due to its linear configuration. In contrast, the branched molecule, *i*-butane, cannot.

The microstructure of membranes critically affects membrane performance, and many researchers have sought to understand how the orientation of zeolite membranes might be controlled.[52,58,79,91] While in-situ growth of zeolite membranes (wherein bare porous supports are dipped into zeolite precursor sol in order to lead the nucleation and crystallization of zeolites onto the porous supports) cannot easily manipulate the orientation of the zeolite membranes, secondary growth (wherein zeolite-seeded porous supports are dipped into zeolite precursor sol) can be used to tune the orientation of the zeolite membranes.[52,79,91]

Recently Yoon's group has developed a gel-free secondary growth method to attain *b*-oriented MFI membranes.[51,55] They were inspired by earlier work wherein MFI crystals grew on TPA-impregnated silicon wafers by consuming the substrate as silica sources.[92] In the gel-free secondary growth method, the zeolite seeded supports are not dipped into the zeolite precursor sol during secondary growth. Thus, this method is more

environmentally-friendly, economically efficient, and appropriate for industrial applications than conventional secondary growth.

This chapter describes preparation of the MFI membranes of the MFI nanosheets that, as noted in Chapter 2, were synthesized using the bottom-up strategy. The membranes were grown through conventional sol growth and gel-free secondary growth. Subsequently, xylene and butane isomer permeation tests are carried out.

3.2 Experimental

Preparation of the MFI nanosheet coating sol

2 mL of the nanosheet suspension from the two-step growth was transferred into a centrifuge tube and then centrifuged at 1,700 RCF for 30 s. After centrifugation, relatively big intergrown particles settled down to form a cake. The top 1 mL of the supernatant, where relatively light nanosheets were suspended, was collected and then diluted with 1 mL of DI water. Three times the diluted supernatant was centrifuged at 14,500 RCF for 1 min. The resulting nanosheets were dispersed in 45 mL of DI water and then the mixture was used as a coating sol (hereafter called the “coating sol A”).

2 mL of the nanosheet suspension grown from two-step was transferred into a centrifuge tube and centrifuged at 10,000 RCF for 30 s. After centrifugation, relatively large intergrown particles were collected at the bottom of the centrifuge tube in the form of a cake. The top 1 mL of the supernatant was pipetted out for further purification. 1 mL of DI water was added to the supernatant and three times it was centrifuged at 14,500 RCF for 1 min. The purified nanosheets were suspended with 45 mL of DI water and then

exploited as a coating sol (hereafter called “coating sol B”).

1 mL of the nanosheet suspension grown from one-step was transferred into a centrifuge tube and diluted with 1 mL of DI water, then it was centrifuged at 10,000 RCF for 30 s. After centrifugation, relatively large nanosheet particles settled to the bottom to form a cake. The top 0.75 mL of the supernatant was removed for the further purification. 1.25 mL of DI water was added to the aliquot, which was then centrifuged three times for 1 min at 14,500 RCF. The purified nanosheets were suspended with 45 mL of DI water and then employed as a coating sol (hereafter “coating sol C”).

Secondary growth based on zeolite precursor sol

Prior to membrane fabrication, porous α-Al_2O_3 supports were prepared using the slip casting method developed by the Tsapatsis’ group.[54] 1 g of the nanosheet coating sol A was deposited on the prepared porous α-Al_2O_3 supports twice through vacuum filtration. Following the first coating and prior to the second, the nanosheet-seeded α-Al_2O_3 supports were placed in a tubular furnace and calcined at 400 °C for 6 h at a ramp/cooling rate of 1 °C/min under a dry air flow of 100 mL/min.

The calcined nanosheet layers on the α-Al_2O_3 supports underwent secondary growth in the presence of sol, which contains SDA, hydrolyzed TEOS, and water. This was done to close unselective gaps between the nanosheets in the coating layer so that the MFI films would become continuous.

1.52 g of TPAOH (tetrapropyl ammonium hydroxide, 1.0 M, Sigma-Aldrich) was added to 23.09 g of DI water and stirred. To hydrolyze the TEOS, 2.08 g of TEOS (tetraethyl orthosilicate, 98 %, Sigma-Aldrich) was added to the mixture of TPAOH and DI water

and stirred overnight at the room temperature. The hydrolyzed TPA sol was pre-heated in a Teflon-lined stainless-steel autoclave at 150 °C for 1 h, cooled down, and filtered by a syringe filter (GHP, 0.2 μm). The filtered precursor sol was transferred to a Teflon-lined stainless-steel autoclave. The resulting composition of the TPA precursor sol was $60SiO_2$: 9TPAOH: $8100H_2O$: 240EOH. The MFI nanosheet seeded α-Al_2O_3 supports were dipped into the TPA precursor sol and hydrothermally treated at 100 °C for different hydrothermal treatment times (7 h, 12 h, and 24 h) in order to obtain defect-free continuous MFI films. The grown films were washed with DI water overnight and then dried at 70 °C overnight. To remove the SDA, TPA, from the zeolite framework the films were then calcined in a tubular furnace at 400 °C for 6 h at a ramp/cooling rate of 1°C/min under a dry air flow of 100 mL/min.

1.1 g of TEAOH (tetraethyl ammonium hydroxide, 20 wt %, Sigma-Aldrich) was added to 23.2 g of DI water and stirred. Then 2.08 g of TEOS was added. To hydrolyze the TEOS the mixture was stirred overnight at room temperature. The resulting composition of TEA sol was $60SiO_2$: 9TEAOH: $8100H_2O$: 240EOH. The non-pre-heated TEA precursor sol was directly transferred to a Teflon-lined stainless-steel autoclave. The MFI nanosheet seeded α-Al_2O_3 supports were dipped into the TEA sol and heated at 180 °C for different hydrothermal treatment times (6 h, 12 h, 18 h, and 24 h). The resulting membranes were washed with DI water overnight and then dried at 70 °C overnight. The dried membranes were calcined in a tubular furnace at 400 °C for 6 h at a ramp/cooling rate of 1 °C/min under a dry air flow of 100 mL/min.

Gel-free secondary growth

To carry out the gel-free secondary growth, porous silica supports were prepared using the recipe recently developed by the Tsapatsis' group[55]. The recipe involves pressing silica fiber powder and then sintering it[55]. The sintered silica supports were polished to reduce the roughness of the surface. 500 nm Stöber silica particles prepared by the well-established Stöber method[55] were deposited by manual rubbing on the polished surface of the silica supports, which further smoothened the support surface. On top of the 500 nm silica particle layer, 50 nm Stöber silica particles synthesized through the Stöber method [55] were rubbed so that they could serve as silica sources during secondary growth. In this way, two intermediate layers of 500 nm and 50 nm Stöber silica particles were deposited onto the porous silica supports in sequence. In the case of the nanosheets synthesized from the two-step growth (i.e., coating sol A and B), 1 g of the coating sol was twice deposited by vacuum filtration, and in between the deposited layers it was calcined in a tubular furnace at 400 °C for 6 h at a ramp/cooling rate of 1 °C/min under a dry air flow of 100 mL/min. 0.5 g of coating sol C, which was prepared from nanosheets synthesized during one-step growth, was deposited by vacuum filtration for four times, and in between the coating layer it was calcined in a tubular furnace at 400 °C for 6 h at a ramp/cooling rate of 1 °C/min under a dry air flow of 100 mL/min.

Following calcination, the MFI nanosheet deposited silica supports were soaked in a SDA solution that contained 0.075 M TPABr (tetrapropyl ammonium bromide, 98 %, Sigma-Aldrich) and 0.075 M KOH (potassium hydroxide, 85 %, Sigma-Aldrich). The excess TPABr/KOH solution was wiped up with kimwipes. After being transferred into

Teflon-lined stainless-steel autoclaves, the supports underwent thermal treatment at 190 °C for 24 h in order to acquire defect-free continuous films. This secondary growth is called “gel-free growth” since it occurs in the absence of gel or sol.

The grown films were soaked in DI water overnight to remove KOH, and then they were dried overnight at 70 °C. The dried films were calcined at 400 °C for 6 h at a ramp/cooling rate of 1 °C/min under a dry air flow of 100 mL/min in a tubular furnace.

Permeation test of membranes

The membrane was loaded in a stainless-steel membrane module and connected to the permeation test set-up. The module was placed in an oven to control temperature during the measurement. The membrane performance was tested in the Wicke–Kallenbach mode, under which concentration gradients are driving forces of permeation with feed and permeate in-flows of carrier gases.[38,55,57] During the xylene isomer permeation test, equimolar p-xylene/o-xylene vapor feed flow in a carrier gas, helium, was applied to the membrane surface. The helium flowed as a sweep gas that collected permeate. Next the permeate was mixed with methane, an internal standard, and then, in order to analyze composition, it was injected into a gas chromatography (GC, Agilent, 7890B) that was equipped with a flame ionization detector (FID). Feed composition was also analyzed by GC to evaluate permeance and the separation factor. The temperature during the permeation test ranged from 50 °C to 200 °C.

The separation factor (S.F.) was evaluated as follows:

$$\text{S. F.} = \frac{x_{p,P-X} / x_{p,O-X}}{x_{f,P-X} / x_{f,O-X}}$$

where $x_{f,i}$ and $x_{p,i}$ are mole fractions of the component *i* (*P-X*: *p*-xylene and *O-X*: *o*-xylene) in the feed and permeate, respectively.

When the membrane exhibited high separation performance for xylene isomers, it was tested for butane isomer separation. To remove the residue of the xylenes that had been adsorbed onto the zeolite framework during the xylene vapor permeation test, helium was flowed overnight as a sweep gas on both the feed and the permeate side at 180 °C (hereafter called the "purging process"). After purging, the flows of helium on the feed and the permeate side were stopped simultaneously and the membrane was cooled to room temperature. As part of the butane isomer permeation test, equimolar *n*-butane/*i*-butane stream was fed to the membrane on its feed side. Helium flowed as a sweep gas to collect permeate, and the permeate was then mixed with an internal standard, methane, and this was injected into a gas chromatography (GC, Agilent, 7890B) equipped with a thermal conductivity detector (TCD) to determine composition. Feed composition was also determined by GC to evaluate permeance and the separation factor. The permeation test was conducted at temperatures that ranged from room temperature to 120 °C.

The separation factor (S.F.) was evaluated as follows:

$$\text{S. F.} = \frac{x_{p,n-C4} / x_{p,i-C4}}{x_{f,n-C4} / x_{f,i-C4}}$$

where $x_{f,i}$ and $x_{p,i}$ are mole fractions of the component *i* (*n-C4*: *n*-butane and *i-C4*: *i*-butane) in the feed and the permeate, respectively.

Characterization

The morphology of the coating and the membrane was analyzed with an SEM. The

orientation of the nanosheet layer deposited on the porous support and the membranes was analyzed using XRD.

3.3 Results and discussion

TPA sol growth

The purified nanosheet coating sol A was deposited on porous α-Al_2O_3 disks via vacuum assisted filtration. As shown in **Figure 3-1A**, the zeolite nanosheet layers wholly covered surfaces of porous α-Al_2O_3 disks. However, the films could not be employed as selective membranes since unselective gaps were present between the zeolite nanosheet particles. To eliminate the gaps, a secondary growth of the films with TPA sol was carried out. After secondary growth (heated at 100 °C for 7 h) the film, exhibited nanosheet-shaped grain boundaries, which indicate that there was little intergrowth of zeolite nanosheets (**Figure 3-1B**). The partially grown membrane was tested for xylene isomer permeation. As expected, the membrane exhibited a separation factor of 1, which indicates that no separation took place. This suggests that 7 h secondary growth is not long enough for a continous MFI film to develop, and as a consequence, interparticlular non-selective gaps remain. To close the non-selective gaps between the MFI nanosheet particles in the deposited layer, the secondary growth period was prolonged. After hydrothermal treatment for 12 h, the intergrowth of the zeolite nanosheets was more developed (**Figure 3-1C**). However, the membrane did not show any separation factor of *p*-xylene over *o*-xylene. Perhaps this stems from that the MFI nanosheets lying on the top surface of the

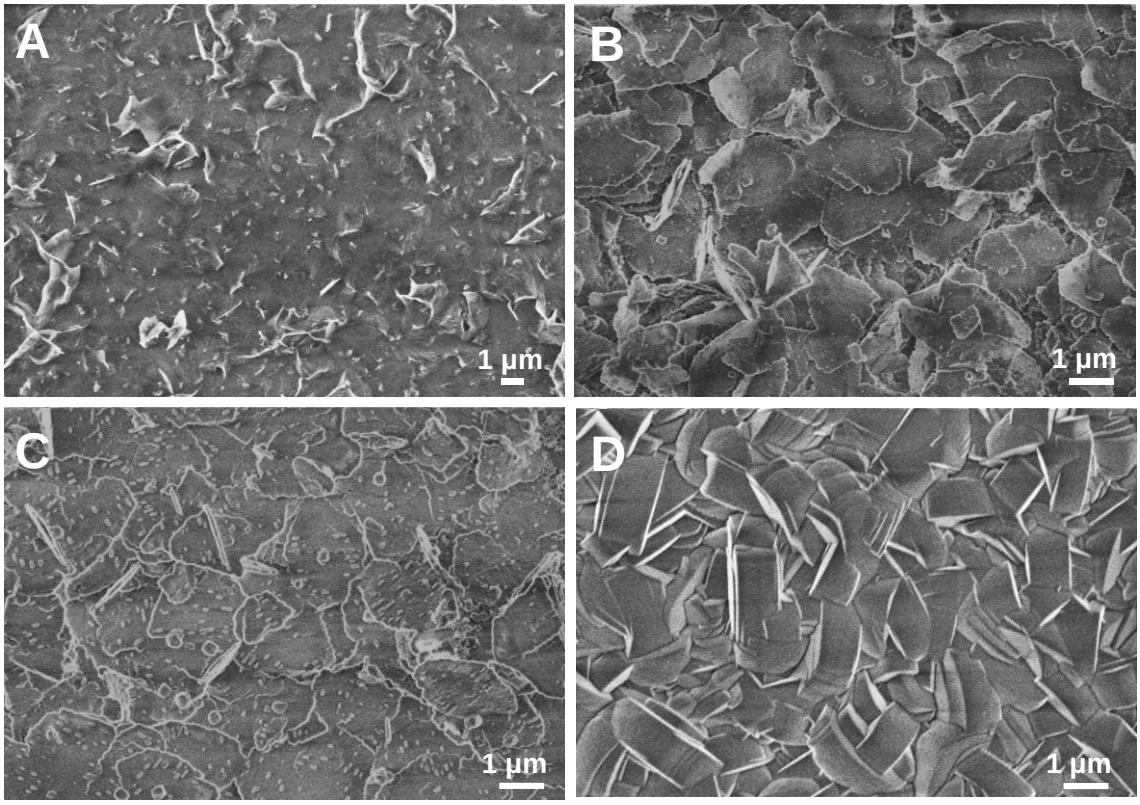

Figure 3-1. SEM images of nanosheet deposition from the coating sol A **on a porous α-Al_2O_3 support (A) and after secondary growth from the TPA sol at 100 °C for 7 h (B), 12 h (C), and 24 h (D)**.

porous α-Al_2O_3 support did not develop sufficiently. Unlike the top surface of the coating, which is directly exposed to the TPA sol, the bottom part of the coating (lying on the top surface of the porous α-Al_2O_3 support) is not directly exposed to the TPA sol, which is where the nutrients that facilitate growth are present.

Not surprisingly, the growth rate of the top surface appears to be higher than that of the bottom part. This asymmetric structure might cause poor separation performance in the the membrane. Hoping to provide enough time for the bottom portion of the seeded layer to grow, the secondary growth period was lengthened to 24 h (**Figure 3-1D**), but the orientation of the film was lost and the result was a randomly orientied film. Perhaps this

results is associated with the growth of MFI crystals from nuclei present in the TPA sol. These randomly oriented crystals were precipitated onto the top surface of the MFI nanosheet layer, and this may have led to the random orientation of the surface of the MFI film. The calcined film was tested for xylene isomer permeation, but no separation factor was attained. The longer secondary growth resulted in an overgrowth of randomly oriented zeolite crystals, and this may have led to the formation of invisible internal cracks. These cracks, caused by aniostropic strains generated upon calciantion, reduce separation performance of the membrane.[93]

TEA sol growth

Addressing the problem of the random orientation of zeolite nanosheet films that can occur during secondary growth, Yoon's group demonstrated that secondary growth from a sol/gel of TEA can preserve the orientation of seed layers.[50] Inspired by this study, TPA was replaced with TEA and secondary growth from TEA sol at 180 °C was carried out for various periods of time. The film grown for 6 h underwent partial intergrowth (**Figure 3-2A**) in a manner that recalls film grown from TPA sol at 100 °C for 7 h. The xylene permeation performance of the activated film grown from TEA sol at 180 °C for 6 h was poor. It suggests that 6 h of growth is not enough to allow the non-selective gaps to close. In an attempt to increase the intergrowth of the film, secondary growth was prolonged to 12, 18, and then 24 h. When the period of secondary growth was increased from 6 h to 12 h, intergrowth was improved (**Figure 3-2B**). The xylene permeation test, undertaken after activation, did not exhibit any separation factor. The low separation factor indicates that

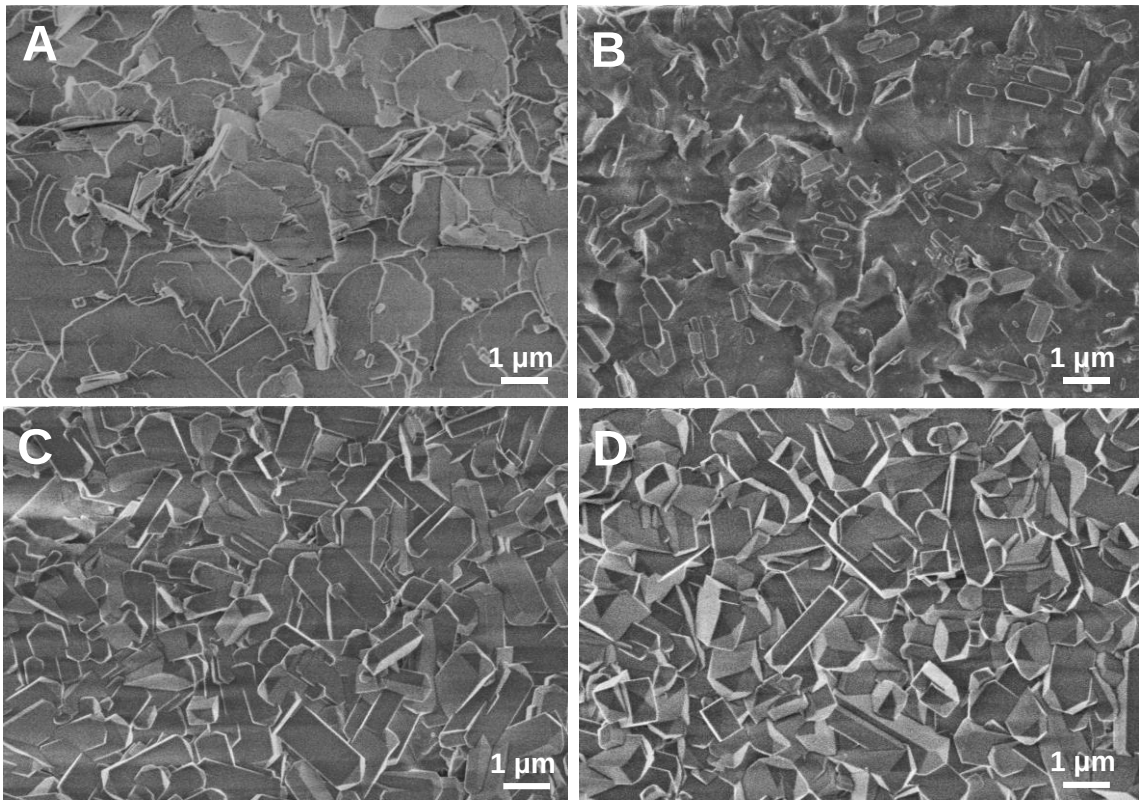

Figure 3-2. SEM images of nanosheet films from coating sol A **on porous α-Al_2O_3 supports after secondary growth from TEA sol at 180 °C for 6 h (A), 12 h (B), 18 h (C) and 24 h (D)**.

non-selective gaps exist in the film even after the longer secondary growth is conducted. In an attempt to obtain a defect-free continous film consisting of MFI nanosheets, then secondary growth at 180 °C was extended to18 h and 24 h. The randomly oriented MFI crystals deposited on the films for 18 h and 24 h are illustrated in **Figure 3-2C** and **D**, resepectively.Neither led to high xylene isomer permselectivity. When TEA was exploited as an SDA for secondary growth, the films resembled those grown from TPA. That is, the non-selective inter-particle gaps did not close during short hydrothermal treatment. After long hydrothermal treatment, randomly oriented MFI crystals

precipitated on the top of the seed layer.

Gel-free secondary growth

To preserve the initial *b*-orientation of the seed layers (i.e., the MFI zeolite nanosheet films on the porous supports), Yoon's group experimented with gel-free secondary growth using TPAOH as SDA.[51] Their research was inspired by earlier work[92] that indicated that when the substrate is a silica source, supported zeolite crystals can be grown in the absence of a liquid sol or gel. Yoon's group demonstrated that *b*-oriented MFI membranes fabricated during gel-free secondary growth significantly enhanced xylene isomer permselective performance.[51,55] However, the gel-free secondary growth is not valid when different supports are used. In particular, the silica supports should have 50 nm silica layer on the top surfaces in order to provide silica sources for growth. During the gel-free secondary growth, the 50 nm silica layer serves as a silica source for growth leading to continuous zeolite films. Before beginning gel-free secondary growth, the porous silica fiber supports were prepared using the robust recipe developed by Tsapatsis' group.[55] The bare silica fiber supports have a high roughness (**Figure 3-3A**) and pore size is so large that zeolite nanosheets cannot stay on top of surface of the support. To smooth the surface and reduce the size of its pores, 500 nm Stöber silica particles were deposited by manual rubbing with gloved hands on the surface of the support, then it was sintered (**Figure 3-3B**). On top of the 500 nm Stöber silica particle layer, 50 nm Stöber silica particles were manually rubbed and then sintered to provide silica sources for gel-free secondary growth (**Figure 3-3C**) To prevent cracks formation

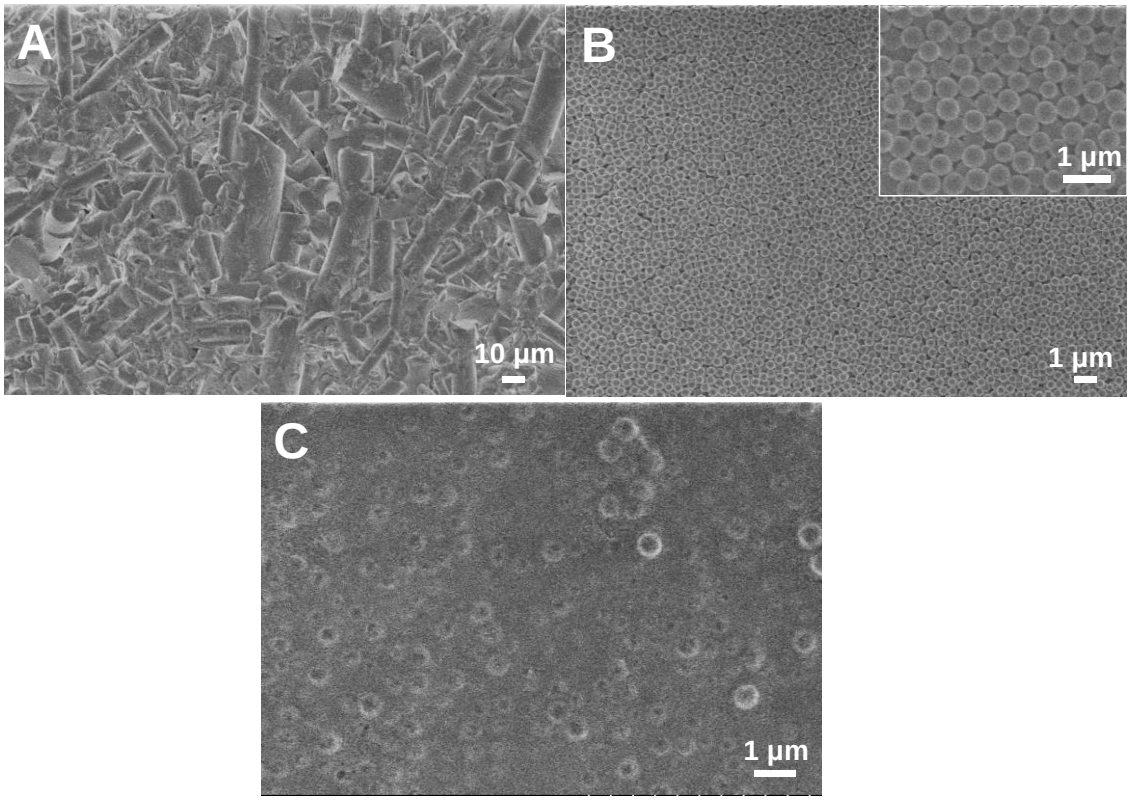

Figure 3-3. SEM images of the bare surface of porous silica supports (A), the 500 nm Stöber silica layer on the porous silica supports (B), and the deposited 50 nm Stöber silica layer on top of the 500 nm Stöber silica layer (C). The inset of B is a magnified SEM image of B.

during sintering, the deposited layer of 50 nm Stöber silica was so thin that the 500 nm Stöber silica particles under it were visible (**Figure 3-3C**).

A vacuum assisted coating method was applied to depositing coating sol A onto the smoothened porous silica supports. The coating covered the entirety of the porous silica supports (**Figure 3-4A**). However, when the gel-free secondary growth was completed, the grown film had a high roughness (**Figure 3-4B**), which led to low xylene isomer permselectivity. Perhaps the roughness stems from twinning or from the large particles in

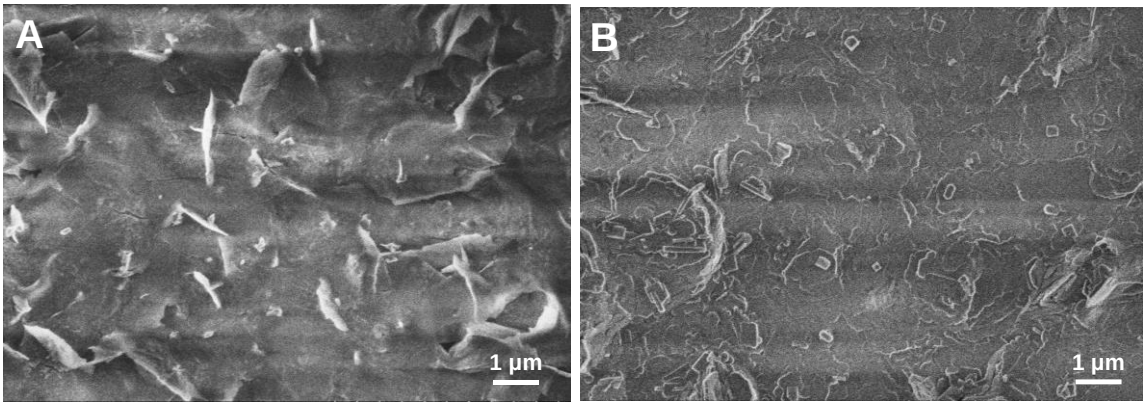

Figure 3-4. SEM images of a nanosheet film produced by coating sol A **on the smoothened porous silica supports (A) and the film after gel-free secondary growth (B).**

the coating sol A leading hindered deposition of the nanosheets. To improve the coating quality, intergrown particles should be eliminated in the coating sol. To achieve it, centrifugation of as-synthesized nanosheet suspension at higher RCF was carried out. This leads heavier intergrown nanosheets to settling down at the bottom in a cake form. As a result, supernatant is composed of less intergrown particles, light nanosheets. By this method, coating sol B was prepared.

The layer deposited from sol B coating appeared to be more uniform (**Figure 3-5A**) than the layer produced from sol A coating. Gel-free secondary growth produced continuous nanosheet films (**Figure 3-5B**) and calcination activated the films for the permeation test. **Figure 3-5C** presents XRD patterns that reveal the orientation of the seed layer before gel-free secondary growth and of the membrane that was generated through gel-free secondary growth. The seed layer has a dominantly *b*-out-of-plane orientation indicated by the dominant (020) reflection peak in the XRD pattern (**Figure 3-5C**). After the gel-free secondary growth, the orientation of the nanosheet seed layer remained intact

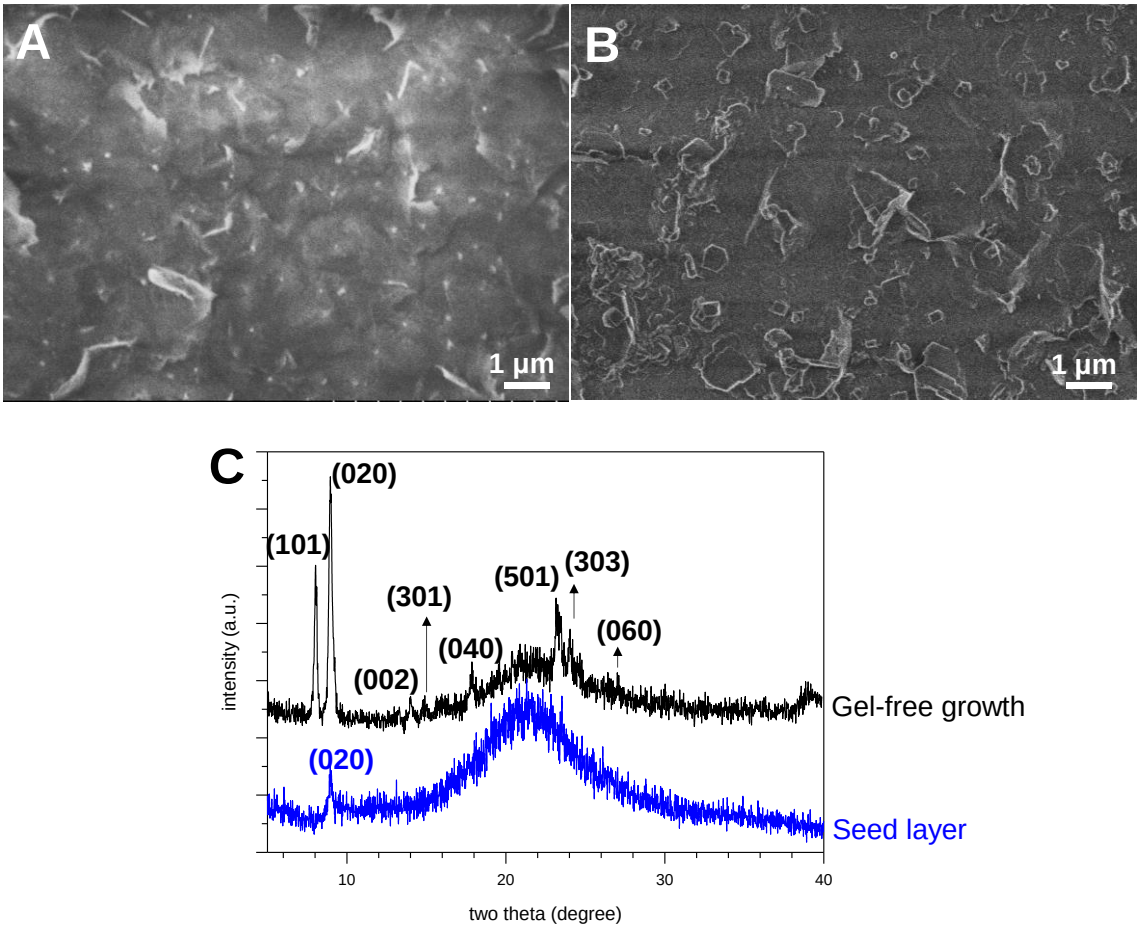

Figure 3-5. SEM images of: nanosheet films made by coating sol B on the smoothened porous silica support (A); and the film after gel-free secondary growth (B). C shows the XRD patterns of the nanosheet film before (seed layer) and after gel-free secondary growth.

(**Figure 3-5C**). However, (*h0l*) reflections, associated with *c*-orientation, were pronounced simultaneously in the membrane compared to the seed layer which does not reveal the *(h0l)* reflections. This may stem from the fact that seed crystals that do not have the *b*-out-of-plane orientation are embedded at the center of the nanosheets. Moreover, perhaps it can be attributed to the co-existence in the seed layer of twinning nanosheets. Indeed, the crystal growth rate of MFI along the *c*-direction is higher than in the *a*- and *b*-directions.[74] Therefore, the (*h0l*) reflections of XRD, which are related to the

c-orientation, become significant.

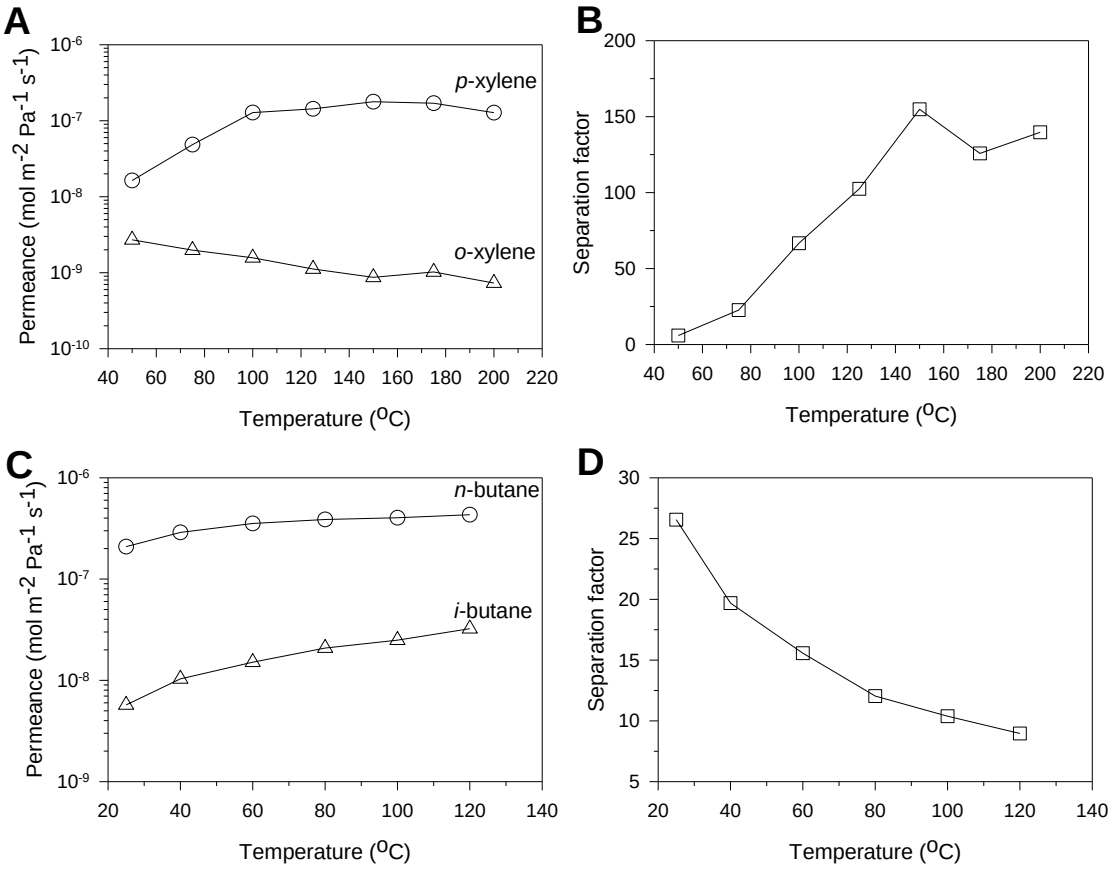

Figure 3-6. The permselectivity of membranes fabricated from the gel-free secondary growth of nanosheet seed layer of coating sol B. The permeances of *p*-xylene and *o*-xylene (A) plus separation factors of *p*-xylene over *o*-xylene (B). The permeances of *n*-butane and *i*-butane (C) as well as separation factors of *n*-butane over *i*-butane (D).

The gel-free grown film was activated through calcination for xylene isomer permeation test. As a result, a high permeance of *p*-xylene (1.8×10^{-7} mol m^{-2} Pa^{-1} s^{-1}) was obtained. It is comparable to the state-of-the-art, where membranes fabricated through gel-free growth of exfoliated MFI nanosheets.[55] Additionally, a high separation factor—above 100—of *p*-xylene over *o*-xylene was achieved (**Figure 3-6B**). Perhaps this highly *p*-

xylene permselective property was attained because of the dominant *b*-orientation of the membrane—an orientation that provides a low transport resistance since its straight micropore channels run along the *b*-axis.

A butane isomer permeation was also carried out after the membrane was purged with helium streams to eliminate the xylene that had been adsorbed onto the MFI micropore channels. As **Figure 3-6C** indicates, the lowest permeance of *n*-butane is 2.1×10^{-7} mol m^{-2} Pa^{-1} s^{-1} at room temperature. This is comparable to the counterpart of the membranes prepared by gel-free secondary growth from nanosheets that were synthesized using the top-down strategy.[55] The permeance of *n*-butane is higher than the values reported in the literature based on conventional secondary growth (wherein the zeolite seeded supports are dipped into zeolite precursor sol or gel).[46,52,78,88-90] The separation factors (**Figure 3-6D)** are lower than those of membranes prepared by gel-free secondary growth fabricated from nanosheets based on the top-down method[55]. The fact that seed particles are embedded at the central part of the nanosheets, which could hinder the close packing of nanosheets, might account for the low separation factors. In other words, thickness variations in the nanosheet and the seed portion might lead to loose packing of the nanosheets, and loose packing might lead to inter-particle gaps that do not close during secondary growth.

To shorten membrane preparation time, coating sol C consisting of one-step grown nanosheets, was deposited onto the smoothened porous silica supports, and this facilitated gel-free secondary growth. **Figure 3-7A** shows improvement in uniformity and a more

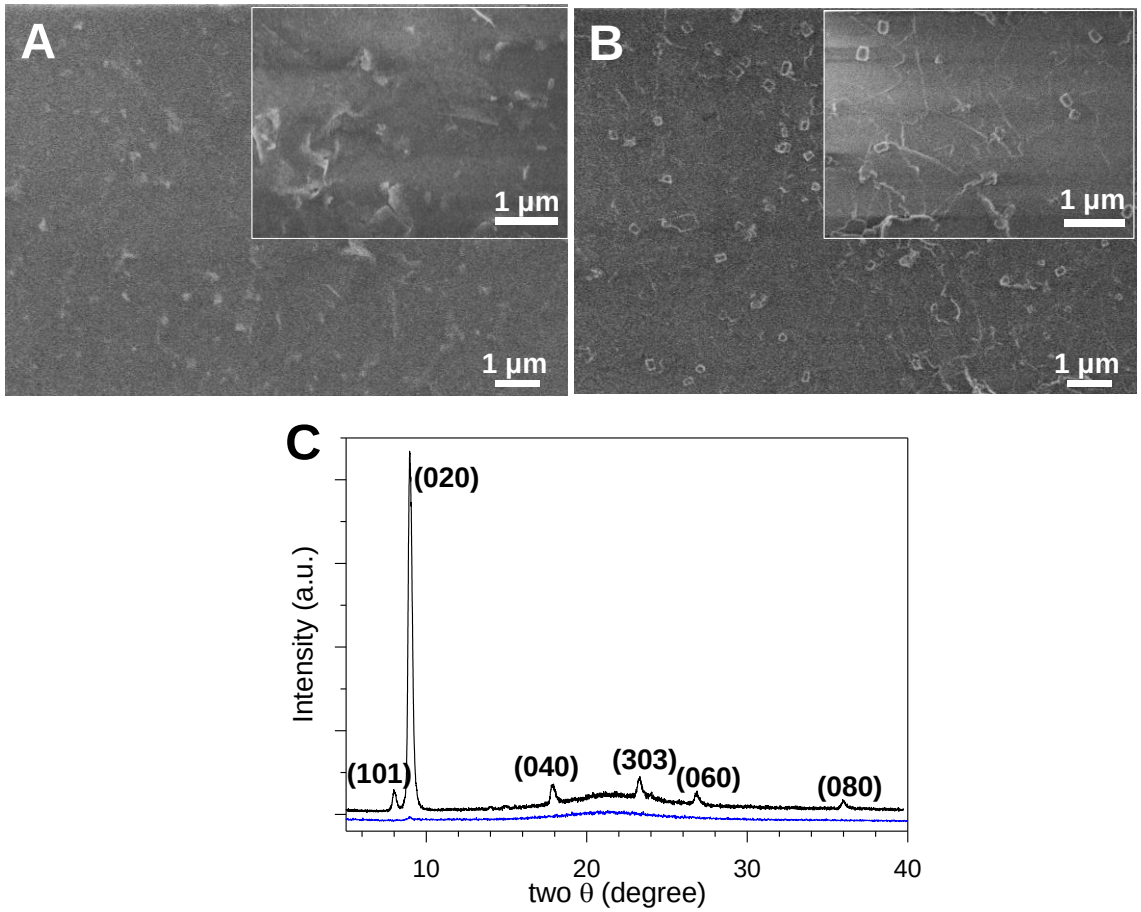

Figure 3-7. SEM images of a nanosheet film made by coating sol C on the smoothened porous silica support (A) and the film following gel-free secondary growth (B). XRD patterns of the nanosheet film before (seed layer, blue line) and after gel-free secondary growth (black line) (C).

continuous deposition of nanosheet layers on the smoothened porous silica supports than is obtained from coating with sol B (**Figure 3-5A**).

Compared to coating with sol B, coating with sol C significantly reduces the development of twinning nanosheets in the deposited layer. Following gel-free secondary growth, the resulting film exhibited well-intergrown *b*-oriented films (**Figure 3-7B**). The orientation of the film was confirmed by a XRD pattern (**Figure 3-7C**): it exhibits a mainly *b*-out-of-plane. However, (*h0l*) reflections co-existed with (*0k0*) reflections. The *(h0l)* reflections

have two possible sources; growth of seed particles embedded at the center of nanosheets and growth of intergrown nanosheets. The *(h0l)* reflections are more likely to stem from growth of seed crystals embedded at the center of nanosheets since most of intergrown particles were not frequently observed in the coating layer (**Figure 3-7A**). Moreover, the reduced intensities of (h0l) reflections compared to membranes from coating sol B support that the (h0l) reflections in membrane from coating sol C is more likely from growth of seed crystals embedded at the center of nanosheets.

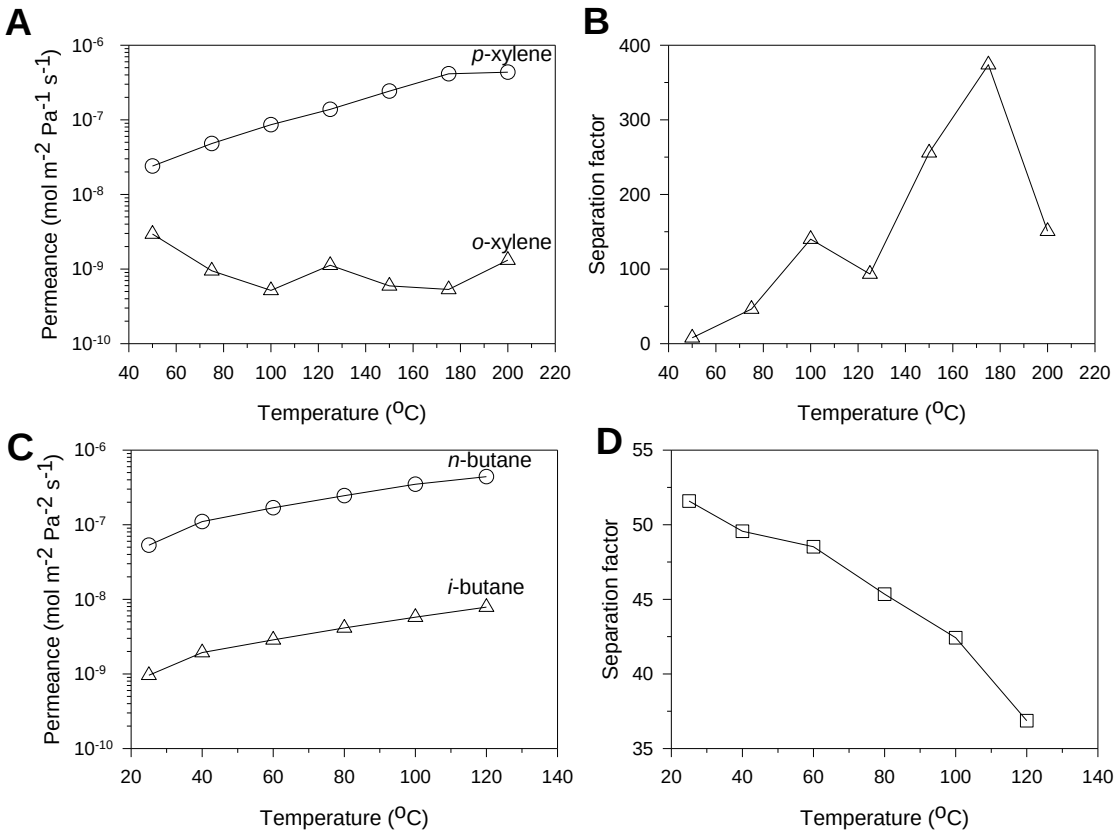

Figure 3-8. The permselectivity of membranes fabricated from the gel-free secondary growth of a nanosheet seed layer made by coating sol C. The permeances of *p*-xylene and *o*-xylene (A) and the separation factors of *p*-xylene over *o*-xylene (B). The permeances of *n*-butane and *i*-butane (C) and the separation factors of *n*-butane over *i*-butane (D).

The grown films were calcined for the xylene isomer and the butane isomer permeation test. In the case of xylene isomer permeation (**Figure 3-8A**), the *p*-xylene permeances were as high as those of membranes fabricated by coating sol B and membranes prepared from nanosheets synthesized under the top-down strategy[55]. The separation factor reached approximately 400 (**Figure 3-8B**), which is as high as values reported for membranes prepared via gel-free secondary growth of the nanosheet films that were fabricated using the top-down method[55]. When the butane isomer permeation test was conducted at room temperature, as shown **in Figure 3-8C**, the permeance of *n*-butane was lower than it is in membranes prepared with coating sol B, but over the measured temperature range separation factors in the former were superior to those in the latter (**Figure 3-8D**). This may be associated with the membrane from coating sol C is more preferentially *b*-oriented than from coating sol B. Additionally, the seed layer deposited from coating sol C (**Figure 3-7A**) appears to be more uniform and flatter than the seed layer prepared from coating B (**Figure 3-5A**). This may indicate that in the coating layer from coating sol C the nanosheets are closely packed. Perhaps as the area of the nanosheet that are closed packing grows, the degree of intergrowth of the films increases. Thus, it is possible that membrane performance could be controlled by manipulating the quality of the seed layer.

3.4 Conclusion

Membranes prepared via sol growth (in the presence of TPA and TEA as SDAs) from films deposited on porous α-Al_2O_3 supports are not permselective to *p*-xylene. The

nanosheet layers deposited through vacuum-assisted coating do not appear to be uniform. The deposited films composed of two-step grown nanosheets (coating sol A) show twinning particles, and these hinder the uniform orientation of the deposited nanosheet layer. Perhaps during the calcination step this leads to crack formation, which in turn is caused by anisotropic thermal expansions of the crystallographic axes.[93] In the case of the short hydrothermal treatment, the inter-particle gaps do not close during secondary growth, and this results in non-permselective membranes. In contrast, in the case of the long hydrothermal treatment, randomly oriented zeolite crystals are precipitated onto the seed layers, and this disturbs the pristine orientation of the seed layer. The randomly oriented zeolite crystals that exist on the top of the seed layers perhaps result in cracks that form during calcination in response to the mismatching of internal strains generated in the zeolite framework.[93] Hence, the membranes produced are not permselective to *p*-xylene.

Gel-free secondary growth is introduced in order to preserve the orientation of the seed layers. In attempt to remove twinning particles from the nanosheet coating sol, and thus improve seed layer uniformity, the method of preparing the coating sol was revised. The higher RCF helps large particles, which are twinning nanosheets in the as-synthesized two-step grown nanosheet suspension, to settle after centrifugation into a cake-like form. To prepare the porous silica supports for the gel-free secondary growth the surface of the porous silica supports was smoothened, first, with a 500 nm and, then, with a 50 nm of Stöber silica layer deposition.

The membranes prepared via gel-free secondary growth from new seed layers that have enhanced uniformity (coating sol B) have a dominant *b*-orientation. In the XRD pattern, *c*-orientation related reflection peaks such as (*h0l*) were observed. These may be attributed to the growth of seed particles embedded at the center of the nanosheets and to twinning nanosheet particles. The membranes, which achieve a high permeance of *p*-xylene, might have industrial applications. Furthermore, the high separation factors of p-xylene over o-xylene—above 100—are achieved. The permeances of *p*-xylene of the membranes are as high as those of membranes fabricated from nanosheets as part of the top-down approach. In the case of the butane isomer permeation, the membranes attain high *n*-butane permeances comparable to those of membranes that as part of the top-down strategy are fabricated from nanosheets. Over the entire temperature range of the measurement the separation factors are moderate. In the case of the xylene isomer and butane isomer permeation, the separation factors are comparable to high values of conventional sol-based secondary growth,[46,53,54,78,88-90] but they are lower than values obtained from membranes fabricated from nanosheets under the top-down method.[55] This may indicate that the seeds embedded at the center of nanosheets inhibit the closed packing of nanosheet particles. The thickness of nanosheets and central seeds can vary, and these variations can stop uniform, closely packed films from forming.

To shorten the time of membrane preparation and at the same time enhance the uniformity of the seed layer, one-step grown nanosheets with coating sol C was prepared. When vacuum assisted coating is used to coat sol C onto porous silica supports, twinning nanosheets are reduced and nanosheet films become highly flat and uniform. Continuous

films produced through gel-free secondary growth exhibited highly permselective *p*-xylene and *n*-butane. The membranes have mainly *b*-orientation, and a minor (*h0l*) orientation is revealed in the XRD pattern. The (*h0l*) reflections in the XRD perhaps stem from the growth of seed particles embedded at the center of the nanosheets.

In terms of preparation time and cost, membranes fabricated from bottom-up synthesized nanosheets can be produced most efficiently. As discussed in Chapter 2, the bottom-up synthesized nanosheets have thickness variations in central seed part and the nanosheet part. Thus, the bottom-up synthesized nanosheets are not closely packed in a coating layer leading to lowering separation performance. Although membranes fabricated from bottom-up synthesized nanosheets have slightly lower separation factor than those fabricated from top-down approach, the bottom-up synthesized nanosheet membranes are attractive to industrial applications of the zeolite membranes.

Chapter 4: Preparation of de-templated nanosheets for processes with polymers

4.1 Introduction

SDAs play a critical role in the synthesis of zeolites to template the pore structures of the zeolite framework. For this reason some call SDAs a template. However, to open the micropores of the zeolite framework after synthesis SDAs must be eliminated since they are occluded in pore channels in the zeolite framework. In general, SDAs are organic molecules that tend to decompose at high temperatures, which is when Hoffman degradation occurs.[94,95] Thermal treatment at high temperatures is energy-intensive, and in the presence of moisture, the steaming process that takes place causes zeolites to lose crystallinity.[96] Furthermore, the condensation of hydroxyl groups on the external surfaces of zeolite causes nano-sized zeolites to form aggregates that reduce surface area. For example, upon calcination the layered zeolite nanosheets are condense one another, and hence the layered structure collapsed. To prevent the condensation of nanosheets, Tsapatsis' group[63] developed a pillaring treatment in the interlayer spaces. They swelled the interlayer space of a layered precursor of MCM-22 (i.e., MCM-22 (P)) with a surfactant (CTAB, cetyl trimethyl ammonium bromide) under a basic condition and then introduced a silica source, TEOS, into the swollen interlayer space. The TEOS in the swollen interlayer space was hydrolyzed and subsequently condensed to form silica particles. Upon calcination, the layered structure was preserved with the support of silica particles, which are pillaring materials.

To preserve the layered structure of layered MFI nanosheets Ryoo's group[94] developed

pillaring with silica particles in interlayer space. They diffused TEOS, a silica source, into the interlayer space and then hydrolyzed and subsequently condensed to form silica particles.

The silica particles served as pillars that supported the layered structure during calcination. Although the layered structure can be preserved through pillaring, in practice, single zeolite nanosheets should be exfoliated to fabricate thin zeolite membranes. Moreover, treating silica particles for pillaring is challenging. One approach is to selectively dissolve the silica particles under either basic or acidic conditions. Zeolite layers can be condensed under acidic conditions since the isoelectric point of silica materials is around 2.[95] In contrast, under a basic condition, the crystallinity of the zeolite layers can be easily destroyed since the nanosheet crystal is thin.

In another extreme attempt to preserve nanosheet morphologies, Tsapatsis' group developed a procedure to self-pillared nanosheet structures such as the SPP.[72] After calcination, the parent structure of the SPP did not collapse since its layers were supported. However, in practice it is difficult to delaminate into single nanosheets since structure of the SPP is highly-intergrown. Even under successful exfoliation, the yield would be very low and the lateral size of the individual nanosheets produced would be tiny due to the extensive intergrowth of the SPP—the result is not desirable for membrane applications.

Another designated approach is to prepare SDA-free (de-templated) MFI nanosheets that have no aggregates. Van Bekkum's group reported that 300 °C is the lowest possible temperature for the SDA removal of a single MFI crystal.[96] Under a mild condition of

calcination at 300 °C fewer and less extensive aggregates would form than do under a high temperature of 550 °C. MFI nanosheets are more likely to separate from each other since, unlike layered structures, they are not closely packed to form entirely condensed structures. Upon calcination, the interaction between the MFI nanosheets would be lower than in the layered structure possibly, and this might facilitate easier exfoliation after calcination.

Yan's group prepared a colloidal suspension of SDA-free MFI nano-crystals by calcining MFI nano-crystals in the presence of carbonized polymer networks. This prevented aggregates of the MFI nano-crystals from forming upon calcination.[97] Co-polymerization of the water soluble organic monomers acrylamide and *N*,*N*'-methylenebisacrylamide took place in the colloidal suspension of MFI nano-crystals, which contained SDAs in the zeolite framework. The resulting polymer provided a network barrier between MFI crystals during carbonization and calcination, which prevented MFI crystals from closed-packing. As a result, Yan's group produced a colloidal suspension of SDA-free MFI nano-crystals. This methodology can be used to acquire de-templated MFI nanosheets that have no aggregates.

Another strategy is to chemically decompose the SDA molecules without calcination. This approach is promising because aggregates do not form as a result of thermal treatment. Thermal treatment is not appropriate for processes combining polymers—for example, zeolite/polymer mixed matrix membranes or polymeric supports—that tend to degrade with thermal treatment.

Zeolite membranes have an attractive separation performance, but they are not widely

used in industrial separation processes since their cost efficiency is low compared to that of polymeric membranes.[36,59,98] That said, polymeric membranes are simple and inexpensive to produce, while the permeability and selectivity are lower than zeolite membranes. To obtain the synergic effects of zeolites and polymers, researchers have added highly selective zeolite materials as fillers in polymer matrix to form zeolite/polymer mixed matrix membranes.[99-109] To obtain effective zeolite/polymer mixed matrix membranes, zeolites with pore opening (i.e., de-templated zeolites) should be uniformly dispersed in polymer matrix. This process cannot be achieved through calcination since polymers have a low thermal stability.

Polymeric supports can replace expensive inorganic porous supports. Once zeolites are deposited on the polymeric supports, thermal treatment should be avoided due to the low thermal stability of the polymers. In other words, zeolites should be de-templated prior to being deposited on the polymeric supports. Yan's group demonstrates that zeolite NaA membranes on polymer/zeolite composite hollow fiber supports (PES(polyethersulfone)/zeolite NaA) lead to a high water/ethanol separation factor.[110] Their findings raise the possibility that zeolite membranes can be fabricated on polymeric supports. To achieve this, the de-templation strategy should not include thermal treatment.

Melián-Cabrera's group has developed a chemically assisted de-templation method called *Fenton Chemistry* that has been used in waste water treatment. The *Fenton Chemistry* was applied in the removal of SDAs from zeolite BEA (beta, pore size *ca.* 7 Å) in 2005 by Melián-Cabrera's group.[67] As presented in equation (1), they generated hydroxyl

radicals (·OH) from hydrogen peroxide (H_2O_2) in the presence of Fe^{2+}/Fe^{3+}, which oxidized the SDA molecules into small molecules.

$$Fe^{2+} + H_2O_2 \rightarrow Fe^{3+} + \cdot OH + OH^- \quad (1)$$

$$Fe^{3+} + H_2O_2 \rightarrow Fe^{2+} + \cdot OOH + H^+$$

Their demonstration of the micropore opening of aluminosilicate BEA (using the *Fenton Chemistry*) is supported by argon adsorption/desorption and TGA (Thermogravimetric analysis) analysis. The *Fenton Chemistry* may be applied to MFI nanosheet in order to prepare de-templated MFI nanosheets that do not form aggregates.

In this chapter, various attempts to prepare de-templated MFI nanosheets that are discussed in chapter 2 are illustrated. The objective of attempts to de-templation has been to prevent MFI nanosheets from forming condensation and aggregates.

4.2 Experimental

Calcination of nanosheets under mild conditions

As mentioned in the introduction, 300 °C is the mildest condition to eliminate SDAs from the MFI zeolite framework. To demonstrate the mild calcination of the MFI nanosheets, calcination was carried out at 300 °C for 6 h at a ramp/cooling rate of 1 °C/min under a dry air flow of 100 mL/min in a tubular furnace. The thermally treated MFI nanosheets were analyzed by argon adsorption/desorption isotherm to check the degree of the micropore opening. As a reference, complete elimination of the SDA out of the zeolite framework was carried out by calcination of the MFI nanosheets at 550 °C for 6 h at a ramp/cooling rate of 1 °C/min under a dry air flow of 100 mL/min in a tubular furnace.

The resulting nanosheets were analyzed by argon adsorption/desorption isotherm.

Centrifugation of the calcined nanosheets

To acquire the SDA-free MFI nanosheets, a simple centrifugation of the calcined MFI nanosheets was carried out. The calcined MFI nanosheet powder was re-dispersed into DI water and then centrifuged at 1,700 RCF for 30 s in order to precipitate big aggregated particles at the bottom of the centrifuge tube. To collect light, less or not aggregated calcined MFI nanosheets, the top of the supernatant was pipetted out.

Disaggregation of the calcined nanosheets at mild temperature

The MFI nanosheets calcined at the mildest temperature, 300 °C, underwent the exfoliation process with polystyrene (hereafter called the "disaggregation process") to disaggregate the calcined nanosheets inspired by exfoliation of multilamellar MFI nanosheets. 0.1 g of the calcined MFI nanosheets under the mild condition was injected into the DSM melt compounder at 120 °C followed by the injection of 11.9 g of polystyrene (MW 1,500) at 120 °C. After injection of the calcined MFI nanosheets and polystyrene, the mixture was blended under a nitrogen environment at a screw speed of 500 rpm. The temperature was elevated to 150 °C for 30 min for mixing. Subsequently, the temperature was reduced to 60 °C for 30 min to attain a high degree of disaggregation. The final product was extruded in nanocomposite solid form at 60 °C. The resulting nanocomposite, consisting of polystyrene, disaggregated SDA-free MFI nanosheets, and aggregated SDA-free MFI nanosheets, was examined by TEM analysis to confirm the degree of disaggregation. For the TEM analysis, the nanocomposite was microtomed by a diamond knife to prepare a 100~200 nm thin film mounted on a TEM

grid.

To purify the disaggregated SDA-free MFI nanosheets, the entire nanocomposite was dissolved into toluene, which is a good solvent for the polystyrene. The solution was centrifuged at 40,000 RCF for 3 h at 4 °C for polystyrene removal. The calcined MFI nanosheet particles were precipitated at the bottom of the centrifuge tube in a cake form and; the supernatant was composed of polystyrene. The supernatant was discarded and the cake was re-dispersed in toluene and re-centrifuged at 40,000 RCF for 3 h at 4 °C. The cake was re-dispersed in toluene and then placed on top of a chlorobenzene layer on the basis of density differences. Chlorobenzene was chosen as a bottom layer since it is not a good solvent for polystyrene and is heavier than toluene. The two layers were centrifuged at 40,000 RCF for 3 h at 4 °C to cause the calcined MFI nanosheets to settle down. The polystyrene was floated in supernatant due to its low density compared to the MFI nanosheets and the low solubility in the chlorobenzene. Polystyrene elimination was examined through TEM analysis after re-dispersion of the MFI nanosheet cake in octanol.

Since the density of the aggregates is higher than that of the disaggregated MFI nanosheets, density gradient centrifugation (DGC)—inspired by the purification step of exfoliated MFI nanosheet—was applied in order to purify the disaggregated SDA-free MFI nanosheets. A chloroform layer (ρ=1.48 cc/g) was placed at the bottom and atop the chloroform layer, a dichloromethane layer (ρ=1.33 cc/g) was formed. Atop the dichloromethane layer, a chlorobenzene layer (ρ=1.10 cc/g) was created, while atop the chlorobenzene layer, a thin buffer layer of octanol (ρ=0.82 cc/g) formed. Then the

octanol suspension of SDA-free MFI nanosheet was placed on top of that the octanol buffer layer. The whole layers were centrifuged at 12,000 RCF for 30 min at room temperature. After the DGC, the top octanol layer was collected and analyzed by TEM. The octanol suspension was deposited on a porous α-Al_2O_3 support by vacuum-assisted coating and the morphology of the deposited layer was analyzed by SEM.

Carbonization and calcination in the presence of polymer networks

To collect light nanosheets and remove unreacted silica, the as-synthesized MFI nanosheets were centrifuged. 2 mL of as-synthesized MFI nanosheet suspension was centrifuged at 1,700 RCF for 30 s leading to precipitation of intergrown nanosheets and nanosheets with significant seed thickening. The top 1 mL of the supernatant was transferred to another centrifuge tube and diluted with 1 mL of DI water. The diluted supernatant was centrifuged three times at 14,500 RCF for 1 min to eliminate unreacted silica. The purified MFI nanosheets were re-dispersed in DI water to form 5 wt% suspension by weight. 0.614 g of acrylamide (AM, $\geq$ 99 %, Sigma-Aldrich) and 0.61 mg of *N*,*N*'-methylenebisacrylamide (MBAM, 99 %, Sigma-Aldrich), which are water soluble monomers, were added to 6.14 g of the 5 wt% purified MFI nanosheets suspension. Then 15.4 mg of ammonium persulfate ($(NH_4)_2S_2O_8$, $\geq$ 99 %, Sigma-Aldrich), an initiator of polymerization, was added. After the monomers were dissolved, the mixture was ultrasonicated for 15 min to ensure complete dispersion of the as-synthesized MFI nanosheets. The aqueous solution was heated at 50 °C for 5.5 h to polymerize the organic monomers. The solid polymer/as-synthesized MFI nanosheet composite was dried overnight at 70 °C. The dried nanocomposite was heated at 550 °C

for 2 h at a ramp rate of 1 °C/min under a nitrogen flow of 100 mL/min to carbonize the polymer, and then it was calcined at 550 °C for 3 h at a ramp rate of 1 °C/min under a dry air flow of 100 mL/min. The resulting MFI nanosheets were re-dispersed in DI-water for further analysis by SEM.

Applications of *Fenton chemistry*

To validate SDA elimination as reported in the literature, aluminosilicate (Si/Al=16) BEA nano-crystals, which in the literature were employed for the *Fenton* treatment, was synthesized by a well-established recipe.[111] 0.272 g of anhydrous sodium aluminate ($NaAlO_2$, Sigma-Aldrich) was dissolved in 1.145 g of DI water as an aluminum source, and then 0.16 g of NaOH (97 %, Sigma-Aldrich) was added. After stirring for 10~15 min, 29.855 g of TEAOH (20 %, Sigma-Aldrich) was added and then stirred for 30 min. During stirring 4.8 g of fumed silica (Cabosil M5, Riedel de Haën) was added to the solution as a silica source. The gel was stirred for 6 h at room temperature and then transferred to a Teflon-lined stainless-steel autoclave. The gel was heated at 140 °C for 5 days under a static condition. The synthesized aluminosilicate BEA was recovered by centrifugation at 20,000 RCF for 20 min at room temperature until the pH of the supernatant appeared to be below 9. The nano-crystal aluminosilicate BEA (Si/Al=16) was acquired after drying at 70 °C overnight.

The 0.3 g of the BEA (Si/Al=16) was dispersed in 50 g of hydrogen peroxide (H_2O_2, 30 %, Fischer Scientific), and then it was transferred into an oil bath at 80 °C connected with a condenser (solution A). 0.013 g of iron (III) nitrate ($Fe(NO_3)_3$, $\geq$ 98 %, Sigma-Aldrich) was dissolved into 50 g of H_2O_2 while the H_2O_2 was dipped into an ice bath (solution B).

The ice bath cooled down the solution while the hydroxyl radicals were generated. After the complete dissolution of the $Fe(NO_3)_3$, solution B was added to solution A dropwise. After the addition of solution B into A was completed, oxidation of the SDA molecules took place at 80 °C for 2 h. The resulting aluminosilicate BEA nano-crystals were recovered by centrifugation at 20,000 RCF for 10 min. The supernatant was discarded and DI water was added to re-disperse the BEA nano-crystals in a cake form. The re-dispersed BEA nano-crystals were centrifuged three times at 2,000 RCF for 10 mins. An aliquot of the collected BEA nano-crystals were dried for argon adsorption/desorption analysis and the rest were re-dispersed in DI water.

The oxidation of SDA molecules of MFI nanosheets was prepared in the same manner as the aluminosilicate BEA nano-crystals. The solution A contained the MFI nanosheets instead of the aluminosilicate BEA (Si/Al=16) nano-crystals.

Characterization

The morphology of MFI nanosheets was observed by SEM and TEM. Microporosity was determined by argon adsorption/desorption isotherm at 87 K.

4.3 Results and discussion

De-templation under mild calcination

To minimize the degree of aggregate formation, the calcination temperature was varied from 300 °C to 550 °C under a dry air flow. As expected, with calcination temperature, aggregates were significantly formed (**Figure 4-1**). Under mild conditions of calcination, single nanosheets were observed as indicated by the arrows in **Figure 4-1A** and **B**.

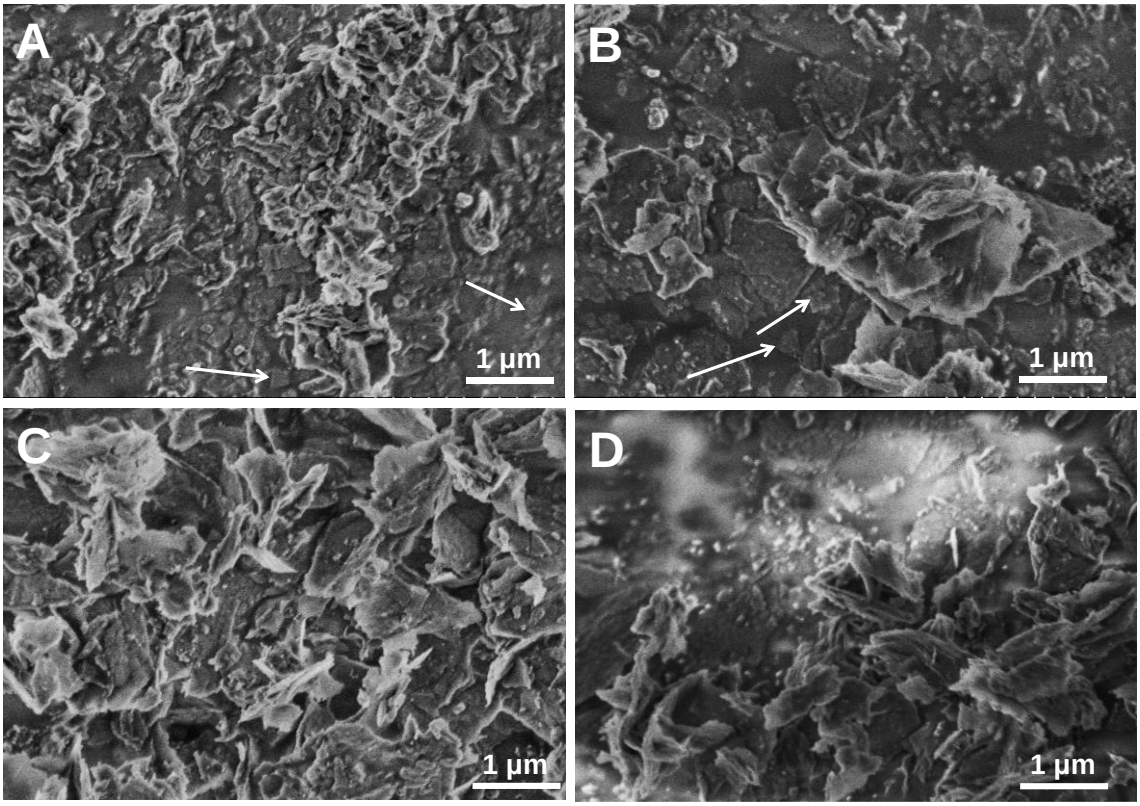

Figure 4-1. SEM images of the calcined MFI nanosheets at 300 °C (A), 350 °C (B), 450 °C (C), and 550 °C (D). Each calcination was carried out at a ramp rate of 1 °C/min for 6 h under a dry air flow of 100 mL/min in a tubular furnace. Arrows indicate single MFI nanosheets after calcination.

Perhaps this can be attributed to the relatively low thermal energy provided during the mild calcination process. In contrast, calcination at high temperature led to the formation of aggregates (**Figure 4-1C** and **D**).

Purification of de-templated nanosheets under mild condition

To purify the single MFI nanosheets after calcination at 300 °C (indicated by arrows in **Figure 4-1A**), a simple centrifugation of water suspension of the calcined MFI nanosheets was applied. The water suspension was centrifuged at 1,700 RCF for 30 s in order to precipitate aggregates. To recover light single nanosheets in the supernatant, the

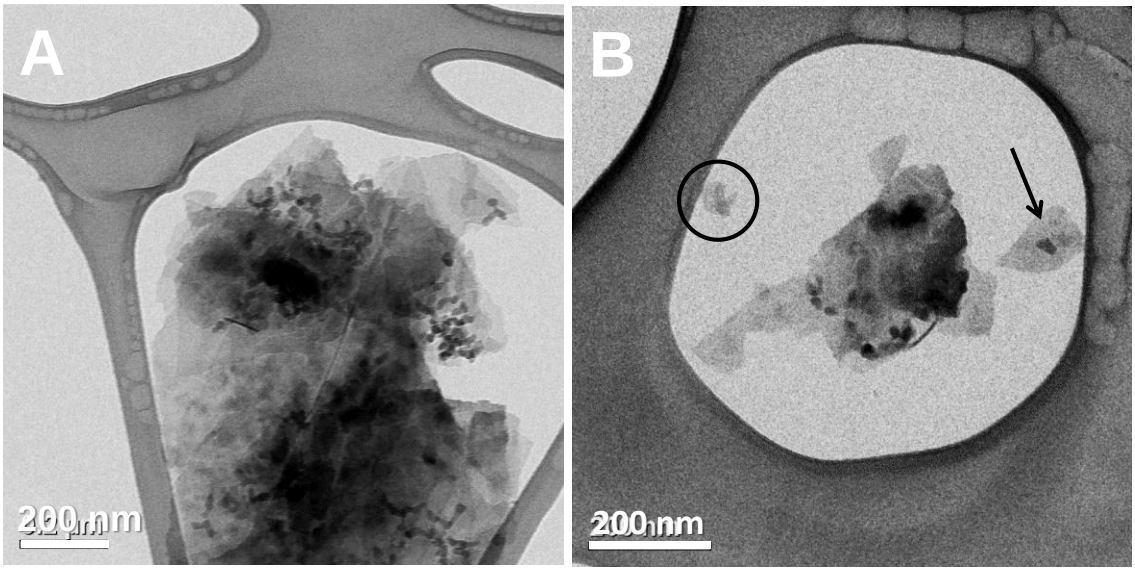

Figure 4-2. TEM images of aggregates after collecting the top part of the supernatant following centrifugation of the mildly calcined MFI nanosheet suspension (A) and a mixture of aggregates and a single nanosheet marked by an arrow after collection of the top part of the supernatant (B). An arrow indicates a single nanosheet and a circle indicates small aggregates composed of small pieces of nanosheets.

top portion of the supernatant was collected and subjected to TEM analysis. TEM examination of the morphology of the top part of the supernatant revealed that a major part of it was composed of aggregates (**Figure 4-2A**). However, as indicated by the arrow in **Figure 4-2B**, a small number of single nanosheets was also present, as were aggregates of tiny pieces of nanosheets (indicated by the circle in **Figure 4-2B**). Given how difficult it is to separate the small aggregates from the single MFI nanosheets via centrifugation, some other strategy should be employed to separate the aggregates of small pieces of the nanosheets.

Disaggregation of calcined nanosheets with a polymer by melt blending

To increase the yield of SDA-free single nanosheets, a disaggregation process with

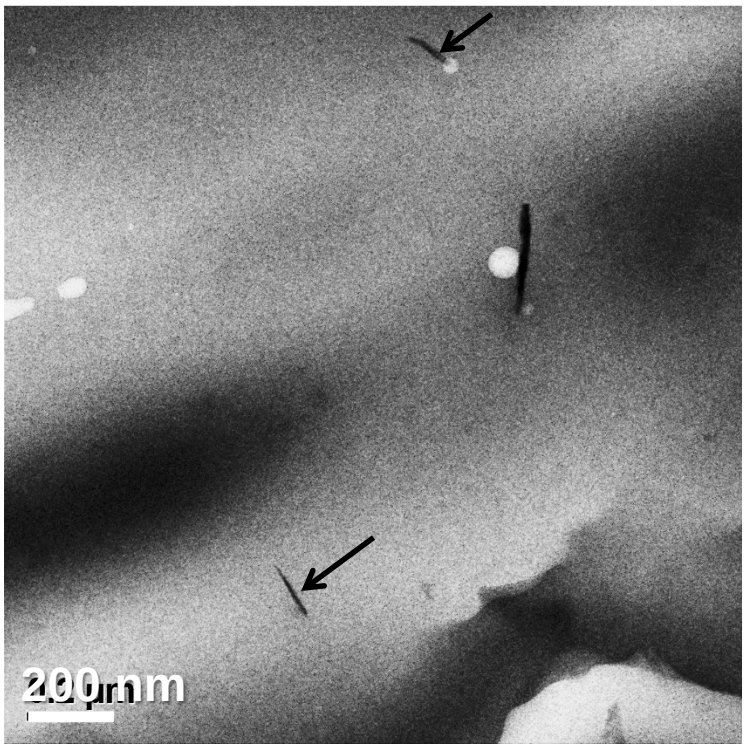

Figure 4-3. A TEM image of a microtomed sample of calcined MFI nanosheets/polystyrene nanocomposite after a disaggregation step. Arrows indicate disaggregated single SDA-free MFI nanosheets.

polystyrene was conducted mimicking melt extrusion to exfoliate the multilamellar MFI nanosheets. At 150 °C, the high temperature provides high mobility of the polystyrene melts to diffuse into spaces between the calcined MFI nanosheets.. At 60 °C, the polystyrene behaves like a solid generating high shear forces that improve the yield of the disaggregation. To ensure disaggregation, the resulting calcined MFI nanosheets/polystyrene nanocomposite was microtomed with a diamond knife for TEM analysis. **Figure 4-3** exhibits the dispersion of disaggregated calcined MFI nanosheets, indicated by arrows, in the polystyrene matrix.

To collect the disaggregated MFI nanosheets and eliminate the polystyrene, a post treatment DGC was applied. Octanol was chosen as a solvent for the final suspension of

the disaggregated MFI nanosheets since it was expected that the hydroxyl group in octanol can interact with silanol groups at the external surface of the SDA-free MFI nanosheets. Simultaneously, relatively long hydrocarbon chains of octanol molecules may interact with one another at the external surface of the de-templated MFI nanosheets and likely lead to forming barriers preventing the de-templated MFI nanosheets from interacting one another to form aggregates. **Figure 4-4** shows the schematic of the DGC and TEM images of the corresponding layers. The aggregated SDA-free MFI nanosheets were presented in three bottom layers: in chloroform (**Figure 4-4A**), in dichloromethane (**Figure 4-4B**), and in chlorobenzene (**Figure 4-4C**). In contrast, the top layer of octanol (**Figure 4-4D**) reveals well-dispersed disaggregated SDA-free MFI nanosheets that owe their existence to the relatively low density of the disaggregated SDA-free MFI nanosheets. The resulting disaggregated SDA-free MFI nanosheets (**Figure 4-4D**) are smaller than the parent MFI nanosheets, perhaps since the high shear forces generated during the disaggregation break the MFI nanosheets into small pieces. Nonetheless, as shown in high magnification TEM image (**Figure 4-4E**), the crystallinity of the disaggregated MFI nanosheets was preserved, confirmed by a corresponding electron diffraction pattern (**Figure 4-4F**). The electron diffraction pattern (**Figure 4-4F**) indicates a single *b*-oriented MFI crystal, which implies that the disaggregation process was successful.

The octanol suspension composed of the disaggregated SDA-free MFI nanosheets was deposited on a porous α-Al_2O_3 support by a vacuum-assisted coating (**Figure 4-5**). **Figure 4-5A** illustrates that the coating layer is not uniform and has roughness. The

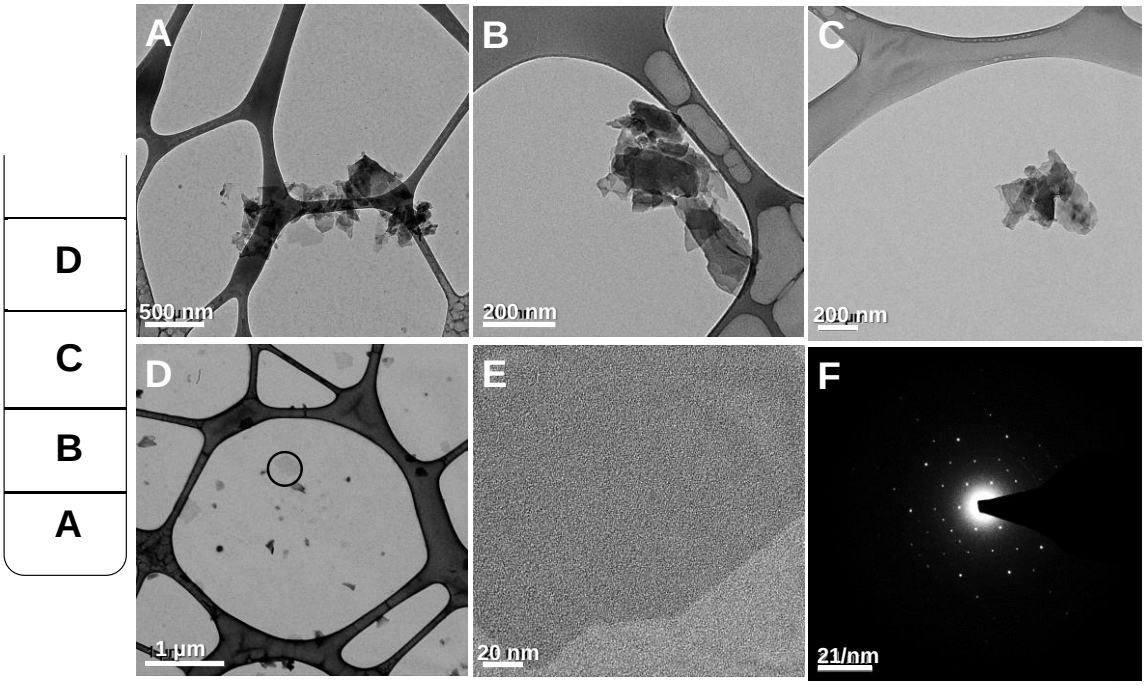

Figure 4-4. Schematic of DGC (left) and TEM images of the corresponding layers (A-D): chloroform (A), dichlorobenzene (B), chlorobenzene (C), and octanol (D). E is a high magnification TEM image of a particle marked by a circle in D and F is a corresponding electron diffraction pattern.

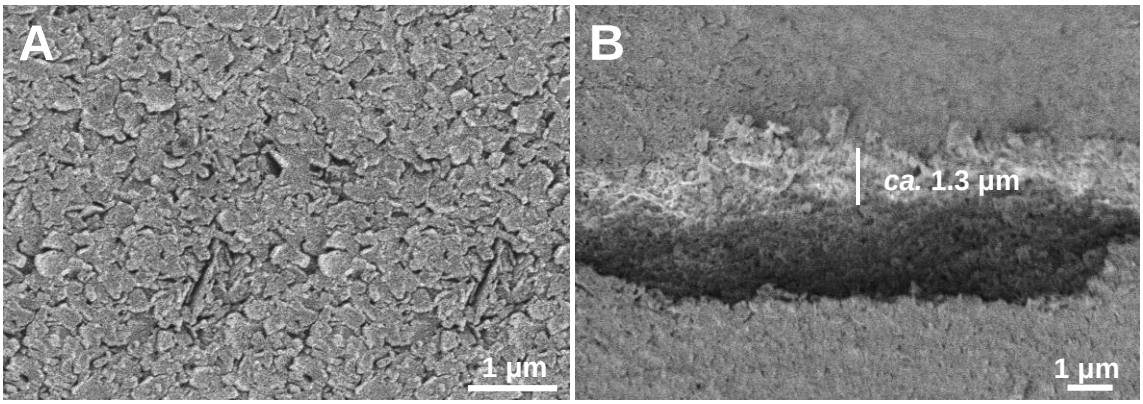

Figure 4-5. SEM images of the deposition of the octanol suspension that contains the disaggregated SDA-free MFI nanosheets on a porous α-Al_2O_3 support (A), and a cross section view (B).

rough surface of the coating was also examined by cross-section view of the coating

(**Figure 4-5B**). The non-uniformity of the deposited film perhaps stems from a re-aggregation of the disaggregated SDA-free MFI nanosheets that was caused by the instability of the nanosheets in octanol. To examine re-aggregation, the old octanol suspension of disaggregated SDA-free MFI nanosheets after it had been stored overnight was analyzed by TEM. Re-aggregation of the disaggregated SDA-free MFI nanosheets occurred even after 1 h sonication (**Figure 4-6**). The result suggests that octanol should not be used to stabilize the disaggregated SDA-free MFI nanosheets. Perhaps the affinity between octanol molecules is higher than it is between octanol and the disaggregated SDA-free MFI nanosheets.

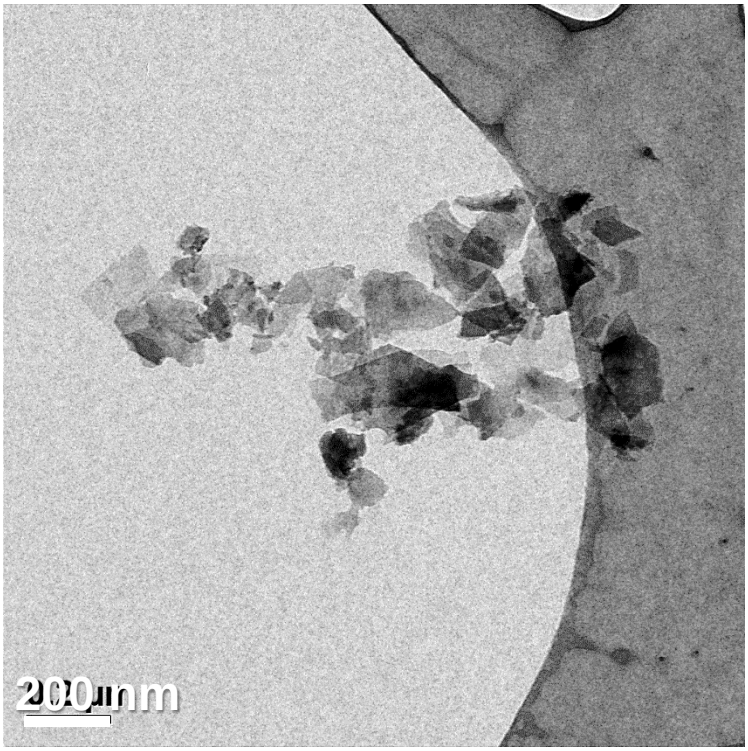

Figure 4-6. A TEM image of the octanol suspension of the disaggregated SDA-free MFI nanosheets following their overnight storage.

Before exploring other solvents for affinity with the disaggregated SDA-free MFI nanosheets, the yield of the disaggregation process was determined on the basis of the thickness of the deposited layer (**Figure 4-5B**). The objective was to determine whether further investigation on the disaggregation process was worthwhile. An approximately 1.3 μm thick coating layer (**Figure 4-5B**) resulted from deposition of 12.41 g of the octanol suspension of the disaggregated SDA-free MFI nanosheets. Under the simplest assumption that the coating is a continuous layer without any defects, the volume of the film is 2.95×10^{-10} m^3. Taking 1.836 g/cm^3 as the density of MFI, the total weight of the deposition of the disaggregated SDA-free MFI nanosheets was evaluated by dividing the volume of the film by the density of MFI. Consequently, the total weight of the disaggregated SDA-free MFI in the coating layer is 5.42×10^{-4} g. In the one batch of the disaggregation process, the total amount of the octanol suspension of the disaggregated SDA-free MFI nanosheets was 34.36 g. This included the deposited amount. Assuming that the octanol suspension of the disaggregated SDA-free MFI nanosheet is homogeneous, and judging from the back-calculation, the total amount of the disaggregated SDA-free MFI nanosheets suspended in octanol is 1.5×10^{-3} g. The disaggregated process was started with 0.1 g of the calcined SDA-free MFI nanosheets. Consequently, 1.5×10^{-3} g of disaggregated SDA-free MFI nanosheets were acquired from 0.1 g of the calcined SDA-free MFI nanosheets. The yield of the disaggregation process was 1.5 %. However, the apparent yield must be lower than 1.5 % since the deposited film of the disaggregated MFI nanosheets is neither continuous nor defect-free. Given that the disaggregation breaks the MFI nanosheets into small pieces, an approach

that preserves crystal size of the parent MFI nanosheets with high yield should be sought.

Carbonization and calcination in the presence of polymer networks

Water soluble organic monomers, *i.e.* AM and MBAM, were polymerized in 5 wt% of the as-synthesized MFI nanosheet suspension to create networks between the MFI nanosheets. After polymerization (**Figure 4-7A**), and due to the polymer matrix, the MFI nanosheets were not observed. The MFI nanosheet/polymer nanocomposite was carbonized under a nitrogen flow. Carbonization resulted in a black powder product. SEM images (**Figure 4-7B** and **C**) show that the majority of the resulting MFI nanosheets are aggregated after carbonization, which suggests that carbonization cannot prevent aggregate formation. The carbonized MFI nanosheet/polymer nanocomposite was subsequently calcined under an air flow.

Calcination led to a white powder, which indicates combustion of the carbon networks. After calcination (**Figure 4-7D**) the MFI nanosheets formed aggregates, the majority of which appeared to be merged together. The calcined powder was re-dispersed into DI water and the morphology was examined by SEM. In the water suspension, the MFI nanosheets formed aggregates (**Figure 4-7E**). Perhaps this is the result of poor mixing while polymerization of the organic monomers took place. When the water soluble organic monomers are dissolved, the solution with loading of 5 wt % of the as-synthesized MFI nanosheets became viscous, and it may have disturbed a good and homogeneous mixing of the monomers and MFI nanosheets. A possible solution might be to reduce the loading of the nanosheets. Before verifying that mixing can be improved by decreasing the loading of the MFI nanosheets, other characterization was carried out

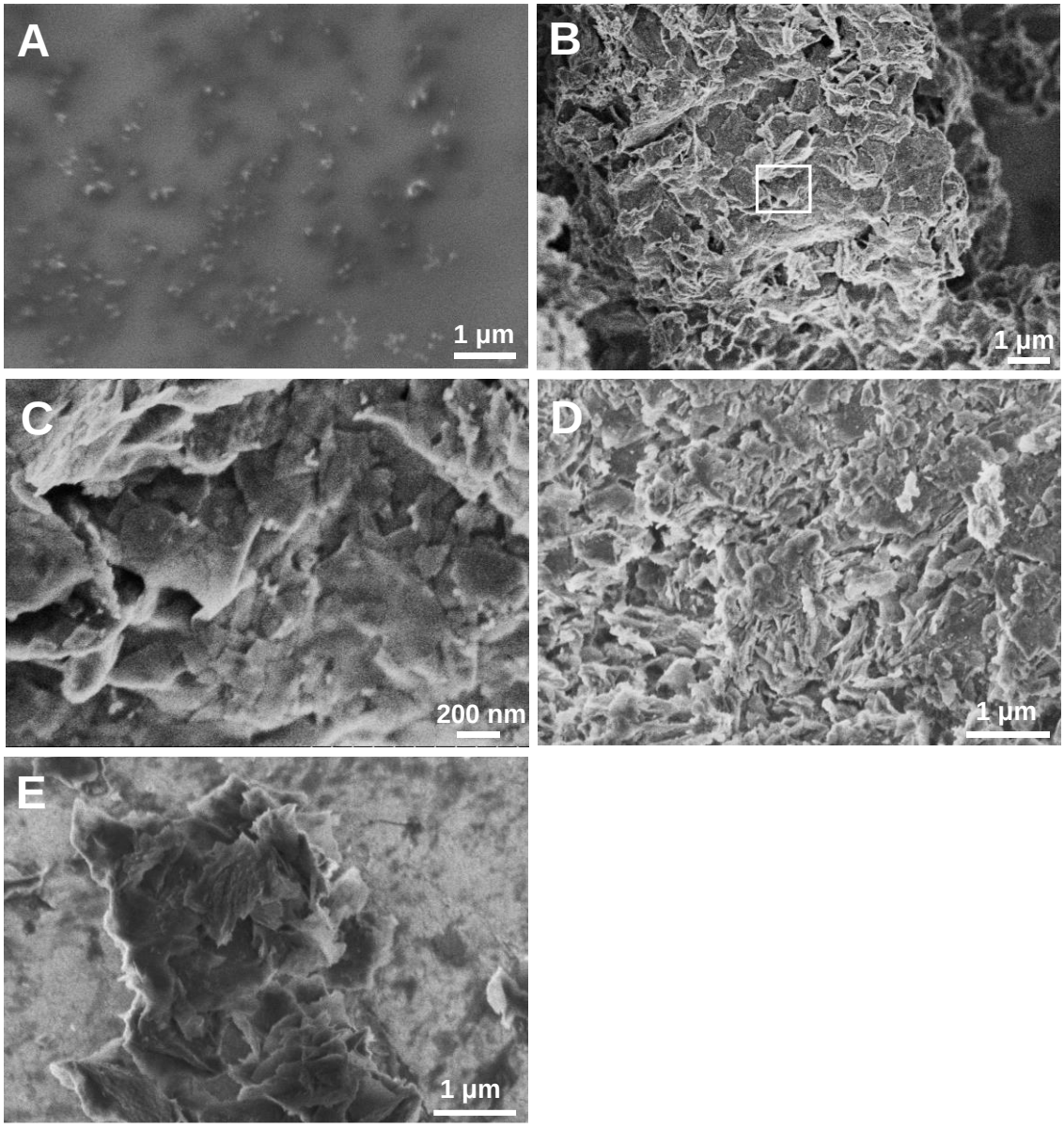

Figure 4-7. SEM images of MFI nanosheets prepared with a polymer network barrier: after drying (A), after carbonization at low magnification (B) and at high magnification (C), after calcination (D), and re-dispersion in DI water (E). A SEM image C is a magnified image of an area indicated by a rectangle in image B.

such as evaluating the crystallinity of the resulting MFI nanosheets by XRD. Here the goal was to determine whether attempting a further investigation of the carbonization of the polymer matrix was worthwhile. The crystallinity of the calcined MFI nanosheets was

reduced based on a lack of well-defined facets on the MFI, as exhibited in **Figure 4-7D** and **E**.

To verify the crystallinity of the calcined MFI nanosheets from the carbon/MFI nanosheet composites, the XRD pattern was compared to as-synthesized MFI nanosheets and conventionally calcined MFI nanosheets at 550 °C. At 23~25 degrees of two theta range, the intensity of the peaks appeared to be lower in the calcined MFI nanosheets from carbon/MFI nanosheet composite than in the as-synthesized and the conventionally calcined MFI nanosheets (**Figure 4-8A**). It implies that the treatment destroyed the crystallinity of the MFI nanosheets. The argon isotherm was exploited to verify the crystallinity of the calcined MFI nanosheets from carbon/MFI nanosheet composites (**Figure 4-8B**). While as-synthesized MFI nanosheets did not reveal microporosity, the calcined nanosheets prepared from the carbon/MFI nanosheet composites had micropore openings, as indicated by argon adsorption amounts at zero relative pressure (**Figure 4-8B**). However, as illustrated in **Figure 4-8B**, the adsorbed argon amount at zero relative pressure is lower in calcined MFI nanosheets made from carbon composite than in conventionally calcined MFI nanosheets. This implies a loss of microporosity caused by the destruction of crystallinity. The argon isotherm is consistent with XRD, which indicates that destruction of crystallinity may result from a rise temperature caused by carbon combustion. In general, the combustion process is highly exothermic and this leads to non-controllable temperature rising. Moreover, the fact that carbon is a major component of carbon/MFI nanosheet composites may cause a higher temperature than the set point of the furnace during calcination. When the loading of the MFI nanosheets is

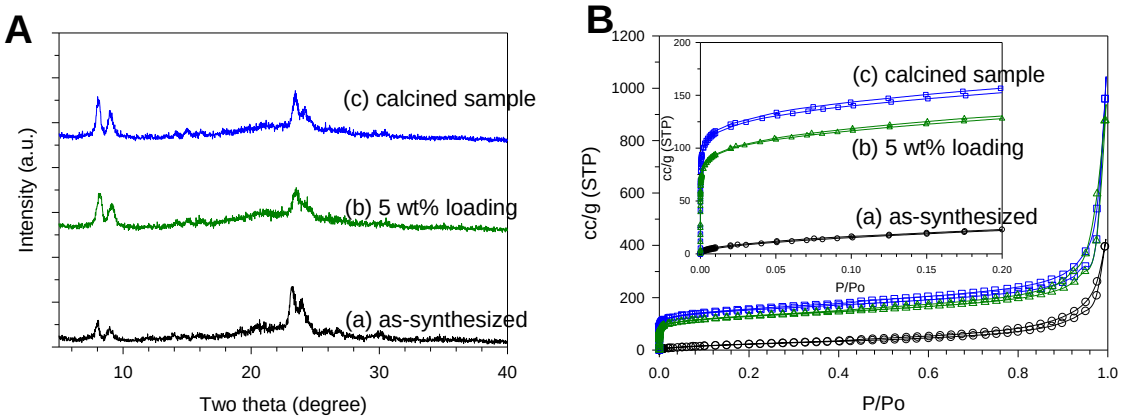

Figure 4-8. XRD patterns (A) of (a) as-synthesized MFI nanosheets, (b) MFI nanosheets prepared with a polymer network barrier with 5 wt% loading, and (c) calcined MFI nanosheets at 550 °C. Argon isotherms (B) of (a) as-synthesized MFI nanosheets, (b) MFI nanosheets prepared with a polymer network barrier with 5 wt% loading, and (c) calcined MFI nanosheets at 550 °C. Inset of B magnifies the low relative pressure regime.

decreased for good mixing, increases in the composition of the carbon might lead to even higher temperature due to the exothermic combustion. The heat generated during calcination may result in destruction of the crystallinity of the MFI nanosheets, which suggests that calcining carbon does not contribute usefully to the preparation of de-templated MFI nanosheets.

Applications of *Fenton chemistry*

To prevent the loss of crystallinity and aggregate formation during SDA removal, non-thermal treatment should be used. Via *Fenton chemistry*, the organic molecules are likely oxidized by the hydroxyl radicals generated from hydrogen peroxide in the presence of iron ions. The first discovery of applicability of the *Fenton chemistry* in template elimination was reported by Melián-Cabrera's group in the case of aluminosilicate BEA

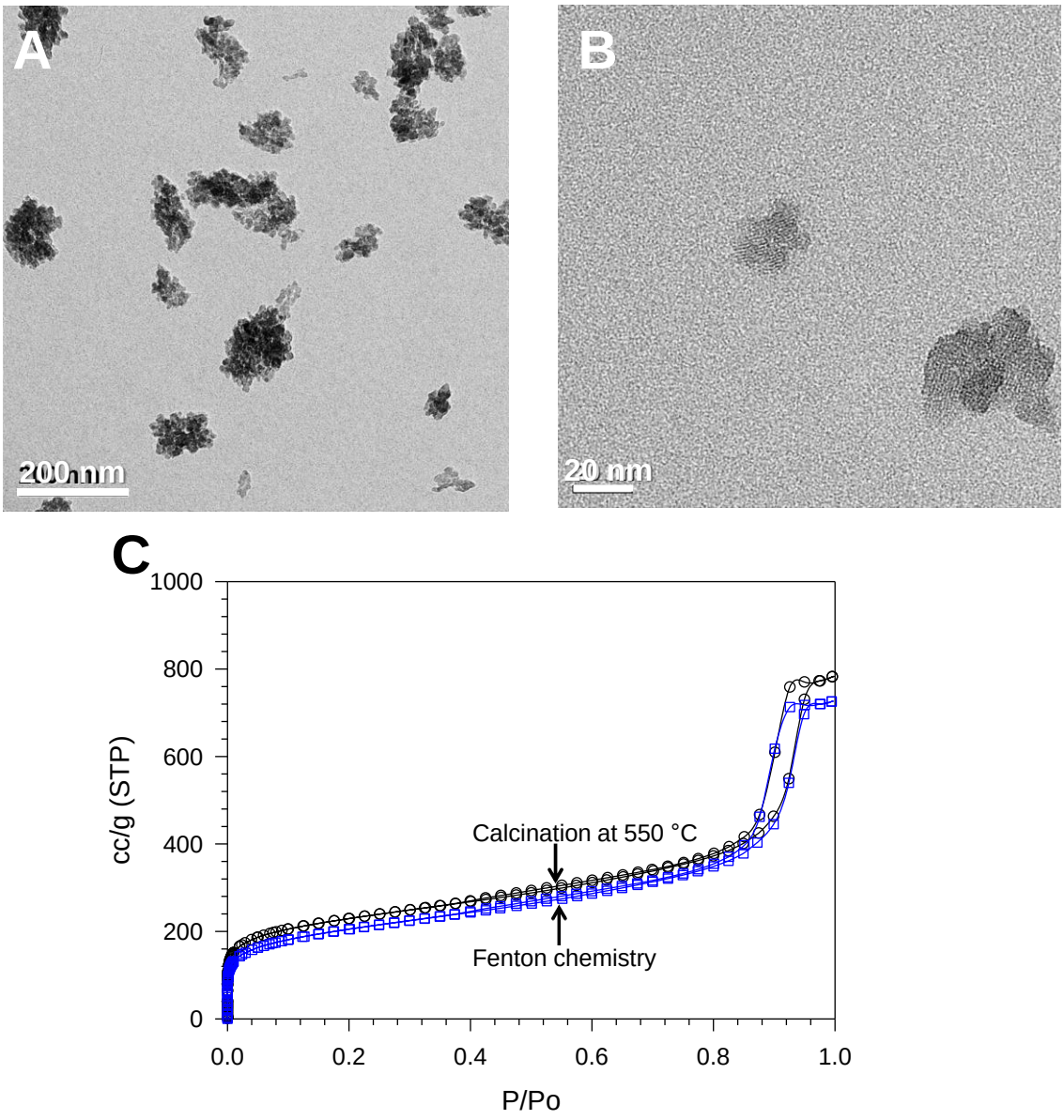

Figure 4-9. TEM images of synthesized aluminosilicate BEA (Si/Al=16) nano-crystals at low magnification (A) and at high magnification (B). Argon isotherm of calcined aluminosilicate BEA at 550 °C and the BEA with *Fenton* treatment (C).

nano-crystals.[67] To validate the *Fenton chemistry*, *ca.* 20 nm aluminosilicate BEA nano-crystals were prepared first from the well-established recipe (**Figure 4-9A** and **B**).[111] The aluminosilicate BEA nano-crystals were calcined at 550 °C for 6 h at a ramp rate of

1 °C/min under a dry air flow of 100 mL/min and then argon adsorption/desorption analysis was conducted for comparison. The adsorbed argon amount at zero relative pressure was comparable to the literature value[111] (**Figure 4-9C**).

The micropore opening of the *Fenton* treated aluminosilicate BEA was evaluated by comparing it with the argon isotherm of the template-free aluminosilicate BEA by calcination. As seen in **Figure 4-9C**, the degree of micropore opening of aluminosilicate BEA nano-crystal via the *Fenton chemistry* was the same as the conventional thermal treatment (i.e., calcination).

After validation of the *Fenton chemistry* in the case of aluminosilicate BEA nano-crystals, the MFI nanosheets were treated using *Fenton chemistry* and then the extent of the micropore opening was determined by argon isotherm. In the case of the as-synthesized MFI nanosheets, SDAs were occluded in the micropores of the zeolite framework (**Figure 4-10**), and hence compared to the calcined MFI nanosheets at 550 °C, no micropore opening occurred. Assuming that the adsorbed amount of argon at zero relative pressure on the calcined MFI nanosheets at 550 °C indicates the completion of micropore opening, the relative micropore opening can be evaluated by comparing the adsorbed amounts of argon at zero relative pressure to other samples calcined at 300 °C and 250 °C under mild conditions and to *Fenton* treated MFI nanosheets. Under *Fenton chemistry*, *ca.* 40 % of SDAs by volume in the micropores of the MFI zeolite framework were eliminated (**Figure 4-10**). Eliminating the SDAs of MFI nanosheets is moderately efficient compared to the procedure in the case of nano-crystals of aluminosilicate BEA nano-crystals. Perhaps this is associated with smaller micropore size of the MFI zeolite

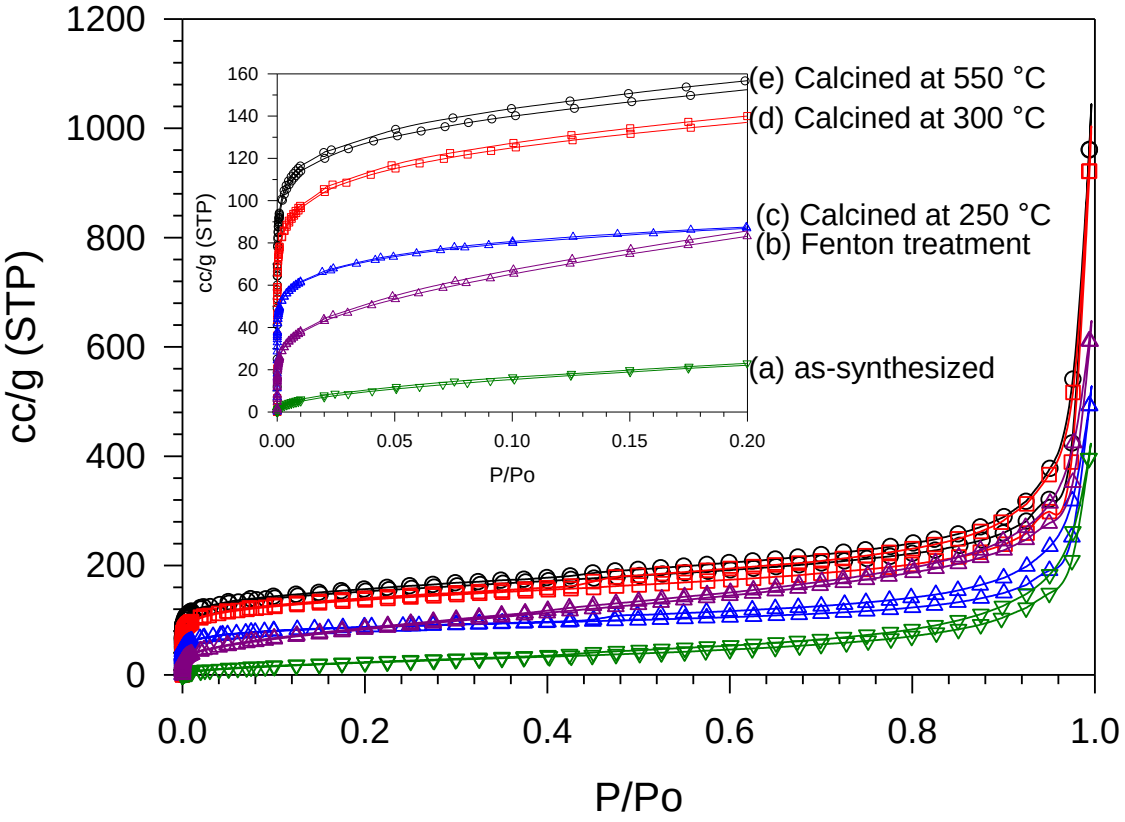

Figure 4-10. Argon adsorption/desorption measurements of (a) as-synthesized MFI nanosheets, (b) MFI nanosheets with the *Fenton* treatment, (c) MFI nanosheets calcined at 250 °C, (d) MFI nanosheets calcined at 300 °C, and (e) MFI nanosheets calcined at 550 °C. Inset magnifies low relative pressure regime.

framework (*ca.* 5.6 Å). The micropore size of BEA framework is approximately 7 Å, which is bigger than that of MFI framework. Consequently, it is likely that hydroxyl radicals may diffuse into the micropores of the BEA zeolite framework and that the products after oxidation may diffuse out of the micropores simultaneously. Crystal thickness might also play an important role. The aluminosilicate BEA nano-crystals had a narrow thickness (or size) distribution and the size of the nano-crystals was approximately 20 nm (**Figure 4-9B**).

However, as discussed in Chapter 2, the thickness of MFI nanosheets varies form thin nanosheet areas (*ca.* 5 nm) to thick seeds at the center (~100 nm). Also, there is thickening around the thick seed, and this may cause mass transport limitations. The 40 % of removal of SDAs by volume might correspond to the average thin part of the nanosheets.

A TEM image of the MFI nanosheets after the *Fenton* treatment (**Figure 4-11A**) illustrates that there are few changes in crystal morphology and that aggregates are not present. The preservation of the crystallinity of the MFI nanosheets after the *Fenton* treatment is confirmed by an electron diffraction pattern (**Figure 4-11B**).

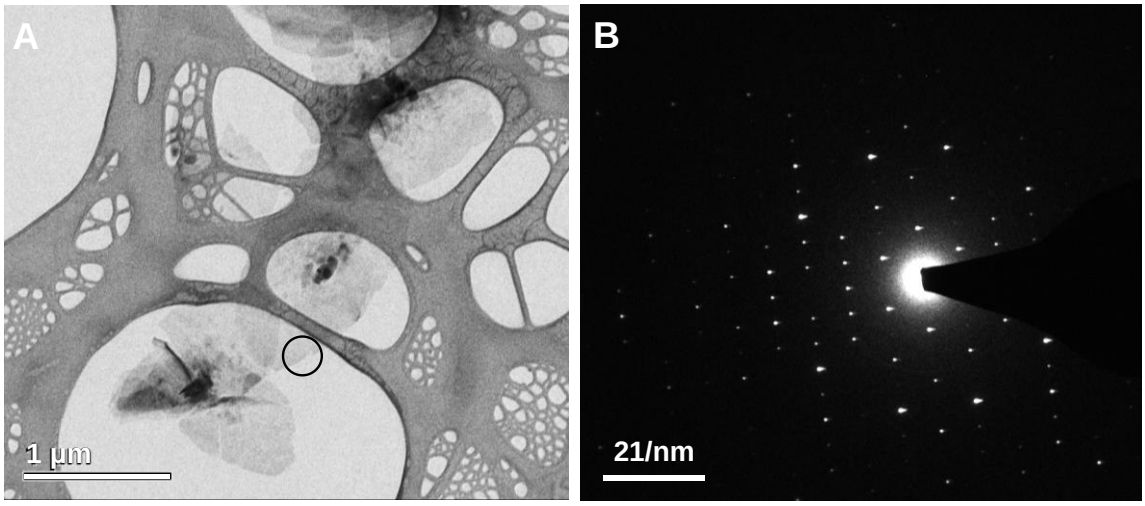

Figure 4-11. A TEM image of MFI nanosheets after the *Fenton* treatment (A) and an electron diffraction pattern (B). The electron diffraction pattern was acquired in the area indicated by a circle in A.

The results from argon adsorption/desorption isotherm and TEM analysis indicate that it would be difficult to completely eliminate SDA without destroying crystallinity and facilitating aggregate formation. However, the *Fenton chemistry* can be used to replace

the conventional calcination step and thus remove SDAs from the zeolite framework without destroying crystallinity and forming aggregates, although it might partially open micropores in the zeolite framework.

4.4 Conclusion

This chapter discusses a number of attempts to remove SDAs in order to improve the processability of MFI nanosheets with polymers with the objective of reducing production costs. First, a simple centrifugation of calcined nanosheets under a mild condition (calcination at 300 °C) was carried out with the goal of settling down aggregates in a cake form; a small portion of the nanosheets does not aggregate after the mild calcination. This attempt to separate individual nanosheets did not proceed as efficiently as expected. To enhance the yield of single nanosheets obtained through centrifugation after mild calcination, inspired by exfoliation of multilamellar MFI, the disaggregation step was carried out followed by DGC. During the initial state of disaggregation, individual nanosheets were segregated and well dispersed in octanol, as confirmed by TEM imaging. However, in the stored octanol suspension, the disaggregated nanosheets again formed aggregates—a development detrimental to the uniform deposition of nanosheets on the porous supports. Thus, the coated layer of the octanol suspension onto a porous α-Al_2O_3 support is not uniform, and the yield at best is 1.5 %.

To prepare the SDA-free nanosheets, an alternative method designed by Yan's group that uses polymer networks was applied.[97] The fact that polymer networks help to create

spaces between zeolite nano-crystals may reduce the possibility that zeolite nanocrystals approach each other closely, thereby causing condensation during thermal treatment. This method is effective in the case of small nano-crystals according to the literature but not MFI nanosheets. The polymer network does not prevent MFI nanosheets from forming aggregates whose presence can be attributed to poor mixing. Additionally, XRD and argon isotherm analysis indicate that zeolite crystallinity is not preserved—it probably can be attributed to uncontrolled heat generated from the carbonized polymer networks during calcination.

In the three different attempts mentioned above, thermal treatment and aggregate formation are inevitable. This suggests that it is not feasible to prepare SDA-free MFI nanosheets using approaches that require thermal treatment. Oxidizing SDA molecules through *Fenton chemistry,* during which hydrogen peroxide generates hydroxyl radicals in the presence of iron ions, most effectively eliminates SDAs. Melián-Cabrera's group was the first to use *Fenton chemistry* to successfully eliminate SDA from aluminosilicate BEA nano-crystals.[67] To demonstrate the feasibility of the *Fenton* treatment for SDA removal, aluminosilicate BEA nano-crystals were prepared for the oxidation. Based on the argon isotherm, SDAs from the aluminosilicate BEA nano-crystals were successfully eliminated. However, in the case of the MFI nanosheets, the *Fenton* treatment opened only *ca.* 40 % of the micropores by volume. The partial removal of SDAs may stem from the fact that the pore size of the MFI is smaller than that of the BEA.Moreover, the thin portion of the nanosheets (*ca.* 5 nm) has a relatively low mass transport resistance, and hence 40 % of the SDA elimination by volume may result from the thin part of the

nanosheets. Although complete SDA removal out of zeolite was not achieved, *Fenton chemistry* can be used productively to prepare de-templated MFI nanosheets. In this method, aggregates do not form and crystallinity is not lost. Furthermore, if the nanosheets have less seed thickneing, *Fenton chemistry* might eliminate more SDAs from the zeolite framework. In that case, the use of SDA-free MFI nanosheets might reduce the cost of producing zeolite membranes when they are combined with polymer materials.

Chapter 5: Probing effects of silanol groups on adsorption of ethanol onto zeolites

5.1 Introduction

Zeolites are effective adsorbents that separate organic molecules from water[69,112,113] since they discriminate molecules on the basis of size/shape and functionality. One of these is silicalite-1, which is a pure silica MFI type zeolite. Adsorption occurs due to the hydrophobicity and the medium pore size (~ 5.6 Å), which can accommodate organic molecules.[114,115] The adsorption properties of ethanol onto the silicalite-1 have been intensively examined seeking a less energy-intensive means of separating ethanol.[6,10,11,116]

In theory, hydrophobic siliceous MFI crystals are supposed to increase ethanol removal from aqueous solutions. Under a base medium route synthesis, pure silica MFI crystals are presumed to be hydrophobic, but they contain silanol defects that lead to hydrophilicity, and this is detrimental to the discrimination of ethanol and water molecules. Furthermore, water molecules can form hydrogen bonds with ethanol molecules. Computational studies have predicted how water molecules influence ethanol adsorption. In a simulation study Krishna's group demonstrates that alcohol adsorbs onto hydrophobic siliceous zeolites when hydrogen bonds are formed between the alcohol and water.[117] Recently, Tsapatsis' group has demonstrated computationally that when water is present, the co-adsorption of water molecules onto hydrophobic siliceous zeolite pores occurs since water molecules form hydrogen bonds with ethanol molecules.[6,116]

This chapter probes experimentally for the first time how silanol defects of siliceous MFI

crystals affect ethanol adsorption onto siliceous MFI zeolite crystals. Additionally, this chapter studies how water molecules affect ethanol adsorption onto the siliceous MFI crystals.

5.2 Experimental

Synthesis of SPP

Tsapatsis' group recently developed a synthesis of siliceous SPP composed of 2 nm thick nanosheets that had a house-of-card arrangement.[72,118,119] 7.35 g of tetrabutyl phosphonium hydroxide (TBPOH, 40 %, TCI America) was added dropwise to 7.5 g of tetraethyl orthosilicate (TEOS, 98 %, Sigma-Aldrich) and this was stirred vigorously until a clear solution was obtained. Then 3.23 g of DI water was added to the solution, and to hydrolyze the TEOS it was stirred overnight at room temperature. The hydrolyzed sol was transferred to a Teflon-lined stainless-steel autoclave and then heated at 115 °C for 3 days under a static condition. The SPP crystals were recovered through repeated centrifugation at 40,000 RCF (Relative Centrifugal Force) for 30 min until the supernatant pH was below 9. The solid from the centrifugation was dried at 70 °C overnight and then calcined at 550 °C at a ramp rate of 1 °C/min for 12 h under a dry air flow of 100 mL/min. This was subsequently cooled to room temperature. When the calcined SPP was dispersed in DI water, the solution seemed to be acidic; indeed, the phosphonium cations converted to phosphoric acid upon calcination. To remove the phosphoric acid, the calcined SPP was washed with DI water by centrifugation at 40,000 RCF for 30 min until the supernatant pH was neutral. The washed SPP was dried at 70 °C

overnight and calcined again under the same conditions as the first calcination.

Preparation of silialite-1

Silicalite-1 (pure silica MFI) was prepared from a starting molar composition of $1SiO_2$: $0.08TPABr$: $0.4NH_4F$: $20H_2O$ via a fluoride medium route.[6,120] 1.66 g of tetrapropyl ammonium bromide (TPABr, 98 %, Sigma-Aldrich) was added to 27.62 g of distilled water, then 1.15 g of ammonium fluoride (NH_4F, 98 %, J.T. Baker) was added. After vigorous stirring at room temperature for 15 min, 4.61 g of fumed silica (SiO_2, Cabosil M5, Riedel de Haën) was added and the whole solution was hand-mixed with a spatula until it appeared to be homogeneous. The mixture was then transferred to a Teflon-lined stainless-steel autoclave and thermally treated at 175 °C for 7 days in a static condition. The resulting silicalite-1 crystals were washed via repeated centrifugation at 20,000 RCF for 20 min until the supernatant pH was neutral. The solid from the centrifugation was sonicated for 10 min for 7~10 times to eliminate amorphous silica particles. The purified particles were dried overnight in a convection oven at 70 °C. The dried silicalite-1 was calcined at 550 °C at a ramp rate of 1 °C/min for 20 h under a dry air flow of 100 mL/min. Then it was cooled to room temperature.

Aqueous ethanol solution adsorption

Ethanol (200 proof, Fisher Scientific) was diluted with DI water to prepare concentrations ranging from 0.05 wt% to 5 wt% of ethanol solution. 0.4 mL of the ethanol solution was transferred to closed glass vials and then between 50 mg and 180 mg of zeolite adsorbent was added. The zeolite-solution mixtures were stirred in a water bath until equilibration, where the temperature was 25±0.5 °C. To remove the zeolite

particles, each solution was filtered with a 1 mL Monojet syringe that was connected to a 0.2 μm GHP (polypropylene) syringe filter, and the filtrated was collected for liquid chromatography analysis.

The filtrated concentrations were analyzed using an Agilent 1200 High Performance Liquid Chromatography (HPLC) equipped with a refractive index detector (RID) and an autosampler. The autosampler injected a 20 μL sample into a stream of 0.005 M sulfuric acid (H_2SO_4) at a flow rate of 0.5 mL/min. The stream was passed through a Bio-Rad Aminex HPX-87H polystyrene packed column that was heated to 60 °C. The outlet stream was passed through a RID that was heated to 50 °C. The RID signal was recorded and plotted over time. The relative signal intensities of the ethanol and a glycerol (99.5 %, Sigma-Aldrich) that is an internal standard were employed to determine the final concentration of each solution. The difference between the initial and the final concentration of ethanol and the total volume of the solution was measured to determine how much ethanol had been adsorbed.

Vapor phase adsorption

Pure ethanol and water vapor adsorption onto a silicalite-1 that had been prepared via the fluoride medium route and SPP was measured in collaboration with Dr. Matthias Thommes (Quantachrome) and Dr. John Bullis (Hiden Isochema). The adsorption was measured by Vstar vapor sorption analyzer (Quantachrome) and IGA-002 gas and vapor sorption analyzer (Hiden Isochema).

5.3 Results and discussion

Preparation and characterization of SPP

To study ethanol adsorption behavior it is not viable to examine MFI nanosheets since when thermal treatment occurs—a procedure carried out to remove SDA molecules from the zeolite framework—aggregates form on the nanosheets. For this reason, SPP that is a one unit cell thick MFI nanosheet along the crystallographic *b*-axis and that has a house-of-cards assembly was prepared. Nanosheet morphology can be preserved by intergrown layers after calcination. A low-magnified TEM image (**Figure 5-1A**) shows *ca.* 100 nm SPP particles that consist of intergrown nanosheets. A magnified TEM image of SPP particle (**Figure 5-1A**) reveals that the SPP particle is composed of crystalline zeolite nanosheets. As indicated in **Figure 5-1B**, the XRD pattern confirms that SPP has MFI crystallinity. The argon adsorption/desorption isotherm at 87 K (**Figure 5-1C**) shows the IUPAC isotherm Type IV; the hysteresis loop is evidence of the presence of mesoporosity. In a comparison of SPP and silicalite-1 porosity, the blue dashed line in **Figure 5-1C** indicates the argon amount that is adsorbed onto silicalite-1 synthesized in a fluoride media. The amount of argon absorbed onto the SPP at a high relative pressure regime was higher than the silicalite-1 attributed to the mesoporosity of the SPP (**Figure 5-1C**). ^{29}Si MAS NMR was analyzed to determine how much hydrophilicity stems from the silanol defects of the SPP (**Figure 5-1D**). At 103 ppm a Q^3 [Si-OH] peak appears that is associated with a hydroxyl group, that in turn is bonded to a silicon atom. In contrast to the siliclaite-1, the SPP appears to be hydrophilic and defective. The silanol groups give hydrophilicity to SPP and this increases the ability of SPP to adsorb water molecules,

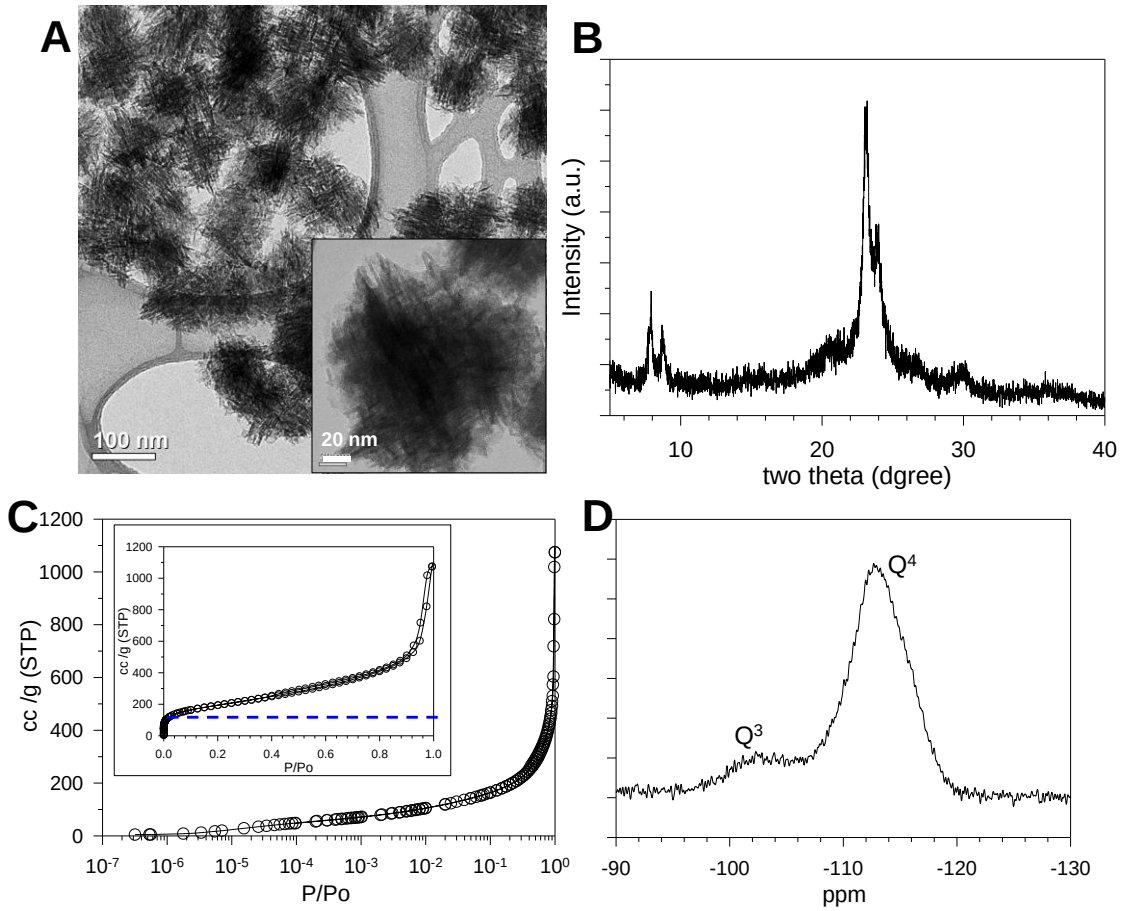

Figure 5-1. A TEM image of the as-synthesized SPP (A). The inset presents a magnified TEM image of a SPP particle. B shows an XRD pattern of the SPP and C presents the argon adsorption/desorption isotherm at 87 K of the SPP. The blue dashed line indicates the adsorbed argon amount of the silicalite-1 that was prepared via a fluoride media. ^{29}Si MAS NMR of the SPP (D). In D, Q^4 represents SiO_2 bonds that lack a silanol group [Si-OH] while Q^3 indicates a hydroxyl group that is bonded to a silicon atom.

which are hydrophilic. SPP is in pure silica form, which is neutrally charged. (However, with the hydrophilicity, the SPP preferentially adsorbs polar molecules such as water.)

Preparation of silicalite-1 via a fluoride medium route

In **Figure 5-2A**, a SEM image describes *ca.* 50 μm of coffin-shaped silicalite-1 crystals. In general, the crystals synthesized under a fluoride media are larger than those of siliclaite-1 that has been prepared via a hydroxide medium route.[18] The XRD pattern

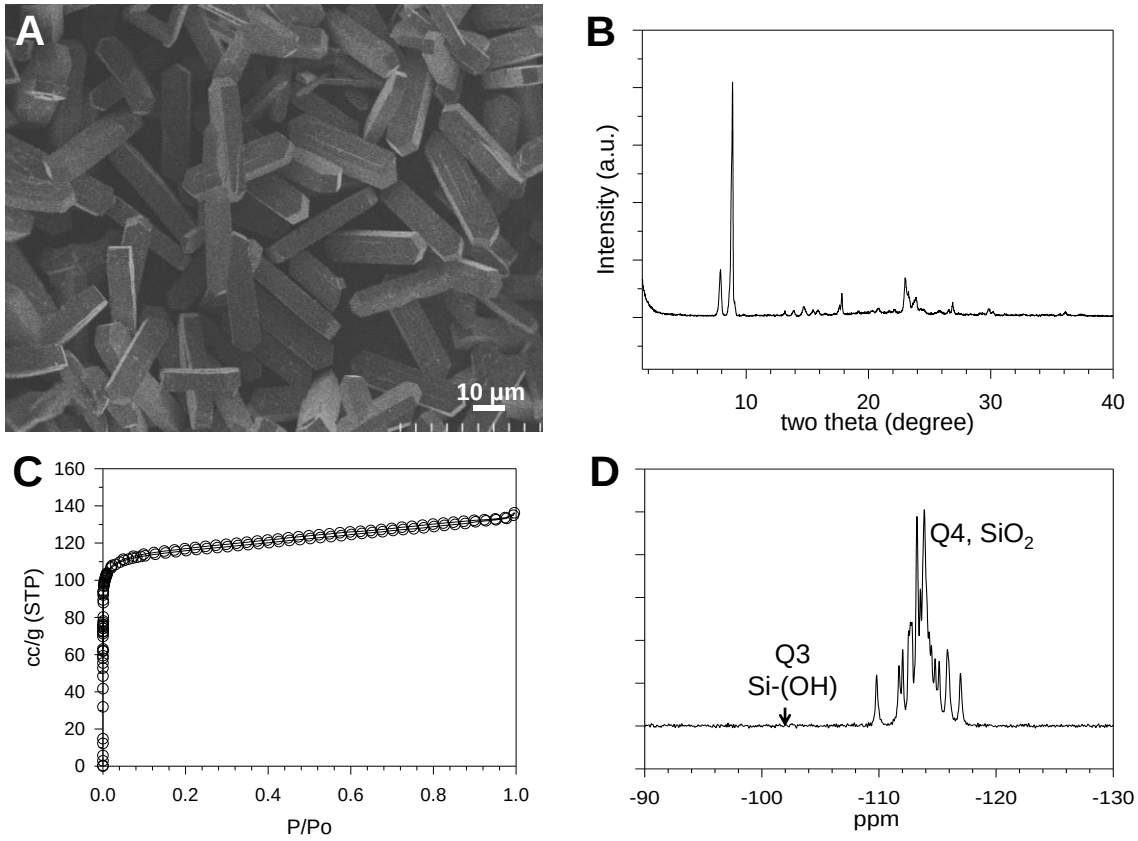

Figure 5-2. A SEM image of silicalite-1 (A) and a XRD pattern of the silicalite-1 (B). Argon adsorption/desorption isotherm at 87 K of the silicalite-1 (C). ^{29}Si MAS NMR of the silicalite-1 (D). Q^4 in D represents SiO_2 bonds without any silanol group [Si-OH] and Q^3 in D indicates a hydroxyl group is bonded to a silicon atom.

(**Figure 5-2B**) confirms that the silicalite-1 has MFI crystallinity. The argon adsorption/desorption at 87 K (**Figure 5-2C**) illustrates IUPAC isotherm Type I where the adsorbed amount is saturated. This indicates microporous adsorbents. The saturated argon adsorption indicates that the silicalite-1 does not have mesoporosity. Q^4 [Si-$(OSi)_4$] peaks at ~113 and ~115 ppm in a ^{29}Si MAS NMR spectrum, as shown in **Figure 5-2D** indicate that the synthesized silicalite-1 produced under the fluoride medium route is composed of SiO_2 tetrahedral bonds when Q^3 [Si-OH] peaks at -102 ppm are absent—a condition that is associated with hydrophilicity. In other words, the silicalite-1 prepared

via a fluoride medium route is hydrophobic/defect-free, and hence it preferentially adsorbs ethanol rather than water.

Comparison of pure ethanol and pure water vapor adsorption

Figure 5-3A shows pure ethanol vapor and water vapor adsorption onto SPP. The measurements, conducted by Dr. Matthias Thommes (Quantachrome) and Dr. John Bullis (Hiden Isochema), agree with one another (**Figure 5-3A**). As expected, water vapor adsorption onto SPP was not negligible compared to ethanol vapor adsorption associated with less hydrophobicity (**Figure 5-3A**). At a relative pressure higher than 0.8, where adsorption amount indicates mesoporosity, the amount of water adsorption onto SPP exceeds ethanol adsorption. This can be attributed to the hydrophilicity of external surface of SPP—i.e., the hydroxyl terminal groups at the external surface of SPP, which are elements of SPP mesopores.

Figure 5-3B shows pure ethanol vapor and water vapor adsorption onto the silicalite-1 prepared under a fluoride medium route. The adsorption isotherms of each component, which were obtained from Dr. Matthias Thommes (Quantachrome) and Dr. John Bullis (Hiden Isochema), agree with one another. Moreover, the pure ethanol vapor adsorption is consistent with results obtained by the Koros' group[11] and with a simulation study carried out by the Tsapatsis' group.[116] In contrast to SPP, the hydrophobicity of the silicalite-1 prepared under the fluoride medium route leads to negligible water vapor adsorption (compare it to the ethanol adsorption displayed in **Figure 5-3B)**. The tendency of ethanol adsorbed onto SPP and silicalite-1 is consistent with the argon adsorption/desorption isotherm: the amount of ethanol adsorbed onto silicalite-1 is

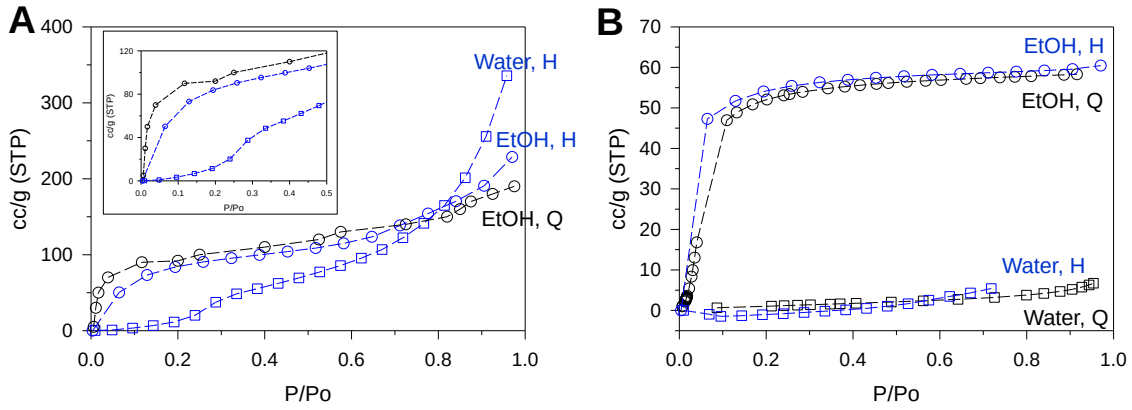

Figure 5-3. Pure ethanol and water vapor adsorption onto SPP (A) and silicalite-1 (B). An inset of A is the adsorption isotherm in the low pressure regime. Dashed lines guide the eyes. The measurements conducted by Dr. Matthias Thommes (Quantachrome) are denoted as Q. The measurements carried out by Dr. John Bullis (Hiden Isochema) are referred to as H. Dr. Limin Ren prepared the SPP for vapor adsorption.

saturated (**Figure 5-3**) but the amount of ethanol adsorbed onto SPP is not (**Figure 5-3A).** This reveals a higher absorption of ethanol, which in turn indicates SPP mesoporosity.

Figure 5-4A compares ethanol adsorption in the aqueous phase onto the SPP and the silicalite-1. The aqueous phase ethanol adsorption behavior resembles vapor phase adsorption. The amount of ethanol adsorbed onto the SPP drastically increased at a high concentration regime. This increase can be attributed to mesoporosity while the amount of ethanol adsorbed onto the silicalite-1 tends to be saturated (**Figure 5-4A**). A lower amount of ethanol was absorbed onto the SPP than onto the silicalite-1 in the low concentration regime can be attributed to the lower microporosity per unit volume of the SPP, which introduces mesopores to the crystal architecture. Recently Tsapatsis' group computationally identified the sequence of adsorption onto the SPP: the micropores fill first and then there is adsorption in the mesopores[121]. Therefore, an intersecting crossover

of an adsorbed amount of ethanol would occur[121]. Where water is present, and in contrast to hydrophobic silicalite-1, the hydrophilicity of the SPP might suppress ethanol adsorption.

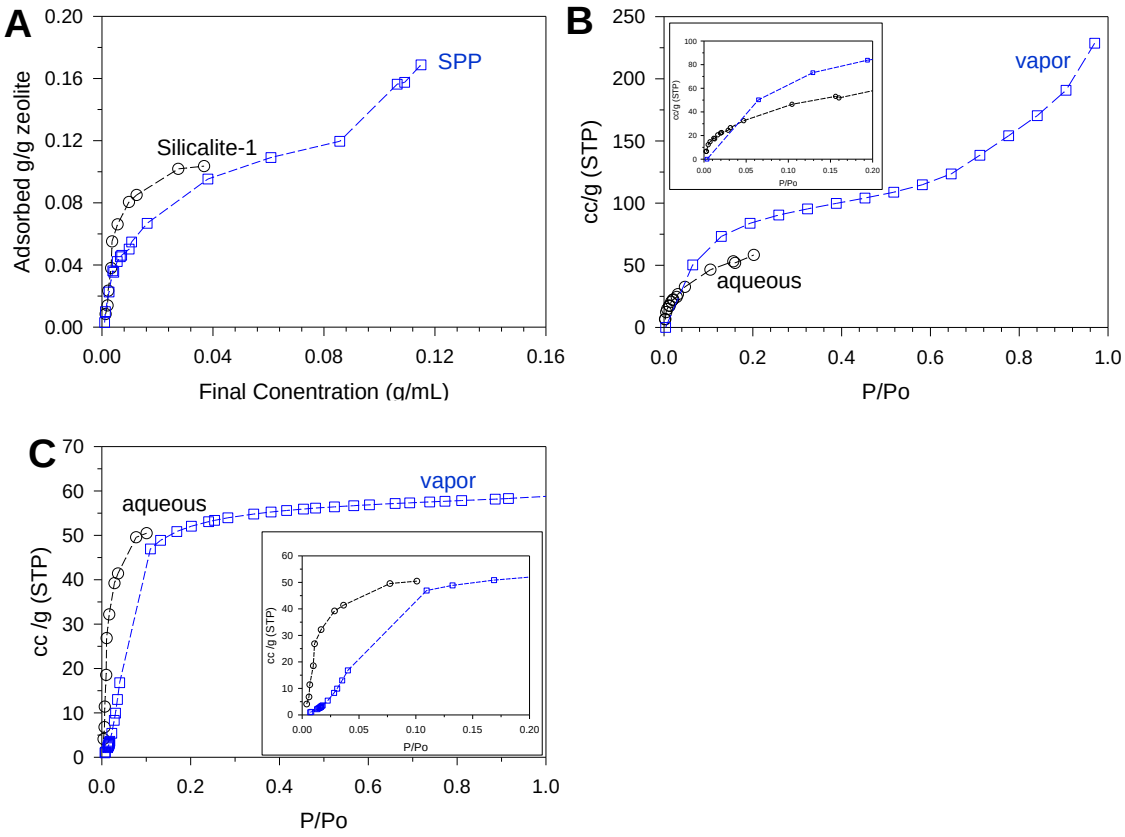

Figure 5-4. Comparison of ethanol adsorption in aqueous phase onto SPP and silicatlie-1 (A). Comparison ethanol adsorption onto the SPP in the aqueous phase and the vapor phase (B). Comparison of ethanol adsorption onto the silicalite-1 in the aqueous phase and the vapor phase (C). Insets in B and C depict adsorption isotherm at the low pressure region. Dashed lines guide the eye. The vapor phase measurements conducted by Dr. Matthias Thommes (Quantachrome) are denoted as Q. The vapor phase measurements carried out by Dr. John Bullis (Hiden Isochema) are referred to as H. Dr. Limin Ren prepared the SPP for the vapor phase adsorption.

To compare the adsorption isotherm of ethanol in the aqueous phase and the vapor phase

adsorption isotherm (**Figure 5-4B** and **C**), the ethanol concentration was converted into corresponding vapor pressure by assuming an ideal vapor/nonideal solution equilibrium. In the case of hydrophilic and defective SPP (in **Figure 5-4B**), at the very low vapor pressure regime—that is, at a relative pressure below 0.01, pure water vapor adsorption onto SPP is negligible compared to pure ethanol vapor adsorption, as presented in **Figure 5-3A**—ethanol adsorption onto SPP was promoted in the presence of water. The postulation of both the promotion of ethanol adsorption in the presence of water and the case of the silicalite-1 is discussed in the last section of this chapter. However, at relative pressures higher than 0.01, water suppresses ethanol adsorption on SPP by a factor of 2 (**Figure 5-4B**). Perhaps ethanol adsorption is constrained in the presence of water since preferential water adsorption becomes pronounced on the external surfaces of SPP and when it interacts with silanol groups within the zeolite framework. It appears that MFI crystals that have the nanosheet morphology cannot be used to separate ethanol efficiently from an aqueous ethanol solution due to hydrophilic silanol groups at the external surface and in the zeolite framework.

As **Figure 5-4C** indicates, defect-free hydrophobic siliclaite-1 shows ethanol adsorption that is the opposite of SPP. Ethanol adsorption in the aqueous phase was compared with in the vapor phase (**Figure 5-4C**). In research that simulates methanol and ethanol adsorption on pure silica type zeolites such as DDR,[119,124] FAU,[119] and MFI[125], adsorption improves when water is present. Additionally, Tsapatsis' group[122] has experimentally demonstrated that the adsorption of propylene glycol onto defect-free and hydrophobic silicalite-1 (synthesized using the fluoride medium) is promoted by the

presence of water. Using a configurational bias Monte Carlo (CMBC) simulation, Krishna's group found that interactions between water and alcohol molecules that lead to the formation of hydrogen bonds play a significant role in adsorption. Ethanol-water interactions are the most frequent, ethanol-ethanol interactions are the second most frequent, and water-water interactions are the least frequent. [119] These experimental results and computational findings suggest that enhanced ethanol absorption in the presence of water is associated with an increase in the number of adsorption sites, which in turn can be attributed to hydrogen bond formation between ethanol and water within the zeolite framework.

5.4 Conclusion

From a defective and hydrophilic SPP—i.e., intergrown MFI nanosheets having a house-of-card architecture—it was determined that water vapor adsorption is comparable to ethanol vapor adsorption. At a relative pressure higher than 0.8, whereupon adsorbed amount indicates filling of the SPP mesoporosity, water vapor adsorption preferentially takes place due to the presence of silanol terminal groups on the external surface of the SPP. These terminal groups are elements of the SPP mesopores. In contrast, defect-free and hydrophobic silicalite-1 synthesized using a fluoride medium facilitates the preferential adsorption of ethanol vapor over water vapor.

To probe how water affects ethanol adsorption onto the defective SPP and the defect-free silicalite-1 adsorption in aqueous phase was compared to vapor phase adsorption. Compared to pure ethanol vapor adsorption, ethanol adsorption onto defect-free silicalite-

1 is enhanced at the low relative pressure regime in the presence of water (the aqueous phase). At medium to high relative pressure regimes water suppresses ethanol adsorption onto the SPP. The number of adsorption sites decreases because of the competitive adsorption of water onto defective and hydrophilic SPP. In contrast, ethanol adsorption was promoted onto SPP at low relative pressure regime and onto silicalite-1 in the presence water. This may be attributed to increases in number of adsorption sites that stem from hydrogen bond formation between ethanol and water molecules within zeolite framework. On the basis of the results described in this chapter, fist, defect-free and hydrophobic MFI is a better candidate for preferential ethanol selective separation than water. Second, defective and hydrophilic MFI crystals that have a nanosheet morphology do not effectively separate ethanol from an aqueous ethanol solution.

Chapter 6: Concluding remarks

This dissertation describes direct hydrothermal synthesis of MFI nanosheets. In this first successful bottom-up strategy, MFI nanosheets are developed through seeded-growth. Under this methodology, the yield of MFI nanosheets is remarkably higher than the yield of the state-of-the-art top-down approach. This simple method, when combined with gel-free secondary growth, is an attractive alternative to current energy-intensive industrial separation processes such as distillation.

Under bottom-up synthesis MFI nanosheets can be combined with polymers to create zeolite/polymer mixed matrix membranes and zeolite membranes on polymeric supports, but this would be possible only if the MFI nanosheets are SDA-free and without aggregates. This possibility is intriguing. Although the zeolite membranes have a high flux and separation factor due to the uniform micropore structure, industry has not adopted them at a significant scale due to the high cost. Hoping to reduce the cost of zeolite membrane manufacture, researchers for the last three decades have investigated processes that involve polymeric materials.

This dissertation suggests that it should be possible to prepare de-templated MFI nanosheets through chemical oxidation. These nanosheets can then be applied as selective fillers on zeolite/polymer matrix membranes or membranes on polymeric supports. With regards to zeolite/polymer matrix membranes, a number of studies have examined conventional MFI crystals. Cussler[122] theoretically predicted that plate-like selective fillers would enhance membrane performance, but to the best knowledge no one has experimentally validated this suggestion. The main challenge has been how to prepare

de-templated zeolite nanosheets so that aggregates do not form. To evaluate Cussler's model experimentally the SDA-removed MFI nanosheets can be applied as plate-like selective fillers in zeolite/polymer mixed-matrix membranes. This dissertation poses possibility to achieve the evaluation of Cussler's model with partially de-templated MFI nanosheets, which do not form aggregates, via chemical oxidation.

Time-resolved study of the sequential evolution of seeds improves understanding of the zeolite crystallization mechanism. However, further investigations are required to reveal why 5 nm nanosheets form. Perhaps the seeded-growth methodology used to prepare MFI nanosheets can be applied to acquire nanosheet crystals in other zeolite frameworks. The surfaces of the MFI nanosheets discussed in this dissertation have well-defined facets that were preserved after synthesis. Studying the influence of surface properties on the adsorption behavior of MFI nanosheets is of importance since external surfaces play an important role in nano-sized crystals. Moreover, tracking each facet or each crystallographic axis during secondary growth in order to probe their crystal growth rates is easy. In the case of thin MFI membranes, the crystal growth rate along *b*-axis should be suppressed while the crystal growth rate along *a*- and *c*-axis should be promoted. This practice should help to find the optimal condition of secondary growth for membranes.

In addition to their usefulness for separation, the MFI nanosheets prepared under the bottom-up strategy can serve as catalysts. It is demonstrated that aluminum and tin atoms can be incorporated into the MFI zeolite framework. The pilot experiment raises the possibility that the method could have catalysis applications.

This dissertation suggests that siliceous zeolites can preferentially adsorb ethanol over water due to high affinity to ethanol than water. However, when the siliceous zeolites have nanosheet morphology, they cannot preferentially adsorb ethanol over water at the same rate as siliceous zeolites synthesized through the fluoride medium route. This is attributed to the presence of silanol groups on the external surface of the siliceous zeolite nanosheets and on the zeolite framework. Since the external surface significantly affects the adsorption properties of the zeolite nanosheets, the silanol groups, which are hydrophilic, are detrimental to ethanol adsorption. Moreover, despite neutral charge of the framework, silanol defects are created in the zeolite framework when the siliceous zeolites are synthesized through the base medium route. In the zeolite framework, siliceous zeolites produced via a fluoride medium route do not contain silanol defects thus they would preferentially adsorb ethanol over water. Synthesis through the fluoride medium route produces zeolite crystals that are larger than those typical of the hydroxide medium recipe. In other words, nanosheet morphology is difficult to obtain when fluoride is present. However, as mentioned above, zeolite nanosheets are not necessary for ethanol adsorption. To produce silanol defect-free zeolites, siliceous zeolites should be produced via a fluoride medium route. Not only MFI framework, other zeolite frameworks such as FER, DDR, CHA and BEA can be produced via a fluoride medium route. Thus, the efficiencies of ethanol adsorption onto different zeolite frameworks in silanol defect-free pure silica form can be compared one another.

Bibliography

1 Davis, M. E. Ordered porous materials for emerging applications. *Nature* **417**, 813-821, doi:10.1038/nature00785 (2002).

2 Leonowicz, M. E., Lawton, J. A., Lawton, S. L. & Rubin, M. K. MCM-22: A Molecular Sieve with Two Independent Multidimensional Channel Systems. *Science* **264**, 1910-1913, doi:10.1126/science.264.5167.1910 (1994).

3 Corma, A., Fornes, V., Pergher, S. B., Maesen, T. L. M. & Buglass, J. G. Delaminated zeolite precursors as selective acidic catalysts. *Nature* **396**, 353-356, doi:10.1038/24592 (1998).

4 Choi, M. *et al.* Stable single-unit-cell nanosheets of zeolite MFI as active and long-lived catalysts. *Nature* **461**, 246-U120, doi:10.1038/nature08288 (2009).

5 Corma, A. From microporous to mesoporous molecular sieve materials and their use in catalysis. *Chemical Reviews* **97**, 2373-2419, doi:10.1021/cr960406n (1997).

6 Bai, P. *et al.* Discovery of optimal zeolites for challenging separations and chemical transformations using predictive materials modeling. *Nature Communications* **6**, doi:10.1038/ncomms6912 (2015).

7 Elyassi, B. *et al.* Ethanol/water mixture pervaporation performance of b-oriented silicalite-1 membranes made by gel-free secondary growth. *Aiche Journal* **62**, 556-563, doi:10.1002/aic.15124 (2016).

8 Chen, H. L., Li, Y. S. & Yang, W. S. Preparation of silicalite-1 membrane by solution-filling method and its alcohol extraction properties. *Journal of Membrane Science* **296**, 122-130, doi:10.1016/j.memsci.2007.03.021 (2007).

9 Bowen, T. C., Kalipcilar, H., Falconer, J. L. & Noble, R. D. Pervaporation of organic/water mixtures through B-ZSM-5 zeolite membranes on monolith supports. *Journal of Membrane Science* **215**, 235-247, doi:10.1016/s0376-7388(02)00617-8 (2003).

10 Dose, M. E. *et al.* Effect of Crystal Size on Framework Defects and Water Uptake in Fluoride Mediated Silicalite-1. *Chemistry of Materials* **26**, 4368-4376, doi:10.1021/cm500914b (2014).

11 Zhang, K. *et al.* Adsorption of Water and Ethanol in MFI-Type Zeolites. *Langmuir* **28**, 8664-8673, doi:10.1021/la301122h (2012).

12 Cundy, C. S. & Cox, P. A. The hydrothermal synthesis of zeolites: Precursors, intermediates and reaction mechanism. *Microporous and Mesoporous Materials* **82**, 1-78, doi:10.1016/j.micromeso.2005.02.016 (2005).

13 Barrer, R. M. & Denny, P. J. 201. Hydrothermal chemistry of the silicates. Part IX. Nitrogenous aluminosilicates. *Journal of the Chemical Society (Resumed)*, 971-982, doi:10.1039/JR9610000971 (1961).

14 DeWitt, E. J., Ramp, F. L. & Trapasso, L. E. HOMOGENEOUS HYDROGENATION CATALYZED BY BORANES. *Journal of the American Chemical Society* **83**, 4672-4672, doi:10.1021/ja01483a049 (1961).

15 Kerr, G. T. & Kokotailo, G. T. SODIUM ZEOLITE ZK-4, A NEW SYNTHETIC CRYSTALLINE ALUMINOSILICATE. *Journal of the American Chemical Society* **83**, 4675-4675, doi:10.1021/ja01483a052 (1961).
16 Kerr, G. T. Chemistry of Crystalline Aluminosilicates. II. The Synthesis and Properties of Zeolite ZK-4. *Inorganic Chemistry* **5**, 1537-1539, doi:10.1021/ic50043a015 (1966).
17 Kokotailo, G. T., Lawton, S. L., Olson, D. H., Olson, D. H. & Meier, W. M. STRUCTURE OF SYNTHETIC ZEOLITE ZSM-5. *Nature* **272**, 437-438, doi:10.1038/272437a0 (1978).
18 Cundy, C. S. & Cox, P. A. The hydrothermal synthesis of zeolites: History and development from the earliest days to the present time. *Chemical Reviews* **103**, 663-701, doi:10.1021/cr020060i (2003).
19 Schoeman, B. J. Analysis of the nucleation and growth of TPA-silicalite-1 at elevated temperatures with the emphasis on colloidal stability. *Microporous and Mesoporous Materials* **22**, 9-22, doi:10.1016/s1387-1811(98)00080-8 (1998).
20 Perezpariente, J., Martens, J. A. & Jacobs, P. A. CRYSTALLIZATION MECHANISM OF ZEOLITE-BETA FROM (TEA)2O, NA2O AND K2O CONTAINING ALUMINOSILICATE GELS. *Applied Catalysis* **31**, 35-64, doi:10.1016/s0166-9834(00)80665-x (1987).
21 de Moor, P. *et al.* Imaging the assembly process of the organic-mediated synthesis of a zeolite. *Chemistry-a European Journal* **5**, 2083-2088, doi:10.1002/(sici)1521-3765(19990702)5:7<2083::aid-chem2083>3.3.co;2-6 (1999).
22 Aerts, A. *et al.* Investigation of the Mechanism of Colloidal Silicalite-1 Crystallization by Using DLS, SAXS, and Si-29 NMR Spectroscopy. *Chemistry-a European Journal* **16**, 2764-2774, doi:10.1002/chem.200901688 (2010).
23 Bosnar, S., Antonic, T., Bronic, J. & Subotic, B. Mechanism and kinetics of the growth of zeolite microcrystals. Part 2: Influence of sodium ions concentration in the liquid phase on the growth kinetics of zeolite A microcrystals. *Microporous and Mesoporous Materials* **76**, 157-165, doi:10.1016/j.micromeso.2004.07.021 (2004).
24 Mintova, S., Olson, N. H., Valtchev, V. & Bein, T. Mechanism of zeolite a nanocrystal growth from colloids at room temperature. *Science* **283**, 958-960, doi:10.1126/science.283.5404.958 (1999).
25 Fedeyko, J. M., Rimer, J. D., Lobo, R. F. & Vlachos, D. G. Spontaneous formation of silica nanoparticles in basic solutions of small tetraalkylammonium cations. *Journal of Physical Chemistry B* **108**, 12271-12275, doi:10.1021/jp047623+ (2004).
26 Falamaki, C., Edrissi, M. & Sohrabi, M. Studies on the crystallization kinetics of zeolite ZSM-5 with 1,6-hexanediol as a structure-directing agent. *Zeolites* **19**, 2-5, doi:10.1016/s0144-2449(97)00025-0 (1997).
27 Mintova, S., Petkov, N., Karaghiosoff, K. & Bein, T. Transformation of amorphous silica colloids to nanosized MEL zeolite. *Microporous and Mesoporous Materials* **50**, 121-128, doi:10.1016/s1387-1811(01)00429-2 (2001).

28 Nikolakis, V., Kokkoli, E., Tirrell, M., Tsapatsis, M. & Vlachos, D. G. Zeolite growth by addition of subcolloidal particles: Modeling and experimental validation. *Chemistry of Materials* **12**, 845-853, doi:10.1021/cm990653i (2000).
29 Cundy, C. S., Henty, M. S. & Plaisted, R. J. Zeolite synthesis using a semicontinuous reactor, Part 1: Controlled nucleation and growth of ZSM-5 crystals having well-defined morphologies. *Zeolites* **15**, 353-372, doi:http://dx.doi.org/10.1016/0144-2449(94)00052-T (1995).
30 Davis, T. M. *et al.* Mechanistic principles of nanoparticle evolution to zeolite crystals. *Nature Materials* **5**, 400-408, doi:10.1038/nmat1636 (2006).
31 Kumar, S., Davis, T. M., Ramanan, H., Penn, R. L. & Tsapatsis, M. Aggregative growth of silicalite-1. *Journal of Physical Chemistry B* **111**, 3398-3403, doi:10.1021/jp0677445 (2007).
32 Kumar, S., Wang, Z., Penn, R. L. & Tsapatsis, M. A Structural Resolution Cryo-TEM Study of the Early Stages of MFI Growth. *Journal of the American Chemical Society* **130**, 17284-+, doi:10.1021/ja8063167 (2008).
33 Kumar, S., Penn, R. L. & Tsapatsis, M. On the nucleation and crystallization of silicalite-1 from a dilute clear sol. *Microporous and Mesoporous Materials* **144**, 74-81, doi:10.1016/j.micromeso.2011.02.029 (2011).
34 International Zeolite Association, http://www.iza-online.org/.
35 Snyder, M. A. & Tsapatsis, M. Hierarchical nanomanufacturing: From shaped zeolite nanoparticles to high-performance separation membranes. *Angewandte Chemie-International Edition* **46**, 7560-7573, doi:10.1002/anie.200604910 (2007).
36 Bowen, T. C., Noble, R. D. & Falconer, J. L. Fundamentals and applications of pervaporation through zeolite membranes. *Journal of Membrane Science* **245**, 1-33, doi:10.1016/j.memsci.2004.06.059 (2004).
37 Diaz, I., Kokkoli, E., Terasaki, O. & Tsapatsis, M. Surface structure of zeolite (MFI) crystals. *Chemistry of Materials* **16**, 5226-5232, doi:10.1021/cm0488534 (2004).
38 Bein, T. Synthesis and applications of molecular sieve layers and membranes. *Chemistry of Materials* **8**, 1636-1653, doi:10.1021/cm960148a (1996).
39 Sano, T. *et al.* PREPARATION AND CHARACTERIZATION OF ZSM-5 ZEOLITE FILM. *Zeolites* **11**, 842-845, doi:10.1016/s0144-2449(05)80066-1 (1991).
40 Geus, E. R., Vanbekkum, H., Bakker, W. J. W. & Moulijn, J. A. HIGH-TEMPERATURE STAINLESS-STEEL SUPPORTED ZEOLITE (MFI) MEMBRANES - PREPARATION, MODULE CONSTRUCTION, AND PERMEATION EXPERIMENTS. *Microporous Materials* **1**, 131-147, doi:10.1016/0927-6513(93)80019-q (1993).
41 Bai, C. S., Jia, M. D., Falconer, J. L. & Noble, R. D. PREPARATION AND SEPARATION PROPERTIES OF SILICALITE COMPOSITE MEMBRANES. *Journal of Membrane Science* **105**, 79-87, doi:10.1016/0376-7388(95)00049-i (1995).

42 Yan, Y. S., Davis, M. E. & Gavalas, G. R. PREPARATION OF ZEOLITE ZSM-5 MEMBRANES BY IN-SITU CRYSTALLIZATION ON POROUS ALPHA-AL2O3. *Industrial & Engineering Chemistry Research* **34**, 1652-1661, doi:10.1021/ie00044a018 (1995).
43 Vroon, Z., Keizer, K., Burggraaf, A. J. & Verweij, H. Preparation and characterization of thin zeolite MFI membranes on porous supports. *Journal of Membrane Science* **144**, 65-76, doi:10.1016/s0376-7388(98)00035-0 (1998).
44 Boudreau, L. C. & Tsapatsis, M. A highly oriented thin film of zeolite A. *Chemistry of Materials* **9**, 1705-&, doi:10.1021/cm970151+ (1997).
45 Gouzinis, A. & Tsapatsis, M. On the preferred orientation and microstructural manipulation of molecular sieve films prepared by secondary growth. *Chemistry of Materials* **10**, 2497-2504, doi:10.1021/cm9802402 (1998).
46 Yan, Y., Tsapatsis, M., Gavalas, G. R. & Davis, M. E. Zeolite ZSM-5 membranes grown on porous [small alpha]-Al2O3. *Journal of the Chemical Society, Chemical Communications*, 227-228, doi:10.1039/C39950000227 (1995).
47 Jia, M. D., Peinemann, K. V. & Behling, R. D. CERAMIC ZEOLITE COMPOSITE MEMBRANES - PREPARATION, CHARACTERIZATION AND GAS PERMEATION. *Journal of Membrane Science* **82**, 15-26, doi:10.1016/0376-7388(93)85089-f (1993).
48 Chen, H. L., Song, C. S. & Yang, W. S. Effects of aging on the synthesis and performance of silicalite membranes on silica tubes without seeding. *Microporous and Mesoporous Materials* **102**, 249-257, doi:10.1016/j.micromeso.2006.12.043 (2007).
49 Caro, J. & Noack, M. Zeolite membranes - Recent developments and progress. *Microporous and Mesoporous Materials* **115**, 215-233, doi:10.1016/j.micromeso.2008.03.008 (2008).
50 Tung Cao Thanh, P., Kim, H. S. & Yoon, K. B. Growth of Uniformly Oriented Silica MFI and BEA Zeolite Films on Substrates. *Science* **334**, 1533-1538, doi:10.1126/science.1212472 (2011).
51 Tung Cao Thanh, P., Thanh Huu, N. & Yoon, K. B. Gel-Free Secondary Growth of Uniformly Oriented Silica MFI Zeolite Films and Application for Xylene Separation. *Angewandte Chemie-International Edition* **52**, 8693-8698, doi:10.1002/anie.201301766 (2013).
52 Choi, J., Ghosh, S., King, L. & Tsapatsis, M. MFI zeolite membranes from a- and randomly oriented monolayers. *Adsorption* **12**, 339-360, doi:10.1007/s10450-006-0564-y (2006).
53 Varoon, K. *et al.* Dispersible Exfoliated Zeolite Nanosheets and Their Application as a Selective Membrane. *Science* **334**, 72-75, doi:10.1126/science.1208891 (2011).
54 Agrawal, K. V. *et al.* Solution-processable exfoliated zeolite nanosheets purified by density gradient centrifugation. *Aiche Journal* **59**, 3458-3467, doi:10.1002/aic.14099 (2013).

55 Agrawal, K. V. *et al.* Oriented MFI Membranes by Gel-Less Secondary Growth of Sub-100 nm MFI-Nanosheet Seed Layers. *Advanced Materials* **27**, 3243-3249, doi:10.1002/adma.201405893 (2015).
56 Lai, Z. P., Tsapatsis, M. & Nicolich, J. R. Siliceous ZSM-5 membranes by secondary growth of b-oriented seed layers. *Advanced Functional Materials* **14**, 716-729, doi:10.1002/adfm.200400040 (2004).
57 Lee, P.-S. *et al.* Sub-40 nm Zeolite Suspensions via Disassembly of Three-Dimensionally Ordered Mesoporous-Imprinted Silicalite-1. *Journal of the American Chemical Society* **133**, 493-502, doi:10.1021/ja107942n (2011).
58 Snyder, M. A. & Tsapatsis, M. Hierarchical nanomanufacturing: From shaped zeolite nanoparticles to high-performance separation membranes. *Angewandte Chemie-International Edition* **46**, 7560-7573, doi:10.1002/anie.200604910 (2007).
59 Tsapatsis, M. Toward High-Throughput Zeolite Membranes. *Science* **334**, 767-768, doi:10.1126/science.1205957 (2011).
60 Tosheva, L. & Valtchev, V. P. Nanozeolites: Synthesis, crystallization mechanism, and applications. *Chemistry of Materials* **17**, 2494-2513, doi:10.1021/cm047908z (2005).
61 Chen, H. *et al.* Hydrothermal Synthesis of Zeolites with Three-Dimensionally Ordered Mesoporous-Imprinted Structure. *Journal of the American Chemical Society* **133**, 12390-12393, doi:10.1021/ja2046815 (2011).
62 Corma, A., Fornes, V., Martinez-Triguero, J. & Pergher, S. B. Delaminated zeolites: Combining the benefits of zeolites and mesoporous materials for catalytic uses. *Journal of Catalysis* **186**, 57-63, doi:10.1006/jcat.1999.2503 (1999).
63 Maheshwari, S. *et al.* Layer structure preservation during swelling, pillaring, and exfoliation of a zeolite precursor. *Journal of the American Chemical Society* **130**, 1507-1516, doi:10.1021/ja077711i (2008).
64 Ogino, I. *et al.* Delamination of Layered Zeolite Precursors under Mild Conditions: Synthesis of UCB-1 via Fluoride/Chloride Anion-Promoted Exfoliation. *Journal of the American Chemical Society* **133**, 3288-3291, doi:10.1021/ja111147z (2011).
65 Eilertsen, E. A. *et al.* Nonaqueous Fluoride/Chloride Anion-Promoted Delamination of Layered Zeolite Precursors: Synthesis and Characterization of UCB-2. *Chemistry of Materials* **23**, 5404-5408, doi:10.1021/cm202364q (2011).
66 Rangnekar, N. *et al.* 2D Zeolite Coatings: Langmuir–Schaefer Deposition of 3 nm Thick MFI Zeolite Nanosheets. *Angewandte Chemie* **127**, 6671-6675, doi:10.1002/ange.201411791 (2015).
67 Melian-Cabrera, I., Kapteijn, F. & Moulijn, J. A. Room temperature detemplation of zeolites through H2O2-mediated oxidation. *Chemical Communications*, 2744-2746, doi:10.1039/b502167g (2005).
68 Ortiz-Iniesta, M. J. & Melian-Cabrera, I. Fenton chemistry-based detemplation of an industrially relevant microcrystalline beta zeolite. Optimization and scaling-up

studies. *Microporous and Mesoporous Materials* **206**, 58-66, doi:10.1016/j.micromeso.2014.12.019 (2015).
69 Huang, H. J., Ramaswamy, S., Tschirner, U. W. & Ramarao, B. V. A review of separation technologies in current and future biorefineries. *Separation and Purification Technology* **62**, 1-21, doi:10.1016/j.seppur.2007.12.011 (2008).
70 Bonilla, G. *et al.* Zeolite (MFI) crystal morphology control using organic structure-directing agents. *Chemistry of Materials* **16**, 5697-5705, doi:10.1021/cm048854w (2004).
71 Chaikittisilp, W. *et al.* Formation of Hierarchically Organized Zeolites by Sequential Intergrowth. *Angewandte Chemie-International Edition* **52**, 3355-3359, doi:10.1002/anie.201209638 (2013).
72 Zhang, X. *et al.* Synthesis of Self-Pillared Zeolite Nanosheets by Repetitive Branching. *Science* **336**, 1684-1687, doi:10.1126/science.1221111 (2012).
73 Burchart, E. D., Jansen, J. C., Vandegraaf, B. & Vanbekkum, H. MOLECULAR MECHANICS STUDIES ON MFI-TYPE ZEOLITES .4. ENERGETICS OF CRYSTAL-GROWTH DIRECTING AGENTS. *Zeolites* **13**, 216-221 (1993).
74 Wong, W. C., Au, L. T. Y., Ariso, C. T. & Yeung, K. L. Effects of synthesis parameters on the zeolite membrane growth. *Journal of Membrane Science* **191**, 143-163, doi:10.1016/s0376-7388(01)00453-7 (2001).
75 Gabelica, Z., Blom, N. & Derouane, E. G. SYNTHESIS AND CHARACTERIZATION OF ZSM-5 TYPE ZEOLITES .3. A CRITICAL-EVALUATION OF THE ROLE OF ALKALI AND AMMONIUM CATIONS. *Applied Catalysis* **5**, 227-248, doi:10.1016/0166-9834(83)80135-3 (1983).
76 Egeblad, K., Christensen, C. H., Kustova, M. & Christensen, C. H. Templating mesoporous zeolites. *Chemistry of Materials* **20**, 946-960, doi:10.1021/cm702224p (2008).
77 Tao, Y. S., Kanoh, H., Abrams, L. & Kaneko, K. Mesopore-modified zeolites: Preparation, characterization, and applications. *Chemical Reviews* **106**, 896-910, doi:10.1021/cr040204o (2006).
78 Stoeger, J. A., Choi, J. & Tsapatsis, M. Rapid thermal processing and separation performance of columnar MFI membranes on porous stainless steel tubes. *Energy & Environmental Science* **4**, 3479-3486, doi:10.1039/c1ee01700d (2011).
79 Lai, Z. P. *et al.* Microstructural optimization of a zeolite membrane for organic vapor separation. *Science* **300**, 456-460, doi:10.1126/science.1082169 (2003).
80 Choi, J. *et al.* Grain Boundary Defect Elimination in a Zeolite Membrane by Rapid Thermal Processing. *Science* **325**, 590-593, doi:10.1126/science.1176095 (2009).
81 Coronas, J., Falconer, J. L. & Noble, R. D. Characterization and permeation properties of ZSM-5 tubular membranes. *Aiche Journal* **43**, 1797-1812, doi:10.1002/aic.690430715 (1997).
82 Xomeritakis, G., Nair, S. & Tsapatsis, M. Transport properties of alumina-supported MFI membranes made by secondary (seeded) growth. *Microporous and Mesoporous Materials* **38**, 61-73, doi:10.1016/s1387-1811(99)00300-5 (2000).

83 Kondo, M., Komori, M., Kita, H. & Okamoto, K. Tubular-type pervaporation module with zeolite NaA membrane. *Journal of Membrane Science* **133**, 133-141, doi:10.1016/s0376-7388(97)00087-2 (1997).
84 Korelskiy, D. *et al.* High flux MFI membranes for pervaporation. *Journal of Membrane Science* **427**, 381-389, doi:10.1016/j.memsci.2012.10.016 (2013).
85 Global Paraxylene Market by Application.
86 O'Neil, K. & Wantanachaisaeng, P. Capturing Opportunities for Para-xylene Production. (2007).
87 http://www.transparencymarketresearch.com/butane-market.html.
88 Coronas, J., Noble, R. D. & Falconer, J. L. Separations of C-4 and C-6 isomers in ZSM-5 tubular membranes. *Industrial & Engineering Chemistry Research* **37**, 166-176, doi:10.1021/ie970462u (1998).
89 Tuan, V. A., Falconer, J. L. & Noble, R. D. Alkali-free ZSM-5 membranes: Preparation conditions and separation performance. *Industrial & Engineering Chemistry Research* **38**, 3635-3646, doi:10.1021/ie980808g (1999).
90 Dong, J. H., Lin, Y. S., Hu, M. Z. C., Peascoe, R. A. & Payzant, E. A. Template-removal-associated microstructural development of porous-ceramic-supported MFI zeolite membranes. *Microporous and Mesoporous Materials* **34**, 241-253, doi:10.1016/s1387-1811(99)00175-4 (2000).
91 Liu, Y., Li, Y. & Yang, W. Fabrication of Highly b-Oriented MFI Film with Molecular Sieving Properties by Controlled In-Plane Secondary Growth. *Journal of the American Chemical Society* **132**, 1768-+, doi:10.1021/ja909888v (2010).
92 Chaikittisilp, W., Davis, M. E. & Okubo, T. TPA(+) - Mediated conversion of silicon wafer into preferentially-oriented MFI zeolite film under steaming. *Chemistry of Materials* **19**, 4120-+, doi:10.1021/cm071475t (2007).
93 denExter, M. J. *et al.* Stability of oriented silicalite-1 films in view of zeolite membrane preparation. *Zeolites* **19**, 13-20, doi:10.1016/s0144-2449(97)00044-4 (1997).
94 Na, K. *et al.* Pillared MFI Zeolite Nanosheets of a Single-Unit-Cell Thickness. *Journal of the American Chemical Society* **132**, 4169-4177, doi:10.1021/ja908382n (2010).
95 Iler, R. K. The Chemistry of Silica: Solubility, Polymerization, Colloid and Surface Properties and Biochemistry of Silica.
96 Geus, E. R., Jansen, J. C. & Vanbekkum, H. CALCINATION OF LARGE MFI-TYPE SINGLE-CRYSTALS .1. EVIDENCE FOR THE OCCURRENCE OF CONSECUTIVE GROWTH FORMS AND POSSIBLE DIFFUSION-BARRIERS ARISING THEREOF. *Zeolites* **14**, 82-88, doi:10.1016/0144-2449(94)90001-9 (1994).
97 Wang, H. T., Wang, Z. B. & Yan, Y. S. Colloidal suspensions of template-removed zeolite nanocrystals. *Chemical Communications*, 2333-2334, doi:10.1039/b006518h (2000).
98 Rangnekar, N., Mittal, N., Elyassi, B., Caro, J. & Tsapatsis, M. Zeolite membranes - a review and comparison with MOFs. *Chemical Society Reviews* **44**, 7128-7154, doi:10.1039/c5cs00292c (2015).

99 Vane, L. M., Namboodiri, V. V. & Bowen, T. C. Hydrophobic zeolite-silicone rubber mixed matrix membranes for ethanol-water separation: Effect of zeolite and silicone component selection on pervaporation performance. *Journal of Membrane Science* **308**, 230-241, doi:10.1016/j.memsci.2007.10.003 (2008).

100 Okumus, E., Gurkan, T. & Yilmaz, L. DEVELOPMENT OF A MIXED-MATRIX MEMBRANE FOR PERVAPORATION. *Separation Science and Technology* **29**, 2451-2473, doi:10.1080/01496399408002203 (1994).

101 Kujawski, W. & Roszak, R. Pervaporative removal of volatile organic compounds from multicomponent aqueous mixtures. *Separation Science and Technology* **37**, 3559-3575, doi:10.1081/ss-120014443 (2002).

102 Vankelecom, I. F. J., Scheppers, E., Heus, R. & Uytterhoeven, J. B. PARAMETERS INFLUENCING ZEOLITE INCORPORATION IN PDMS MEMBRANES. *Journal of Physical Chemistry* **98**, 12390-12396, doi:10.1021/j100098a038 (1994).

103 Tehennepe, H. J. C., Bargeman, D., Mulder, M. H. V. & Smolders, C. A. ZEOLITE-FILLED SILICONE-RUBBER MEMBRANES .1. MEMBRANE PREPARATION AND PERVAPORATION RESULTS. *Journal of Membrane Science* **35**, 39-55, doi:10.1016/s0376-7388(00)80921-7 (1987).

104 Chen, X., Ping, Z. H. & Long, Y. C. Separation properties of alcohol-water mixture through silicalite-I-filled silicone rubber membranes by pervaporation. *Journal of Applied Polymer Science* **67**, 629-636, doi:10.1002/(sici)1097-4628(19980124)67:4<629::aid-app5>3.0.co;2-4 (1998).

105 Yang, H., Nguyen, Q. T., Ping, Z., Long, Y. & Hirata, Y. Desorption and pervaporation properties of zeolite-filled Poly(dimethylsiloxane) membranes. *Materials Research Innovations* **5**, 101-106, doi:10.1007/s100190100138 (2001).

106 Adnadjevic, B., Jovanovic, J. & Gajinov, S. Effect of different physicochemical properties of hydrophobic zeolites on the pervaporation properties of PDMS-membranes. *Journal of Membrane Science* **136**, 173-179, doi:10.1016/s0376-7388(97)00161-0 (1997).

107 Jia, M. D., Peinemann, K. V. & Behling, R. D. PREPARATION AND CHARACTERIZATION OF THIN-FILM ZEOLITE PDMS COMPOSITE MEMBRANES. *Journal of Membrane Science* **73**, 119-128, doi:10.1016/0376-7388(92)80122-z (1992).

108 Bartelscaspers, C., Tusellanger, E. & Lichtenthaler, R. N. SORPTION ISOTHERMS OF ALCOHOLS IN ZEOLITE-FILLED SILICONE-RUBBER AND IN PVA-COMPOSITE MEMBRANES. *Journal of Membrane Science* **70**, 75-83, doi:10.1016/0376-7388(92)80081-t (1992).

109 Vane, L. M., Namboodiri, V. V. & Meier, R. G. Factors affecting alcohol-water pervaporation performance of hydrophobic zeolite-silicone rubber mixed matrix membranes. *Journal of Membrane Science* **364**, 102-110, doi:10.1016/j.memsci.2010.08.006 (2010).

110 Ge, Q., Wang, Z. & Yan, Y. High-Performance Zeolite NaA Membranes on Polymer-Zeolite Composite Hollow Fiber Supports. *Journal of the American Chemical Society* **131**, 17056-+, doi:10.1021/ja9082057 (2009).

111 Xiao, F. S. *et al.* Catalytic properties of hierarchical mesoporous zeolites templated with a mixture of small organic ammonium salts and mesoscale cationic polymers. *Angewandte Chemie-International Edition* **45**, 3090-3093, doi:10.1002/anie.200600241 (2006).
112 Mallon, E. E., Bhan, A. & Tsapatsis, M. Driving Forces for Adsorption of Polyols onto Zeolites from Aqueous Solutions. *Journal of Physical Chemistry B* **114**, 1939-1945, doi:10.1021/jp910543r (2010).
113 Mallon, E. E. *et al.* Correlations for Adsorption of Oxygenates onto Zeolites from Aqueous Solutions. *Journal of Physical Chemistry B* **115**, 11431-11438, doi:10.1021/jp208143t (2011).
114 Vane, L. M. A review of pervaporation for product recovery from biomass fermentation processes. *Journal of Chemical Technology and Biotechnology* **80**, 603-629, doi:10.1002/jctb.1265 (2005).
115 Lin, X., Chen, X. S., Kita, H. & Okamoto, K. Synthesis of silicalite tubular membranes by in situ crystallization. *Aiche Journal* **49**, 237-247, doi:10.1002/aic.690490122 (2003).
116 Bai, P., Tsapatsis, M. & Siepmann, J. I. Multicomponent Adsorption of Alcohols onto Silicalite-1 from Aqueous Solution: Isotherms, Structural Analysis, and Assessment of Ideal Adsorbed Solution Theory. *Langmuir* **28**, 15566-15576, doi:10.1021/la303247c (2012).
117 Krishna, R. & van Baten, J. M. Hydrogen Bonding Effects in Adsorption of Water-Alcohol Mixtures in Zeolites and the Consequences for the Characteristics of the Maxwell-Stefan Diffusivities. *Langmuir* **26**, 10854-10867, doi:10.1021/la100737c (2010).
118 Xu, D. D. *et al.* On the Synthesis and Adsorption Properties of Single-Unit-Cell Hierarchical Zeolites Made by Rotational Intergrowths. *Advanced Functional Materials* **24**, 201-208, doi:10.1002/adfm.201301975 (2014).
119 Swindlehurst, G. R. *et al.* Nucleation, Growth, and Robust Synthesis of SPP Zeolite: Effect of Ethanol, Sodium, and Potassium. *Topics in Catalysis* **58**, 545-558, doi:10.1007/s11244-015-0396-7 (2015).
120 Mallon, E. E., Jeon, M. Y., Navarro, M., Bhan, A. & Tsapatsis, M. Probing the Relationship between Silicalite-1 Defects and Polyol Adsorption Properties. *Langmuir* **29**, 6546-6555, doi:10.1021/la4001494 (2013).
121 Bai, P., Olson, D. H., Tsapatsis, M. & Siepmann, J. I. Understanding the Unusual Adsorption Behavior in Hierarchical Zeolite Nanosheets. *Chemphyschem* **15**, 2225-2229, doi:10.1002/cphc.201402189 (2014).
122 Cussler, E. L. MEMBRANES CONTAINING SELECTIVE FLAKES. *Journal of Membrane Science* **52**, 275-288, doi:10.1016/s0376-7388(00)85132-7 (1990).
123 Sivakumar, G. *et al.* Bioethanol and biodiesel: Alternative liquid fuels for future generations. *Engineering in Life Sciences* **10**, 8-18, doi:10.1002/elsc.200900061 (2010).
124 Farrell, A. E. Ethanol can contribute to energy and environmental goals (vol 311, pg 506, 2006). *Science* **312**, 1748-1748 (2006).

125 Ragauskas, A. J. *et al.* The path forward for biofuels and biomaterials. *Science* **311**, 484-489, doi:10.1126/science.1114736 (2006).
126 Orts, W. J., Holtman, K. M. & Seiber, J. N. Agricultural chemistry and bioenergy. *Journal of Agricultural and Food Chemistry* **56**, 3892-3899, doi:10.1021/jf8006695 (2008).
127 U.S. Energy Information Administration. http://www.eia.gov/petroleum/ethanolcapacity/.
128 Obrien, D. J. & Craig, J. C. Ethanol production in a continuous fermentation membrane pervaporation system. *Applied Microbiology and Biotechnology* **44**, 699-704 (1996).
129 Groot, W. J., Kraayenbrink, M. R., Waldram, R. H., Vanderlans, R. & Luyben, K. ETHANOL-PRODUCTION IN AN INTEGRATED PROCESS OF FERMENTATION AND ETHANOL RECOVERY BY PERVAPORATION. *Bioprocess Engineering* **8**, 99-111, doi:10.1007/bf01254225 (1992).
130 Uragami, T. Structural design of polymer membranes for concentration of bio-ethanol. *Polymer Journal* **40**, 485-494, doi:10.1295/polymj.PJ2008015 (2008).
131 Bowen, T. C., Li, S. G., Noble, R. D. & Falconer, J. L. Driving force for pervaporation through zeolite membranes. *Journal of Membrane Science* **225**, 165-176, doi:10.1016/j.memsci.003.07.016 (2003).
132 Zhang, W., Yu, X. J. & Yuan, Q. A. ETHANOL FERMENTATION COUPLED WITH COMPLETE CELL RECYCLE PERVAPORATION SYSTEM - DEPENDENCE OF GLUCOSE-CONCENTRATION. *Biotechnology Techniques* **9**, 299-304 (1995).
133 Miyata, T., Nakanishi, Y. & Uragami, T. Ethanol permselectivity of poly(dimethylsiloxane) membranes controlled by simple surface modifications using polymer additives. *Macromolecules* **30**, 5563-5565 (1997).
134 Feng, X. S. & Huang, R. Y. M. Liquid separation by membrane pervaporation: A review. *Industrial & Engineering Chemistry Research* **36**, 1048-1066, doi:10.1021/ie960189g (1997).
135 Bowen, T. C., Li, S. G., Noble, R. D. & Falconer, J. L. Driving force for pervaporation through zeolite membranes. *Abstr. Pap. Am. Chem. Soc.* **225**, 231-FUEL (2003).
136 Vanbekkum, H., Geus, E. R. & Kouwenhoven, H. W. in *Advanced Zeolite Science and Applications* Vol. 85 *Studies in Surface Science and Catalysis* 509-542 (Elsevier Science Publ B V, 1994).
137 Shen, D. *et al.* Synthesis of silicalite-1 membrane with two silicon source by secondary growth method and its pervaporation performance. *Separation and Purification Technology* **76**, 308-315, doi:10.1016/j.seppur.2010.10.021 (2011).
138 Lin, X., Kita, H. & Okamoto, K. Silicalite membrane preparation, characterization, and separation performance. *Industrial & Engineering Chemistry Research* **40**, 4069-4078, doi:10.1021/ie0101947 (2001).
139 Nomura, M., Yamaguchi, T. & Nakao, S. Ethanol/water transport through silicalite membranes. *Journal of Membrane Science* **144**, 161-171, doi:10.1016/s0376-7388(98)00043-x (1998).

140 Nomura, M., Yamaguchi, T. & Nakao, S. Transport phenomena through intercrystalline and intracrystalline pathways of silicalite zeolite membranes. *Journal of Membrane Science* **187**, 203-212, doi:10.1016/s0376-7388(01)00350-7 (2001).
141 Sano, T., Yanagishita, H., Kiyozumi, Y., Mizukami, F. & Haraya, K. SEPARATION OF ETHANOL-WATER MIXTURE BY SILICALITE MEMBRANE ON PERVAPORATION. *Journal of Membrane Science* **95**, 221-228, doi:10.1016/0376-7388(94)00120-0 (1994).
142 Ikegami, T. *et al.* Production of highly concentrated ethanol in a coupled fermentation/pervaporation process using silicalite membranes. *Biotechnology Techniques* **11**, 921-924, doi:10.1023/a:1018474603027 (1997).
143 Matsuda, H. *et al.* Improvement of ethanol selectivity of silicalite membrane in pervaporation by silicone rubber coating. *Journal of Membrane Science* **210**, 433-437, doi:10.1016/s0376-7388(02)00364-2 (2002).
144 Tuan, V. A., Li, S. G., Falconer, J. L. & Noble, R. D. Separating organics from water by pervaporation with isomorphously-substituted MFI zeolite membranes. *Journal of Membrane Science* **196**, 111-123, doi:10.1016/s0376-7388(01)00590-7 (2002).
145 Kuhn, J., Sutanto, S., Gascon, J., Gross, J. & Kapteijn, F. Performance and stability of multi-channel MFI zeolite membranes detemplated by calcination and ozonication in ethanol/water pervaporation. *Journal of Membrane Science* **339**, 261-274, doi:10.1016/j.memsci.2009.05.006 (2009).
146 Sebastian, V. *et al.* Microwave-assisted hydrothermal rapid synthesis of capillary MFI-type zeolite-ceramic membranes for pervaporation application. *Journal of Membrane Science* **355**, 28-35, doi:10.1016/j.memsci.2010.02.073 (2010).
147 Soydas, B., Dede, O., Culfaz, A. & Kalipcilar, H. Separation of gas and organic/water mixtures by MFI type zeolite membranes synthesized in a flow system. *Microporous and Mesoporous Materials* **127**, 96-103, doi:10.1016/j.micromeso.2009.07.004 (2010).
148 Hasegawa, Y. *et al.* Real-time monitoring of permeation properties through polycrystalline MFI-type zeolite membranes during pervaporation using mass-spectrometry. *Separation and Purification Technology* **58**, 386-392, doi:10.1016/j.seppur.2007.05.014 (2008).
149 Weyd, M. *et al.* Transport of binary water-ethanol mixtures through a multilayer hydrophobic zeolite membrane. *Journal of Membrane Science* **307**, 239-248, doi:10.1016/j.memsci.2007.09.032 (2008).
150 Zhang, X. L., Zhu, M. H., Zhou, R. F., Chen, X. S. & Kita, H. Synthesis of silicalite-1 membranes with high ethanol permeation in ultradilute solution containing fluoride. *Separation and Purification Technology* **81**, 480-484, doi:10.1016/j.seppur.2011.08.009 (2011).
151 Zou, X. Q. *et al.* Ethanol Recovery from Water Using Silicalite-1 Membrane: An Operando Infrared Spectroscopic Study. *Chempluschem* **77**, 437-444, doi:10.1002/cplu.201200048 (2012).

152 Shu, X. J., Wang, X. R., Kong, Q. Q., Gu, X. H. & Xu, N. P. High-Flux MFI Zeolite Membrane Supported on YSZ Hollow Fiber for Separation of Ethanol/Water. *Industrial & Engineering Chemistry Research* **51**, 12073-12080, doi:10.1021/ie301087u (2012).
153 Shan, L. J., Shao, J., Wang, Z. B. & Yan, Y. S. Preparation of zeolite MFI membranes on alumina hollow fibers with high flux for pervaporation. *Journal of Membrane Science* **378**, 319-329, doi:10.1016/j.memsci.2011.05.011 (2011).
154 Peng, Y. *et al.* Preparation of zeolite MFI membranes on defective macroporous alumina supports by a novel wetting-rubbing seeding method: Role of wetting agent. *Journal of Membrane Science* **444**, 60-69, doi:10.1016/j.memsci.2013.05.013 (2013).
155 Peng, Y., Lu, H. B., Wang, Z. B. & Yan, Y. S. Microstructural optimization of MFI-type zeolite membranes for ethanol-water separation. *Journal of Materials Chemistry A* **2**, 16093-16100, doi:10.1039/c4ta02837f (2014).
156 Zhang, X. L., Zhu, M. H., Zhou, R. F., Chen, X. S. & Kita, H. Synthesis of a Silicalite Zeolite Membrane in Ultradilute Solution and Its Highly Selective Separation of Organic/Water Mixtures. *Industrial & Engineering Chemistry Research* **51**, 11499-11508, doi:10.1021/ie300951e (2012).
157 Gonzalez-Velasco, J. R., Lopez-Dehesa, C. & Gonzalez-Marcos, J. A. Pervaporation performance of PTMSP membranes at high temperatures. *Journal of Applied Polymer Science* **90**, 2255-2259, doi:10.1002/app.12895 (2003).
158 Mulder, M. H. V., Hendrikman, J. O., Hegeman, H. & Smolders, C. A. ETHANOL WATER SEPARATION BY PERVAPORATION. *Journal of Membrane Science* **16**, 269-284, doi:10.1016/s0376-7388(00)81315-0 (1983).
159 Evcin, A. & Tutkun, O. PERVAPORATION SEPARATION OF ETHANOL-WATER MIXTURES BY ZEOLITE-FILLED POLYMERIC MEMBRANES. *Ceramics-Silikaty* **53**, 250-253 (2009).
160 Zhu, C. L., Liu, M. & Xu, W. SEPARATION OF ETHANOL WATER MIXTURES BY PERVAPORATION MEMBRANE SEPARATION PROCESS. *Desalination* **62**, 299-313 (1987).
161 Cussler, E. L. Diffusion Mass Transfer in Fluid Systems, 3rd edition (2009).
162 Fornes, T. D., Yoon, P. J., Keskkula, H. & Paul, D. R. Nylon 6 nanocomposites: the effect of matrix molecular weight. *Polymer* **42**, 9929-9940, doi:10.1016/s0032-3861(01)00552-3 (2001).
163 Ikegami, T. *et al.* Concentration of fermented ethanol by pervaporation using silicalite membranes coated with silicone rubber. *Desalination* **149**, 49-54, doi:10.1016/s0011-9164(02)00690-2 (2002).
164 Nomura, M., Bin, T. & Nakao, S. Selective ethanol extraction from fermentation broth using a silicalite membrane. *Separation and Purification Technology* **27**, 59-66, doi:10.1016/s1383-5866(01)00195-2 (2002).
165 Geus, E. R., Denexter, M. J. & Vanbekkum, H. SYNTHESIS AND CHARACTERIZATION OF ZEOLITE (MFI) MEMBRANES ON POROUS CERAMIC SUPPORTS. *Journal of the Chemical Society-Faraday Transactions* **88**, 3101-3109, doi:10.1039/ft9928803101 (1992).

Appendix: Top-down approach for MFI nanosheets and their applications as ethanol selective membranes

*The work was done at the beginning of the Ph.D. degree program before bottom-up synthesis of MFI nanosheets were developed yet. In addition, this work was based on initial establishment of top-down strategy of MFI nanosheet preparation consisting of exfoliation and a simple centrifugation. DGC (Density Gradient Centrifugation) is s not introduced in this chapter.

A.1 Introduction

Significant research efforts have focused on renewable energy due to energy security and the environmental impacts of oil.[114,123,124] Bioethanol is the most common biofuel in the world, which may be obtained through the fermentation of starch-based grains, sucrose, and cellulosic materials.[123,125] Since 2005, the United States has become the biggest producer of bioethanol in the world.[126] In 2015, 15 billion gallons of ethanol were made by 195 ethanol plants in the United States.[127]

The fermentation process results in dilute aqueous solutions consisting of 5 to 15 wt% ethanol[99,114,128-130] and combination of ethanol pervaporation can lead to higher yield of ethanol production.[131] The most common strategy for ethanol purification is distillation, however, it is far more energy-intensive than pervaporation.[132] Additionally, pervaporation can separate close-boiling components of liquid mixtures which prove difficult for distillation processes.[1, 6-9,133] Currently, pervaporation technology is applied

to the dehydration of organic solvents, the removal of volatile organic compounds from water, and the separation of organic-organic mixtures.[134]

Pervaporation processes have been studied utilizing various types of membranes for preferential component separation such as zeolitic,[8,9,36,48,78,84,115,135-156] polymeric,[36,102,130,157-160] and zeolite/polymer mixed matrix membranes.[99-109] Among them, the zeolite membranes exhibit uniform pore size, high selectivity, and high chemical and thermal stability.[36,135,136]

The pervaporation process is illustrated by the sorption-diffusion model as represented in **Figure A-1**.[134] Selective sorption of feed components occurs at the membrane surface, followed by diffusion of the sorbed component through the membrane and desorption into a vapor phase.[11, 26-29] The affinity between the membrane surface and the chemical species in the feed solution affects selective sorption: a higher affinity indicates preferential sorption. Molecular vaporization occurs by means of a pressure drop created by establishing a vacuum on the permeate side.

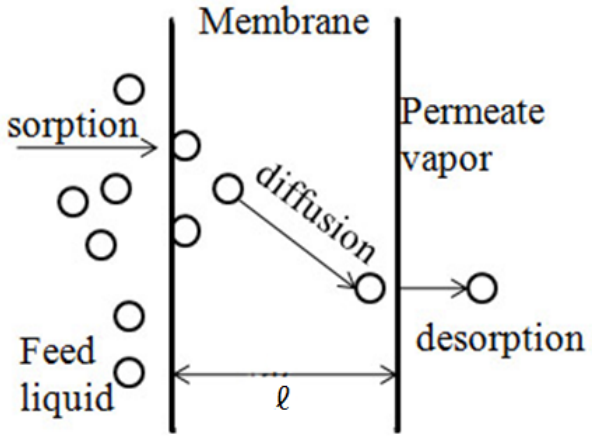

Figure A-2. Schematic description of the sorption-diffusion model. ℓ is membrane thickness.

Hydrophobic zeolites may be exploited for ethanol dehydration since ethanol adsorption would be preferential. Additionally, the straight pore channel of the MFI zeolite framework is larger than the ethanol molecules (4.3 Å), allowing for molecular transport. Consequently, MFI is a suitable candidate for ethanol dehydration. So far, to the best knowledge, ethanol pervaporation through MFI membranes fabricated MFI nanosheet crystals has not reported in the literature. In this appendix, efforts to fabricate MFI membranes from MFI nanosheets which are prepared from exfoliation and purification. This appendix illustrates ethanol pervaporation process to separate ethanol by using the MFI nanosheet membranes.

A.2 Experimental

Synthesis of SDA (C_{22}-$_6$-$_6Br_2$) of multilamellar MFI

138 mL of N,N,N',N'-tetramethyl-1,6-diaminohexane (Sigma-Aldrich, 99 %) was dissolved in mixture of 300 mL of toluene (Sigma Aldrich, anhydrous) and 300 mL of acetonitrile (Sigma-Aldrich, anhydrous) in an 1 L three neck round bottom flask. 25 g of 1-bromodocosane (TCI America, 98 %) was added into the flask and heated to 70 °C under an argon environment for 10 h with connection of a condenser. After cooling to room temperature, the product was precipitated by rotary evaporation at 70 °C. The recovered product was washed with diethyl ether (Sigma-Aldrich, 99 %) followed by rotary evaporation to eliminate the residue of the diethyl ether. The solid product was weighed and corresponding amount of 1-bromohexane (Sigma-Aldrich, 98 %) was added into an 1 L three neck round bottom flask. The designated molar ratio of the solid product

and the 1-bromohexane was 1:2. 300 mL of the acetonitrile was added into the flask as a solvent of the synthesis. The flask was heated at 83 °C with connection of the condenser under an argon environment for 10 h. After cooling to room temperature, the final product was washed with the diethyl ether followed by rotary evaporation to dry the product.

Synthesis of the multilamellar MFI

The bromide ions of the synthesized SDA were exchanged to hydroxyl ions by ion-exchange resin (Amberlite IRN-78, Acros). The SDA was dissolved in DI water and then excessive amount of the ion-exchange resin was added. The whole mixture was stirred overnight. The solution was recovered by vacuum filtration and underwent ion-exchange step again. The concentration of the ion-exchanged SDA solution was determined by titration with 0.1 M hydrochloric acid (Sigma-Aldrich) in the presence of an indicator, phenolphthalein (Sigma-Aldrich). The color of the SDA solution was purple at the initial state of the titration and it became clear at the equivalence point. If the evaluated concentration of the SDA solution was lower than 0.207 M, the water was evaporated by rotary evaporation and then titrated until the concentration of the SDA solution was equal or higher than 0.207 M. Corresponding amount of DI water, tetraethyl orthosilicate (TEOS, Sigma-Aldrich, 98 %) were added and stirred overnight at room temperature in order to hydrolyzed a silica source, TEOS, leading to gel composition of 100 SiO_2: 15 $C_{22\text{-}6\text{-}6}(OH)_2$: 4000 H_2O: 400 EtOH. The resulting gel was transferred into a Teflon-lined stainless-steel autoclave and then heated at 150 °C for 5 days under rotation. The synthesized multilamellar MFI was washed with DI water by repeated centrifugation at

13,000 RCF (Relative Centrifugal Force) for 30 min until pH reached lower than 9. The product was dried at 70 °C.

Exfoliation of the multilamellar MFI (top-down strategy)

0.16 g of the as-synthesized multilamellar MFI powder was mixed with 3.84 g of polystyrene (PS, Mw 45,000, Sigma-Aldrich) and then injected into a twin-screw extruder (DACA mini compounder). The mixture was blended sequentially at 120 ℃ for 20 min, 170 ℃ for 25 min, 150 ℃ for 30 min, and 200 ℃ for 20 min under a nitrogen environment in order to prevent decomposition of the polystyrene at a screw speed of 300 rpm. The MFI nanosheet/polystyrene nanocomposites were extruded out at 150 ℃.

Preparation of the MFI nanosheet membranes

0.1 g of the MFI nanosheet/polystyrene nanocomposite was dissolved in 8 g of toluene, a good solvent for polystyrene, followed by application of ultrasonication for 1 h. The solution was centrifuged at 12,000 RCF for 10 min leading to precipitation of un-exfoliated and big MFI particles. 6 mL of the supernatant composed of the exfoliated MFI nanosheets was pipetted out for coating.

3 g of the toluene coating sol was deposited onto a porous α-Al_2O_3 support, which was prepared by pressing, sintering at high temperature, and then polishing, by vacuum-assisted coating method. The films on the α-Al_2O_3 supports were underwent secondary growth with sol in the presence of TPAOH (tetrapropyl ammonium hydroxide, 1.0 M, Sigma-Aldrich) as SDA. 1.52 g of TPAOH was added to 23.09 g of DI water and stirred. 2.08 g of TEOS was added into the TPAOH solution and stirred overnight at the room temperature in order to hydrolyze the TEOS. The TPA sol was pre-heated at 100 °C for 4

h and filtered by a syringe filter (GHP 0.2 μm) and transferred into a Teflon-lined stainless-steel autoclave.[53,91] The resulting sol composition of the TPA sol was $60SiO_2$: 9TPAOH: $8100H_2O$: 240EOH. The MFI nanosheet coating on α-Al_2O_3 supports were dipped into the sol and hydrothermally treated at 100 °C for 4.5 h, 6 h, 7 h, and 10 h. The membrane was then calcined at 480 °C for 4 h at a ramp/cooling rate of 0.5°C /min to eliminate the TPAOH from the MFI framework.

Pervaporation of ethanol

5 wt % of ethanol/water solution by weight was prepared as a feed solution for pervaporation test of the membranes. The pervaporation set-up was built as seen in **Figure A-2**. The chamber was put on a stirring plate to mix the feed solution during measurement. The chamber was designed with a thermal jacket in order to control the pervaporation temperature. The membrane, sealed by two o-rings within the cell, was immersed in the feed solution. On the permeate side, a vacuum was pulled to maintain a pressure below the vapor pressure. The vapor permeate was condensed and collected in a cold trap.

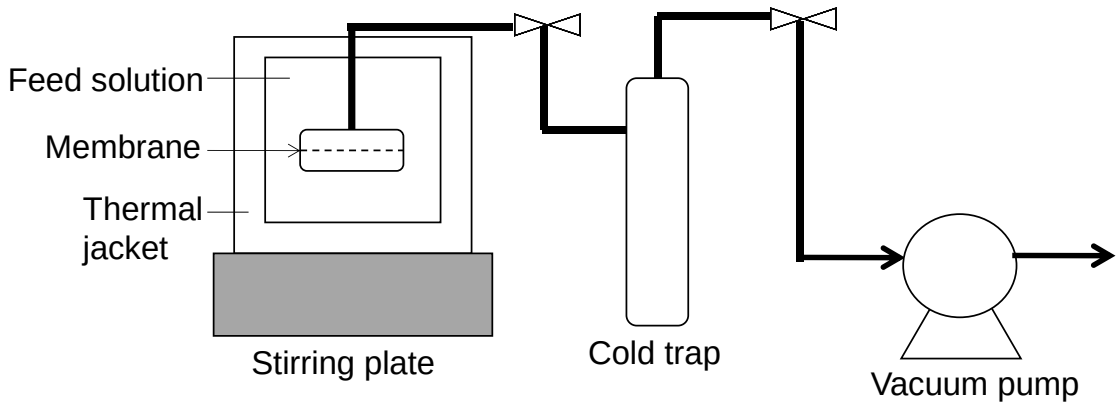

Figure A-2. A schematic diagram of the pervaporation module.

The experimental total mass flux is calculated as:

$$J = \frac{m}{A \cdot t} \quad (1)$$

where *m* is the permeate weight, *A* is the available membrane surface area, and *t* is the measurement time. The flux *J* denotes total flux, which is composed of ethanol and water.

Membrane separation factor, $\alpha_{i/j}$, is defined as:[99,161]

$$\alpha_{i/j} = \frac{J_i/J_j}{[C_i/C_j]_{feed}} = \frac{[C_i/C_j]_{permeate}}{[C_i/C_j]_{feed}} = \frac{[w_i/w_j]_{permeate}}{[w_i/w_j]_{feed}} = \frac{[w_i/(1-w_i)]_{permeate}}{[w_i/(1-w_i)]_{feed}} \quad (2)$$

where C_i and C_j are feed solution concentrations of component *i* and *j*, and w_i and w_j are weight fractions of component *i* and *j*, respectively. The compositions of the feed and permeate were determined by a gas chromatography (GC 6890, Agilent).

A.3 Results and discussion

Preparation of multilamellar MFI nanosheets

The layered assembly of the approximately 3 nm thick MFI nanosheet appeared in TEM image as shown in **Figure A-3A**. As presented in **Figure A-3B**, the intergrown multilamellar MFI nanosheet crystals were produced from interactions between hydrophobic tails of the SDA. Although the intergrown crystals play a role in preventing the collapse of crystal structure, it hinders thin and oriented membrane applications. Therefore, post treatment, exfoliation, is required to prepare single MFI nanosheets. XRD measurement confirmed the crystallinity of multilamellar MFI (**Figure A-3C**).

Exfoliation of multilamellar MFI nanosheets

To delaminate the as-synthesized multilamellar MFI nanosheets, melt extrusion was performed with polystyrene (PS) with a molecular weight of 45,000.[53,63] Before beginning the process, 4 wt % as-synthesized multilamellar MFI was mixed with 96 wt% PS. At high temperatures, above the glass transition temperature or melt temperature of PS, the PS chains have enough mobility to diffuse into the inter-layer space of the multilamellar MFI sheets.[162] During the process, due to the high melt viscosity of PS, it transfers high energy and shear stress to exfoliate the multilamellar MFI. A TEM image of the exfoliated MFI nanosheets/PS nanocomposite, as exhibited in **Figure A-4A**, illustrates dispersion of exfoliated MFI nanosheets in the PS matrix. To employ the exfoliated MFI nanosheets, purification is required due to co-existence of un-exfoliated particles embedded in the PS matrix, as seen in **Figure A-4B**.

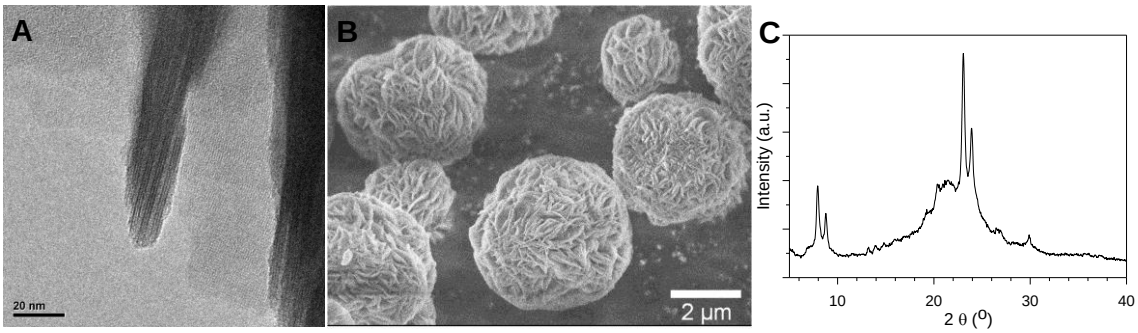

Figure A-3. A TEM image of as-synthesized multilamellar MFI (A), a SEM image of as-synthesized multilamellar MFI (B), and a XRD pattern of as-synthesized multilamellar MFI (C).

Purification of exfoliated MFI nanosheets

To make a deposition of exfoliated MFI nanosheets onto porous α-Al_2O_3 supports, the exfoliated MFI nanosheet/PS nanocomposite was dissolve in toluene, which is a good

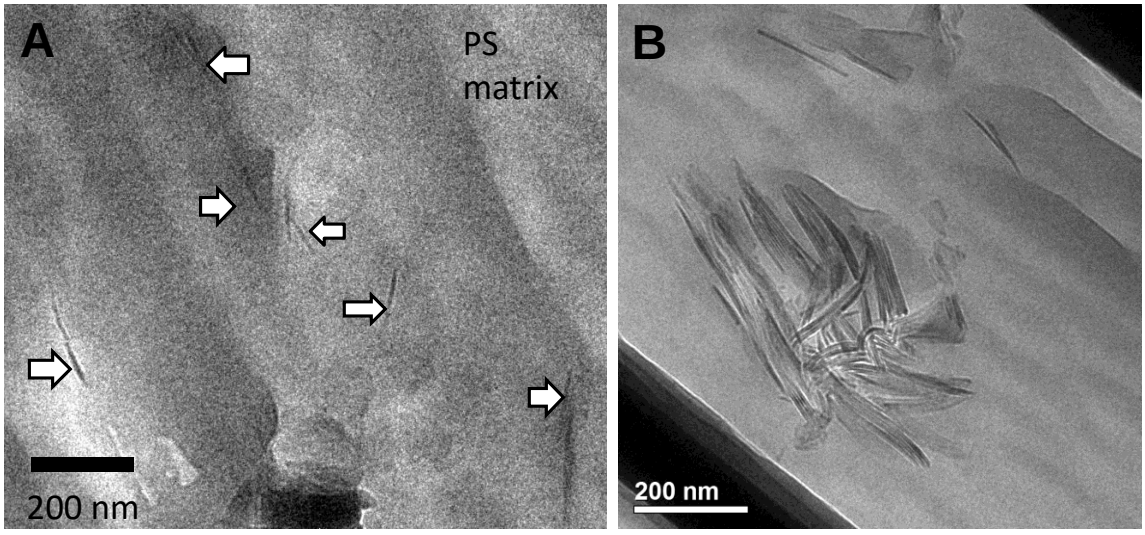

Figure A-4. TEM images of microtomed exfoliated MFI nanosheet/polystyrene (PS) nanocomposite. Dispersion of exfoliated single MFI nanosheets in PS matrix (A), un-exfoliated particle embedded in PS matrix (B). Arrows indicate exfoliated MFI nanosheets.

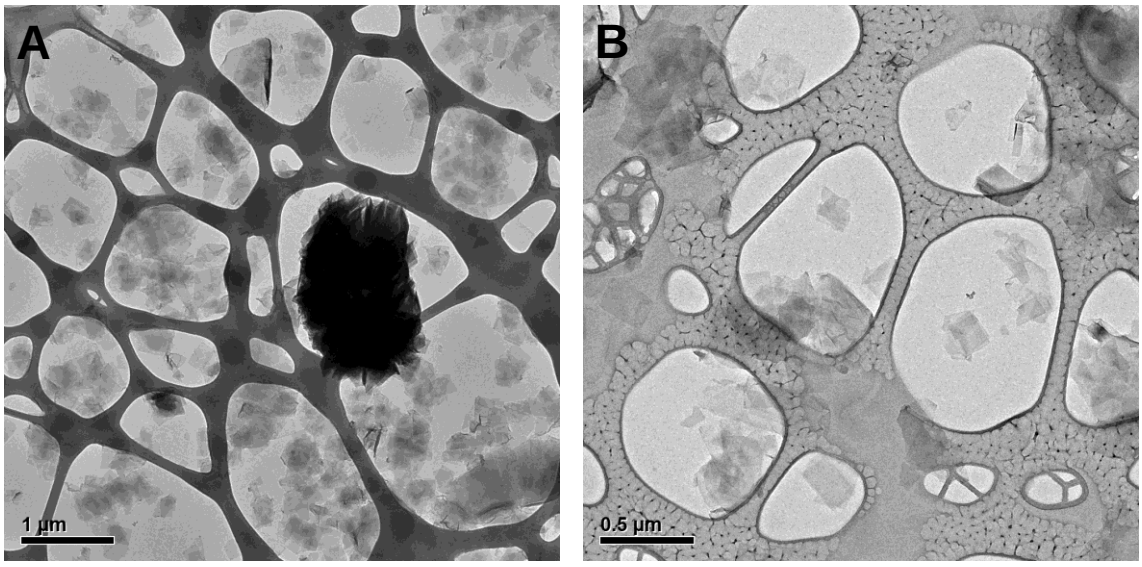

Figure A-5. TEM images of nanosheet suspension after dissolving the exfoliated nanosheet/PS nanocomposite in toluene without purification (A) and with purification (B).

solvent for the PS. A TEM image of the nanosheet suspension in toluene without purification, as presented in **Figure A-5A**, describes the co-existence of the exfoliated

nanosheets and un-exfoliated particles. A centrifugation was applied in order to eliminate the un-exfoliated particles which inhibit uniform and thin deposition of the exfoliated nanosheets on the porous α-Al_2O_3 supports. As a result, as shown in **Figure A-5B**, the nanosheet suspension for coating was composed of exfoliated nanosheets.

Preparation of membranes

For membrane preparation, α-Al_2O_3 discs, consisting of 100 ~ 200 nm pores (**Figure A-6A**), were chosen as a porous support. Due to surface roughness, a polishing process preceded membrane fabrication. The coating suspension was deposited onto the smoothened α-Al_2O_3 supports by vacuum-assisted coating method. The exfoliated nanosheet coating was calcined to eliminate the PS and SDAs out of the MFI framework. A top view SEM image of the exfoliated nanosheet coating (**Figure A-6B**) indicates uniform coverage. However, secondary growth is supposed to be carried out in order to close the nonselective inter-particle gaps, *i.e.*, defects, which are detrimental to permselectivity of the coating. It is evident in from **Figure A-6B**.

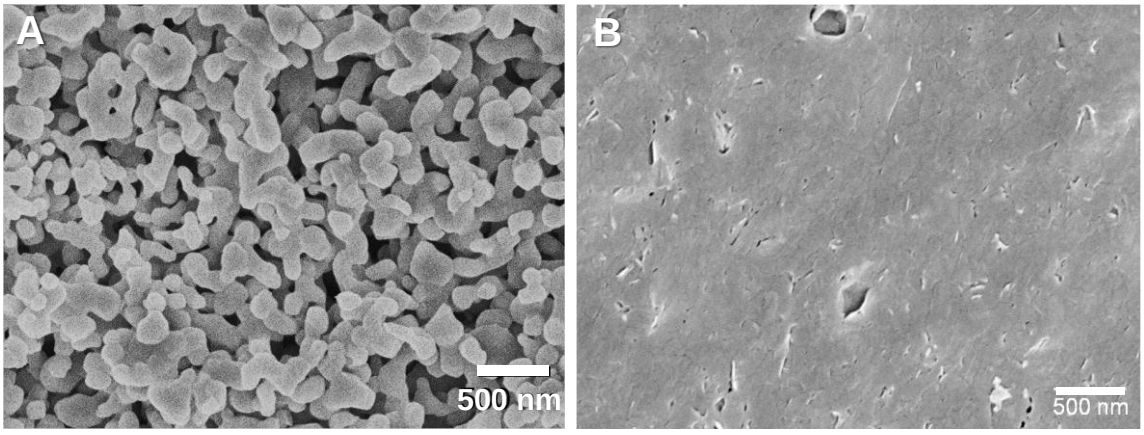

Figure A-6. SEM images of a porous α-Al_2O_3 support after polishing (A) and an exfoliated nanosheet coating on the porous α-Al_2O_3 support (B).

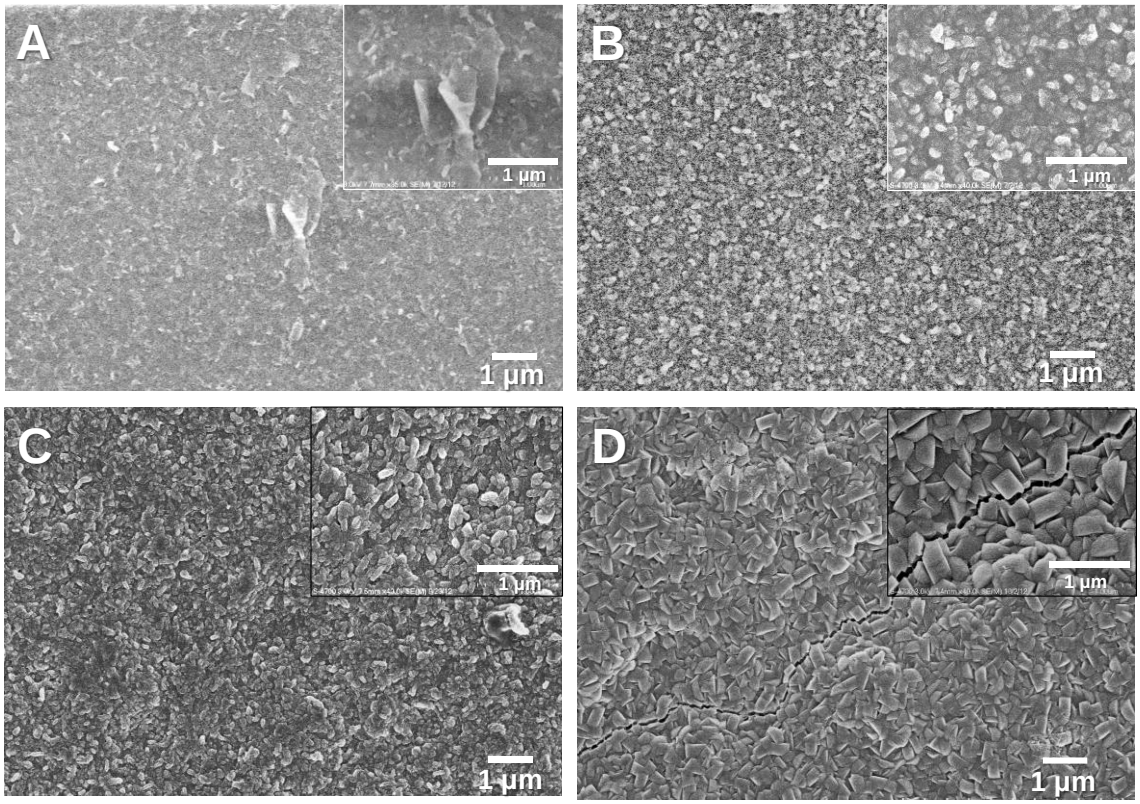

Figure A-7. SEM images of exfoliated nanosheet films followed by hydrothermal treatment with sol in the presence of TPAOH at 100 °C for 4.5 h (A), 6 h (B), 7 h (C) and 10 h (D).

The film after secondary growth at 100 °C for 4.5 h, as shown in **Figure A-7A**, appeared to be hardly intergrown. The nanosheets did not merged with each other and thus the film was not permselective. To enhance quality of the nanosheet films, prolonged secondary growth was conducted. A top view SEM, as seen in **Figure A-7B**, indicates the intergrowth between nanosheets is improved with increased secondary growth time, *i.e.* for 5 h. However, the film did not show permselectivity. This may be associated with insufficient intergrowth of nanosheets underlying the top surface of the film. For longer hydrothermal time, *i.e.* 7 h, well-intergrown film was acquired with random orientation as presented in **Figure A-7C**. The separation factor of the film was increased to 8, which is

moderated but higher compared to other films with no permselectivity. The ethanol permselectivity of the membrane was tested from room temperature to 60 °C as exhibited in **Figure A-8**. As temperature increased, the total flux increased attributed to enhanced mass transfer rate but the separation factors were decreased.

Prolonged secondary growth, *i.e*, 10 h, was conducted in order to consider possibility to improve intergrowth of the membrane which lead to higher ethanol permselectivity. However, a top view SEM, **Figure A-7D**, describes a randomly oriented surface with bigger grains and crack formation. Overgrowth with prolonged secondary growth may lead to crack formation, which is attributed to pronounced mismatch of the thermal expansion coefficient between the α-Al_2O_3 support and the membrane with membrane thickness[90].

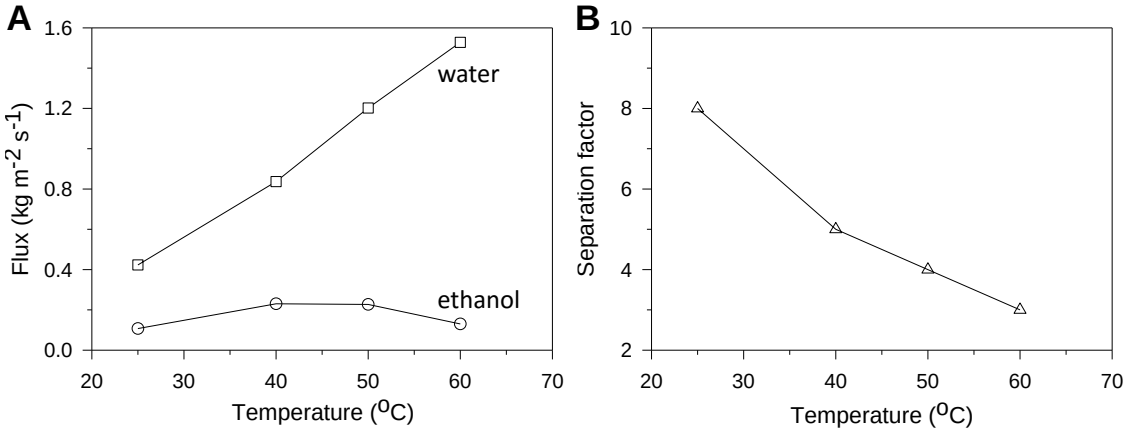

Figure A-8. Ethanol pervaporation performance from room temperature to 60 °C of the membrane fabricated from the exfoliated MFI nanosheets with secondary growth for 7 h at 100 °C. Fluxes of ethanol and water, respectively (A) and separation factor (B).

A.4 Conclusion

MFI nanosheets are successfully prepared by top-down strategy, *i.e.* exfoliation of layered precursor MFI crystals in the presence of PS. The viscosity of PS is manipulated by controlling the blending temperature leading to from low to high shear forces. The parent MFI crystals with layered assembly yield to exfoliated MFI nanosheets by the shear forces generated during the exfoliation process. As a result, the exfoliated MFI nanosheets are obtained in the exfoliated nanosheets/PS nanocomposite form.

In the nanocomposite, un-exfoliated particles co-existed since the degree of the exfoliation is not 100 %. A centrifugation is sufficient to purify the exfoliated MFI nanosheets after dissolution of the nanocomposite into toluene. The purified exfoliated MFI nanosheets were deposited on porous α-Al_2O_3 support discs by vacuum-assisted filtration method. The nanosheet films are not permselective due to the inter-particle gaps which are detrimental to permselectivity. As a result, the film was hydrothermally treated by secondary growth in the presence of precursor sol of TPAOH, the typical SDA of MFI zeolites. In the case of short hydrothermal treatment, intergrowth of the film is not well developed. In contrast, in the case of prolonged secondary growth, the film is overgrown with randomly oriented MFI crystals leading to crack formation.

The best membrane was obtained after 7 h secondary growth. The ethanol pervaporation performance of the membrane was tested at varied temperature range from room temperature to 60 °C. At room temperature, the membrane reveals the highest ethanol separation factor, 8, which is not as high as counterparts reported in the literature.[7,9,78,139-142,158,163,164] However, this is the first membrane prepared from MFI nanosheets for

ethanol separation. The membranes reported in the literature are thicker than 1 μm and fabricated from conventional MFI crystals not from the MFI nanosheets. Compared to the conventional MFI crystals, the external surface of the MFI nanosheets consisting of hydroxyl groups plays a significant role in adsorbing ethanol or water molecules. The hydroxyl groups have a negative effect on preferential adsorption of ethanol molecules over water molecules. Moreover, during calcination, aluminum atom from the porous alumina support may be leached out and incorporated into the zeolite framework leading to uncontrolled hydrophilicity.[165] In contrast to size/shape discrimination, ethanol pervaporation is based on affinity between ethanol and zeolite since ethanol is bulkier than water. If the zeolite is hydrophilic, water molecules are preferentially adsorbed onto the zeolites. The hydrophobicity is key factor to fabricate efficient membranes for ethanol separation. Therefore, MFI nanosheet membranes are not a promising for ethanol pervaporation.